



THE HONG KONG
POLYTECHNIC UNIVERSITY

香港理工大學

Pao Yue-kong Library

包玉剛圖書館

Copyright Undertaking

This thesis is protected by copyright, with all rights reserved.

By reading and using the thesis, the reader understands and agrees to the following terms:

1. The reader will abide by the rules and legal ordinances governing copyright regarding the use of the thesis.
2. The reader will use the thesis for the purpose of research or private study only and not for distribution or further reproduction or any other purpose.
3. The reader agrees to indemnify and hold the University harmless from and against any loss, damage, cost, liability or expenses arising from copyright infringement or unauthorized usage.

IMPORTANT

If you have reasons to believe that any materials in this thesis are deemed not suitable to be distributed in this form, or a copyright owner having difficulty with the material being included in our database, please contact lbsys@polyu.edu.hk providing details. The Library will look into your claim and consider taking remedial action upon receipt of the written requests.



THE HONG KONG
POLYTECHNIC UNIVERSITY

Department of Mechanical Engineering

**Numerical Models for Sound Propagation in
Long Spaces**

Lai Yuen Cheung Chenly

A thesis submitted in partial fulfillment of the requirements
for the degree of Doctor of Philosophy

May 2011

CERTIFICATE OF ORIGINALITY

I hereby declare that this thesis is my own work and that to the best of my knowledge and belief, it reproduces no material previously published or written nor material which has been accepted for the award of any other degree or diploma, except where due acknowledgement has been made in the text,

(Signed)

Lai, Yuen Cheung Chenly

(Name of student)

Abstract

Both reverberation time and steady-state sound field are the key elements for assessing the acoustic condition in an enclosed space. They affect the noise propagation, speech intelligibility, clarity index, and definition. Since the sound field in a long space is non diffuse, classical room acoustics theory does not apply in this situation. The ray tracing technique and the image source methods are two common models to fathom both reverberation time and steady-state sound field in long enclosures nowadays. Although both models can give an accurate estimate of reverberation times and steady-state sound field directly or indirectly, they often involve time-consuming calculations. In order to simplify the acoustic consideration, a theoretical formulation has been developed for predicting both steady-state sound fields and reverberation times in street canyons. The prediction model is further developed to predict the steady-state sound field in a long enclosure. Apart from the straight long enclosure, there are other variations such as a cross junction, a long enclosure with a T-intersection, an U-turn long enclosure.

In the present study, an theoretical and experimental investigations were conducted to develop formulae for predicting reverberation times and steady-state sound fields in a junction of a street canyon and in a long enclosure with T-intersection. The theoretical models are validated by comparing the numerical

predictions with published experimental results. The theoretical results are also compared with precise indoor measurements and large-scale outdoor experimental results.

In all of previous acoustical studies related to long enclosure, most of the studies are focused on the monopole sound source. Besides non-directional noise source, many noise sources in long enclosure are dipole like, such as train noise and fan noise. In order to study the characteristics of directional noise sources, a review of available dipole source was conducted. A dipole was constructed which was subsequent used for experimental studies. In addition, a theoretical model was developed for predicting dipole sound fields. The theoretical model can be used to study the effect of a dipole source on the speech intelligibility in long enclosures.

Acknowledgements

The author would like to express deepest gratitude to Prof. C. W. Leung, currently professor in the Department of Mechanical Engineering of the Hong Kong Polytechnic University and Prof. K. M. Li, now professor in Ray W. Herrick Laboratories, School of Mechanical Engineering of Purdue University. The author is grateful for their outstanding support and precious advice. No doubt their great intellect and wisdom have had a considerable effect upon the academic progress and the author is much indebted to them.

The author would also like to acknowledge some research colleagues Dr. Siu Tong So, Dr. Wai Sun Fung, Mr. Tsz Leung Ip, Dr. Ming Kan Law, Dr. Wai Keung Lui and Dr. Yat Sze Choy for their genuine support, advice and encouragement which allowed the author to complete this thesis. Many thanks are acknowledged to all professors, staff and colleagues in the Mechanical Department for their kind assistance during the study.

Last but not least, the author would like to dedicate his piece of work to his dearest wife Annabella for her patience, encouragement and unceasing support. He also likes to thank his kids Vito and Mandy for understanding during the study.

Publications arising from the thesis

1. C. Y. C. Lai and K. M. Li, “A simple formula for predicting the reverberation time in long enclosures,” *ICSV* **14**, (2007).
2. Chenly Y. C. Lai and K. M. Li, “Prediction of sound fields in long enclosure due to a dipole source,” *J. Acoust. Soc. Am.* **122**(5), 2963-2964 (2007).
3. C. Y. C. Lai, K. M. Li and C. W. Leung, “Predictions of the reverberation time in a street canyon,” *ICSV* **15**, (2008).
4. K. M. Li and Chenly Y. C. Lai, “Prediction of reverberation times and sound pressure levels town streets,” *J. Acoust. Soc. Am.* **125**(4), 2494 (2009).
5. K. M. Li and Chenly Y. C. Lai, “A note on noise propagation in street canyons,” *J. Acoust. Soc. Am.* **126**(2), 644-655 (2009).

Table of Contents

Abstract	ii
Acknowledgements	iv
Publications arising from this thesis	v
Table of Contents	vi

Chapter 1 - Introduction

1.1 Background of research.....	1
1.2 Literature review.....	5
1.2.1 Speech-transmission intelligibility.....	5
1.2.2 Room acoustics.....	8
1.2.3 Acoustic study for street canyon.....	9
1.2.4 Acoustic study for a long enclosure.....	11
1.2.5 Dipole noise source in long enclosure.....	17
1.3 Objectives of the study and organisation of thesis.....	20

Chapter 2 - Noise propagation in street canyons

2.1 Introduction.....	25
2.2 Theory.....	27
2.2.1 Total steady-state sound energy at a receiver.....	27
2.2.2 Reverberation time in street canyons.....	35
2.3 Comparison with experimental measurements.....	39
2.3.1 Full scale field measurements in a town street.....	39
2.3.2 Indoor model experiments.....	43
2.3.3 Outdoor field measurements in an alley street.....	48
2.4 Summaries.....	52
Tables.....	53
Figures.....	55

Chapter 3 - An analytical model for predicting sound propagation in long enclosures

3.1 Introduction.....	71
3.2 Theory.....	73
3.2.1 Sergeev's model.....	73
3.2.2 Kang's image source method.....	75
3.2.3 Analytical prediction model.....	78
3.3 Experimental validation.....	83

3.3.1	Theoretical comparison.....	83
3.3.2	Indoor model measurements.....	85
3.3.3	Outdoor field measurements.....	88
3.4	Summaries.....	90
	Tables.....	92
	Figures.....	93

Chapter 4 – Transmission of noise through a junction in a street canyon

4.1	Introduction.....	107
4.2	Theory.....	109
4.2.1	Formulation of the problem.....	109
4.2.2	Transmission of noise through a cross junction.....	114
4.2.3	The sound field round a corner of a cross junction.....	120
4.2.4	An incoherent model for noise transmission.....	125
4.3	Experimental validations.....	126
4.4	Prediction of noise attenuation in street canyons with a cross-junction.....	132
4.5	Summaries.....	136
	Tables.....	138
	Figures.....	139

Chapter 5 – Sound propagation in a long enclosure with a T-intersection

5.1	Introduction.....	155
5.2	Theory.....	156
5.2.1	The steady state sound field at a receiver.....	156
5.2.1.1	Sound field of a straight long enclosure.....	156
5.2.1.2	Sound field at the opposite end of the main enclosure.....	161
5.2.1.3	Sound field at the side branch.....	164
5.2.2	Reverberation time in a long enclosure with a “T” intersection.....	167
5.2.2.1	Reverberation time of a straight long enclosure.....	167
5.2.2.2	Reverberation time of the opposite end of the long enclosure.....	170
5.2.2.3	Reverberation time of the side branch.....	171
5.2.3	Sound field and reverberation time by incoherent model.....	173
5.3	Experimental validations.....	175
5.3.1	Model tunnel with T-branch.....	175
5.3.2	Field measurement.....	181
5.4	Summaries.....	184
	Tables.....	186

Figures..... 188

Chapter 6 – Constructing a dipole source

6.1 Introduction..... 201
6.2 Acoustic dipole..... 202
6.3 Existing dipole sources..... 203
6.4 Dipole source constructed by two loudspeakers..... 206
6.5 Summaries..... 211
Figures..... 214

Chapter 7 – Noise propagation in a long enclosure due a dipole source

7.1 Introduction..... 225
7.2 Theory..... 226
7.3 Field measurements..... 229
 7.3.1 Full scale field measurements – a long corridor..... 229
 7.3.2 Indoor measurements – a model tunnel..... 232
7.4 Propagation of non-perfect dipole source in a long enclosure..... 234
 7.4.1 Propagation loss of non symmetrical dipole source..... 235
 7.4.2 Experimental measurements..... 237
7.5 Summaries..... 239
Tables..... 241
Figures..... 242

Chapter 8 – Conclusion and suggestions for future work

8.1 Conclusion..... 255
8.2 Limitations of developed models..... 260
8.3 Suggestions for future work..... 261

References..... 265

Chapter 1

Introduction

1.1 Background of research

The objective of this study is to predict the sound field in a long enclosure. The parameters of interest in this study include steady-state sound fields and reverberation times. An enclosed area can be identified as a long enclosure where one dimension is much larger than the other two. In addition, the other two dimensions are still relatively greater than the acoustic wavelength of interest. In this study, the long enclosure is modelled to have a rectangular cross section and to be of an infinite length, i.e. no end wall reflection. The examples are underground train station and its platform, a road or rail tunnel, a pedestrian subway and a corridor in a building. Apart from the straight long enclosure, there are other variations. By treating the flanking facades as a pair of parallel side walls, the road pavement is taken as the floor, and the opening at the top is represented by a perfectly absorptive ceiling, meaning that a street canyon can be considered as an extreme variation of long enclosure. A T-shape corridor, a long corridor with a perpendicular side branch, is the other typical example.

The associated acoustic problems in a long enclosure are high ambient noise and lack of speech intelligibility.

Normally, acoustic consideration is not placed in the first priority when constructing long enclosures. Cost consideration and associated maintenance problems drive the design engineers to use less sound absorption materials for noise reduction. For fire drills, verbal warnings and general announcements are provided by public address (PA) systems which are normally installed in long enclosures. Increasing the sound power output of the PA system will increase the audibility but not necessarily improve the speech intelligibility directly. There are several factors that affect the speech intelligibility including speech to noise level or so called signal to noise ratio and reverberation times in long enclosures.

Speech transmission index (STI) is one of the widely acceptable ways to indicate the quality of sound perception [1, 2]. Speech transmission index is a single index that was developed for predicting speech intelligibility of various types of transmission channels and is now widely used for room acoustic to classify the quality of sound perception. To calculate this single index, most of the important acoustics parameters such as steady-state sound pressure level, reverberation time and ambient noise level

have been considered. Rapid speech transmission index (RASTI) is a simplified version of the STI that can indicate the speech intelligibility and it has also been demonstrated that both RASTI and STI are highly correlated [3].

In order to predict the speech intelligibility, both the steady-state sound fields and reverberation times should be considered. Based on the assumption of a diffuse sound field, the classical room acoustic theory [4] was developed and used for more than a century to predict the reverberation time in a regular enclosure. By the reverberation time, the steady-state sound field can be calculated accordingly [5]. However, due to widely different dimensions of a long enclosure, this classical theory is unsatisfactory as the assumption of the diffuse field does not hold in this situation. Yamamoto [6] was the first to study propagation of sound fields in corridors in the 1960s. After that, a lot of investigations relating to the steady-state sound fields and reverberation times in long enclosures have been conducted. Most of investigations are using either the image source method or the ray tracing technique. Although most of the models can give an accurate estimate of the steady-state sound field and reverberation times, they often involve time-consuming calculations. Furthermore, studies related to non-straight long enclosures are very limited even though the non-straight long enclosures are commonly found in our daily life.

Besides reverberation times and steady-state sound fields, ambient noise is the other important issue when predicting the speech intelligibility. In previous studies, the ambient noise was assumed to be contributed by either a constant environmental noise which was independent to the source and receiver locations or it was contributed by a non-directional noise source. In the long enclosure, many noise sources are directional and dipole like, such as train noise and fan noise. Although dipole sources are assumed to be less efficient radiators than corresponding monopoles and neglected in the ambient noise prediction in the room acoustic study, there are many situations when the dipole strength is very large and there is no significant contribution from non-directional noise sources in a long enclosure.

In order to simplify the acoustic consideration, a closed form theoretical formulation is developed for predicting both the steady-state sound field and reverberation time in a special variation of long enclosure – the street canyon in the first part of the study. The formulation is generalised for predicting steady-state sound pressure level in a straight long enclosure.

The theory for predicting noise through a junction in a street canyon is proposed afterwards. The theory is further extended to predict sound field in a long enclosure

with a T-intersection.

Besides non-directional noise sources, many noise sources in a long enclosure are dipole like such as train noise and fan noise. In order to study the characteristics of directional noise sources, a review of available dipole sources is conducted in the study. In addition, a theoretical model is developed for predicting dipole sound fields. The theoretical model can be used to study the effect of a dipole source on the speech intelligibility in long enclosures.

1.2 Literature review

1.2.1 Speech-transmission intelligibility

Speech-transmission intelligibility is developed to measure the effectiveness of understanding speech of various types of transmission channels which is standardized for room acoustics so as to classify the quality of sound perception. There are principally two different assessment methods for determining the intelligibility of speech transmission system, namely subjective assessment and objective assessment.

Subjective assessment is an assessment method based on the use of speakers and listeners to perform an intelligibility test with using phonemes, words (these may be

meaningful words or nonsense words) and sentences. Various techniques have been used to prepare the test material with meaningful words, nonsense words which consist of a random combination of a consonant, vowel, and consonant (so called CVC-word) or words embedded into a carrier phrase. The response method might allow the listener to respond to what he/she thinks they have heard or to select from a group of alternatives [7 - 10]. This assessment method has the obvious advantage of its directness. However, there are some serious drawbacks, such as the need for a large number of trained talkers, listeners and poor information on the type of degradation on the channel.

Objective assessment is an assessment method based on the physical parameters of the speech transmission channel to predict the intelligibility rather than measure. The speech signal is assumed as the contributions of individual frequency bands and physical parameters of the transmission channel include intensities of speech and noise on individual frequency bands. The concept was first proposed between 1925 and 1930 by Fletcher [11] and modelled by French and Steinberg in 1947 [12]. By using the proposed method a relevant index (Articulation Index, AI) was obtained. The method was reconsidered by Kryter [13] who greatly increased its accessibility by the introduction of a calculation scheme, work sheets, and tables. The calculation of

the AI basically consists of three parts. First, the effective signal to noise ratio within a number of frequency bands is calculated. Second, the effective signal to noise ratio is transformed to an octave band contribution, ranging from one to zero. Third, the weighted mean of the contributions of all relevant octave bands is calculated then constitute the AI.

A new concept of Modulation Transfer Function (MTF) for assessing the effect of an enclosure on speech intelligibility was introduced by Steeneken and Houtgast [1, 2].

The Modulation Transfer Function is a physical characteristic which reflects the effect of the room (reverberation, interfering noise) on the modulation index of a (hypothetical) test signal with a variable modulation frequency. The MTF can be converted into a single index, the Speech Transmission Index (STI). The Speech Transmission Index bears a direct relation to speech intelligibility and has been applied in several cases [14, 15]. A study shows that the basic assumption of AI and STI, predicting the intelligibility of speech is obtained by simple addition of the contribution of individual frequency band, is not optimal [16]. Actually, contribution of individual frequency bands is based on mutual dependence. Redundancy–correction factors for adjacent frequency bands were introduced to improve prediction accuracy. The IEC standard [17] was revised according to this improvement on 1998.

The rapid speech transmission index (RASTI) is a simplified version of the STI. It is depended on two octave bands, 500 Hz and 2000 Hz, and provides a fast evaluation of speech intelligibility. Based on a series of articulation tests, it has been demonstrated that the STI and RASTI were highly correlated with articulation scores [3].

1.2.2 Room acoustics

Sabine theory [4] is the classical room acoustic theory developed and used for more than a century. Based on other considerations, Eyring developed a slightly different formula which improves the prediction in the high sound absorption conditions [18].

Millington developed the other reverberation formula to avoid the Eyring mistake when the surface material is highly absorbent and absorption coefficient is greater than unity [19]. However, there is a drawback in Millington's formula. When the absorption coefficient of one of the surfaces of the room, even if it is very small, is equal to unity, the absorption exponent would be infinitely large and the reverberation time would be zero. Uniform absorption of all surfaces is the basic assumption of both the Sabine and Eyring theories and uneven distribution of absorption will cause a prediction error in both theories. Fitzry experimentally verified that problem, and then proposed a formula in which the absorption exponent is calculated by an area-weight absorption exponent in three orthogonal directions [20]. Based on Fitzry's idea,

Arau-Puchades proposed an improved reverberation formula which was based on a weighted absorption exponent [21]. More recently, the ray tracing technique and the image source method are two popular approaches that have been used to develop numerical models for predicting reverberation times in rooms [22 - 25]. Despite these efforts, the Sabine formula is still used today, especially in the preliminary design stage because of its simplicity and ease of application. It can give a reasonable estimate of the reverberation time in rooms.

1.2.3 Acoustic study for street canyon

From a scientific point of view, the investigation of outdoor sound propagation can be traced back to the mid-nineteenth century. In the 1930s, the theoretical study of outdoor sound propagation became popular since the concern for noise problem in community became important. During this period, investigations were focusing on geometrical spreading, atmospheric absorption, ground effect, refraction, the effect of atmospheric turbulence and the effect of topography [26]. It is of interest to point out that the first measurements of sound propagation in urban areas were performed to determine an optimal location for sirens during 1940s [27, 28]. Wiener *et al.* [29] conducted a theoretical study on the propagation of sound, the reverberation time, and speech intelligibility in a city street of Boston. In 1970s, Aylor *et al.* [30] conducted a

study to investigate the effect of ivy grown on building façades on the reverberation time. Yeow [31, 32] performed some measurements of the reverberation time in downtown residential areas. From their experimental results, Ko and Tang [33] suggested that the reverberation time of a street canyon was proportional to the volume bounded by the tall buildings in street canyons. Steenackers *et al.* [34] carried out a series of experimental measurements of the sound decay curves in a street canyon. Their study was focused on the determination of the absorption coefficient in favour of the reverberation time of the street canyons but no theoretical models were introduced.

There were also a number of other studies addressing the theoretical and numerical aspects of sound propagation in street canyons in the past few decades. Typically, either an image source model or a diffuse reflection model is used to compute the sound fields and the reverberation times in a street canyon [35, 36]. Most of the image source methods are based on incoherent models [37] although a coherent model has been used in a recent study [38]. Despite these theoretical and experimental studies, there is still no simple yet accurate formula to predict the noise levels and the reverberation time in street canyons.

Besides the straight street canyon, the cross junction is one of variations of street canyon that can be found frequently in daily life. The sound field propagation characteristic on the street canyon with cross junction is totally different to the straight street canyon since part of the sound energy will be transmitted into the side arm of the cross junction while the source and the receiver are separated by the junction. So *et al.* [39 - 41] have used a coherent image source model to predict the sound field in the “T” intersection and the “U” sharp section of a long enclosure. However, they do not provide any systematic formation to do so. Besides the So *et al.* studies, there are only a few studies related to the sound propagation through a junction in a street canyon.

1.2.4 Acoustic study for a long enclosure

Based on the assumption of diffuse sound field, Sabine theory [4] was developed and used for more than a century to predict the reverberation time in a regular enclosure. The dimensions of a long enclosure, where one dimension is much larger than the other two, mean those classical formulae are no longer valid in this situation.

Since 1960s, a number of investigations relating to sound propagation in a long enclosure were conducted. Yamamoto [6] was among the first to study sound

propagation in corridors. In the study, both source and receiver were located at the centre of the corridor cross-section and the effect of numerous reflections from the boundary walls was estimated numerically for a variety of absorption coefficients. The experimental measurements were made with a maximum source-receiver distance of 18m. As a result, Yamamoto's predictions were limited to allow generalisation to a more general condition. Davies [42] presented a similar geometrical acoustics approach to high frequency noise propagation in acoustically treated corridors in the early 1970's. Expressions are given for the attenuation of sound for a variety of cases when one or more walls have high or low absorption coefficients. Kuttruff [43] proposed two theoretical models for a town street. In the first he considered a street as a long room with hard walls and a completely absorbing ceiling. The reverberation time is deduced from Sabine's formula where the length of the room is tending to infinity. In the second he used an image-source model to calculate the intensity and variability of the noise level from traffic flow. Kuttruff indicated the difference between the diffuse reverberation model and the image source method. Whether the diffuse reverberation model or the image source method could be applied on the prediction should depend mainly on the degree of the diffuseness that is introduced by irregularities in the facades.

In the late 1970's, Sergeev [44] developed a series of simple formulae to predict the sound density of an incoherent point source in city streets and in tunnels. The formulae were developed from an image source method. In his study, a point source was considered and total sound field summed the contributions from all reflection rays. He pointed out that the attenuation is non-exponential and the decay is nonlinear on a logarithmic scale. Air absorption and angle-dependent reflection coefficients were considered in the study. However, he offered no measurement result to support his model. Steenackers *et al.* [34] analysed the reverberation in town streets caused by the multiple reflections between flanking houses and buildings. In the study, he noticed that the decay curves were not straight but were curved. Furthermore, the decay curves can be better explained by the image source method and not by the diffuse reverberation model. The amount of reverberation depends mainly on the street width, the absorption and the diffusion of the facades. The absorption coefficients can be evaluated by means of a simple reverberation measurement combined with a correct interpretation of sound decay curves. On the basis of this approach, the influence of the street reverberation on the sound field produced during the passage of a single vehicle was calculated.

In the early 1980's, Redmore [45] developed an acoustic ray theory to predict relative

sound pressure levels along a corridor or in adjacent rooms caused by a sound source in a corridor. He suggested that sound level along a corridor can be divided into three sections generally, e.g. direct field, beyond the direct field and reflection from end termination. Direct field region is classified as the receiver close to the source and the sound pressure level decreases rapidly (inverse square of the distance). Beyond the direct field is a length of approximately linear sound pressure level attenuation region. If the end termination has a large reflection coefficient, most of the sound energy travelling along the corridor is reflected back and decreases the rate of sound pressure level attenuation in the reflection region.

In the 1990's, Kang [46] conducted measurements and showed that classical room acoustics was not applicable in a long enclosure since the assumption of the diffuse field does not necessarily hold for the extreme dimensions. Furthermore, theoretical formulae for calculating the reverberation in rectangular long enclosures with geometrically reflecting boundaries are derived by applying the image source method [47]. The theory was validated by comparing the numerical predictions with the experimental results that are conducted in a corridor. From these formulae, it can be seen that the reverberation time increases sharply to a maximum and then decrease slightly when increasing the source-receiver distance from zero to the receiver

faraway from the sound. Air absorption was considered in Kang's study also and the reverberation time decay curves are more linear after taking the air absorption into account. After that, a semi-empirical method was developed and, accordingly, a computer program has been written [48]. The basic idea of this method is to correct the calculations of existing theoretical formulae or computer simulation models with an empirical database that is based on a physical scale model or site measurements. Particular attention is given to the speech intelligibility of multiple loudspeaker public address systems in underground stations.

In a recent study, Yang and Shield [49] developed a ray-tracing computer model to predict the sound field in long enclosures with particular reference to rectangular and curved cross sections, such as underground train stations. The model provides the detailed predictions of sound pressure level, early decay time, clarity index, and definition. The model also calculates the value of the speech transmission index at individual points. Based on the technique of radiosity, Kang [50] developed a computer model for calculating acoustic indices in rectangular enclosures with diffusely reflecting boundaries. The model divides every boundary into a number of patches and receivers with nodes in a network. The effectiveness and accuracy of the model has been demonstrated in several enclosures. Lu and Li [51] were using simple

ray theory that takes account of multiple reflections to develop a numerical model for the sound field prediction in narrow streets with a width of less than 10 m. Furthermore, based on coherently summing, they developed a simple numerical model to predict sound propagation in long enclosures [52, 53]. The coherent model was extended by Li and Lam [54] to predict the reverberation time and speech transmission index. Based on fixed non-linear regression, statistically deriving prediction functions from measured data and ray-tracing simulation results, Wijngaarden and Verhave developed a statistical based prediction formula to simplify the speech transmission index (STI) prediction for traffic tunnels [55]. Unfortunately, the developed formula can only be applied in a particular traffic tunnel application when the values of all variables fall within the specified ranges.

Although most of models described above can give an accurate estimate of steady-state sound fields and/or reverberation times, there is basically no closed form solution proposed by the investigators.

Apart from the straight long enclosure, there are other variations. A long enclosure with a T-intersection and/or U-turn corridors are commonly found in office buildings, shopping malls, residential houses and schools. Bend corridors and long enclosures

with a cross-junction are frequently found in train stations and underground tunnels.

Studies that focus on the sound field propagation in branching long enclosures

becomes necessary but the related studies are limited to a few nowadays [39 - 41].

1.2.5 Dipole noise source in long enclosure

Speech intelligibility is affected by two factors; signal to noise ratio and reverberation

time. For predicting the speech intelligibility, background noise is assumed as either

created by a non-directional acoustic monopole noise source or a constant ambient

noise level which is independent of the distance between source and receiver [55, 58 -

60]. Besides acoustic monopole and constant ambient noise, there are many noise

sources which are directional such as railway noise and fan noise. Both railway noise

and fan noise are classified as dipole shape and are frequently found in a long

enclosure. Although a railway noise survey shows that the railway noise is mainly

contributed by rolling noise and aerodynamic noise [61] and the aerodynamic noise is

classified as acoustic quadrupole [62], Talotte mentions that rolling noise still

dominates the railway noise when the operating train speed is below 300 km/h [63].

The structure of a dipole field can be easily understood by considering the dipole in

terms of a pair of anti-phase monopoles with equal acoustic power and separated in a

small distance [64]. Because a dipole involves sources of opposite signs there is some cancellation of the acoustic field, so a dipole source is assumed as a less efficient radiator than a corresponding monopole and neglected on the ambient noise prediction [65]. In a long enclosure, there are many situations when the dipole strength is very large and there is no significant contribution of a non-directional source.

From the 1970s, Peters [66] was the first to classify railway noise as an incoherent line of dipoles and that railway noise was dominated by wheel radiation. Although Rathe mentioned that a monopole line source model provides closer prediction than a dipole line source when the prediction model is not adjusted for atmospheric or ground attenuation influences [67], Hohenwarter shows that a dipole line source could provide a more acceptable prediction than monopole afterwards [68]. Nowadays most generic models, such as from Austria [69, 70], Germany [71], Switzerland [72] and the Netherlands [73], classify the sound radiation characteristics of railway noise in both horizontal and vertical planes as dipole shape. The sound radiation characteristics of a railway wheel were further investigated by Thomson and Jones in 2000s [74]. In Thomson and Jones study, the directivity of wheel radiation is obtained by measured data and the wheel radiation sound field can be closely approximated by an omni-directional field in radial motion but dipole distribution in the axial motion.

Apart from train noise, noise problems associated with fan installations are not uncommon in long enclosure. A noise survey showed that the corridor was the noisiest area in hospital and the noise level was maintained between 65 to 70 dBA round the clock [75]. Even worse, the noise level of the nurse station and patient room were affected by the corridor since all doors in the hospital had large gaps at the floor and lacked acoustic isolation. The corridor background noise was almost certainly caused by heating, ventilating and air conditioning in the study.

Baade was the first to classify the noise of an axial fan in an air duct as dipole shape [76]. Margett then demonstrated that either tonal or broadband noise generated by an axial fan is of a dipole nature [77]. Thompson *et al.* have modelled the noise generated by blade tip of centrifugal fan as dipole in their study [78]. Neise reviewed the fan noise generation mechanisms of both axial and centrifugal fans in his study [79]. He pointed out that although monopole and quadrupole radiation can be important in some cases, the dipole radiation still plays the most important role in fan noise generation. Hodgson and Li studied the noise emission of personal computer cooling fans and found that the directivity of the fan noise radiation is dipole like [80].

Both rolling noise and fan noise are classified as dipole shape in previous studies and

the dipole noise sources are easily found anywhere in the long enclosures. However, the study of acoustic dipole sound field propagation is very limited, especially in long enclosures.

1.3 Objectives of the study and organisation of thesis

The objective of this study is to simplify the acoustic consideration for a long enclosure. In order to achieve this objective, this study is divided into eight chapters. Chapter 1 includes the background of the study and the outline of objectives to be achieved. A literature review is given afterwards, which focuses on the studies of speech-transmission intelligibility, room acoustics, acoustic studies for street canyons and for long enclosures, and the dipole noise sources that are found in a long enclosure.

As a result of the rapid growth in mechanised transport and transportation systems, land transportations are becoming the primary source of noise pollution in high-rise city. Despite the previous theoretical and experimental studies, there is still no simple but accurate formula to predict the noise levels and the reverberation times in street canyons. In order to speed up the assessment of effectiveness noise control, theoretical formulations for evaluating both steady-state noise level and reverberation time in a

street canyon are developed in Chapter 2. The theoretical models are validated by comparing the numerical predictions with published experimental results, and indoor and outdoor experimental results.

The theoretical formulation developed in Chapter 2 is generalised for regular long enclosures in Chapter 3. In Chapter 3, a long enclosure is modelled to have a rectangular cross-section and of an infinite length, i.e. no end wall reflection in this study. Comparative validations of the predicted results with experimental data are given before the end of the chapter.

Chapter 2 and Chapter 3 are focused on simplifying the acoustic prediction in a straight long enclosure. Apart from a straight long enclosure, there are other variations that commonly found in daily life. Cross-junction is one of the examples that is commonly found in a high-rise city. In order to study the sound field transmission through a junction in a street canyon, systematic formulations are developed in Chapter 4. The formulae are developed from the coherent image source method. In this model, all source and receiver locations are considered that include (1) both source and receiver are located in same arm of the street junction, (2) source and receiver are located in same street but separated by the junction and (3) source and

receiver located in different arms of the junction and the source cannot “see” the receiver directly. The model can be used to estimate both the steady state sound field and reverberation time. A series of outdoor field measurements was conducted to validate the proposed theory.

The theory in Chapter 4 is further developed to estimate the sound field in a long enclosure with a T-intersection. In the model, the height of the main enclosure and T-intersection are same. The T-intersection is joined by the main enclosure perpendicularly. A sound source is always maintained in the main enclosure and three receiver locations are considered in the study. The receiver is located in same arm of the source, in the main enclosure but separate from the junction to the source and in the T-branch. The theoretical predictions are validated against the published experiments.

Besides the reverberation time, the other key element that affects the speech intelligibility is the background noise level. Literature shows that many noise sources in long enclosures have distinct directional characteristics such as rolling noise and fan noise. Both rolling noise and fan noise are classified as acoustic dipole. In order to study the characteristics of dipole noise source, experimental dipole sound sources

should be prepared before continuing. Chapter 6 reviews the available dipole sources.

Dipole sources are constructed for subsequent experimental studies.

The structure of a dipole field can be considered in terms of a pair of anti-phase monopoles with equal acoustic power, while an acoustic dipole can be modeled as two equivalent monopoles but in anti-phase. Based on this assumption, the dipole sound field in a long enclosure can be obtained by subtracting the total sound field contributed by two virtual monopoles since two virtual monopoles are assumed as totally out of phase. The theoretical calculation, i.e. comparative validations of the predicted results with experimental data is given in Chapter 7. In the real world, most dipole sources are not fully symmetrical, as the sound field that radiates from the front part of the dipole source is not exactly the same as the sound field that radiates on the back part of the dipole source. Theoretical study of the source field propagation of a non-symmetrical dipole source is conducted afterwards. Indoor and outdoor field measurements are also conducted to validate the proposed methodology.

The overall conclusion and findings of the study is given in Chapter 8. Furthermore, some future research is recommended.

Chapter 2

Noise propagation in street canyons

2.1 Introduction

Due to the rapid growth in mechanised transport and transportation systems in the past few decades, noise is one of the most cited environmental factors that are often commonly associated with pollution from transport. Various modes of land transportation are the primary source of noise in densely populated, high-rise cities. An essential feature of compact and high-rise cities is that the scarcity of suitable land has encouraged building development to go up in the vertical dimension. It is common to find residential and commercial tower blocks of over 40 storeys with a height of over 100 m or more. Worse still, the urban areas are typically embedded with a compact traffic network of highways and/or railways with high traffic volume. The lack of available land space means that the residents are closer to noise sources. The tall flanking buildings, which form a street canyon, lead to a large portion of the dwellings to be exposed to the land transportation noise. The noise levels do not decrease significantly with increasing height above the ground in street canyons

[81-84]. The motivation of the current study is to develop a simple formula to evaluate steady-state noise levels and the reverberation times in a street canyon for assessing the effectiveness of noise control.

It is known that the scattering of sound at the façade surfaces is known to be significant for predicting the transmission of noise along a street canyon [35, 42]. The image source model where the boundaries can be taken as smooth, geometrically reflecting surfaces can be used in the present study. This is because this model is simple yet it can be used to represent some urban situations. The closed-form analytical results can be used to offer a first order engineering approximation to supplement the numerical results obtained from other computational intensive schemes, e.g., the diffuse reflection model [37, 38].

In the study, an integral formulation to calculate the noise levels and the reverberation times in street canyons is presented. The theoretical models are validated by comparing the numerical predictions with published experimental data [34], indoor and outdoor experimental results. These measured results are compared with the numerical predictions based on the integral formulations. The outcomes of the present study are summarised at the end of this chapter.

2.2 Theory

2.2.1 Total steady-state sound energy at a receiver

A street canyon may be considered as a category of a long enclosure: the flanking façades are treated as a pair of parallel side walls, the road pavement is taken as the floor, and the opening at the top is represented by a perfectly absorptive ceiling.

Taking the boundaries as geometrically reflecting surfaces, the sound propagation along the street canyon can be calculated by means of an image source method [38].

Figure 2.1 displays an idealised street canyon where h is the height of the buildings measured in the z -direction. The pair of flanking façade surfaces is parallel to each other with a horizontal separation of w measured in the x -direction. The y -axis is aligned along the direction of the street canyon.

The origin is located on the ground equidistance from the parallel flanking buildings where the façade surfaces are situated at $x = \pm w/2$ [50]. In the current study, a typical situation where the height of the flanking façades is greater than the width of the street canyon, i.e., $h > w$ is considered. The effect of diffraction at the top edges of the façades is ignored in the present study. This is because the total sound energy at a receiver point is dominated by the contributions from multiple reflected sound rays of the boundary surfaces. In general, the noise levels due to vehicular noise sources

decrease with an increase in the receiver height because there are no reflections from the open ceiling of the street canyon. In addition, the noise levels decrease with the increase in the separation between the source and receiver along the y-direction. However, Kang [38] showed that the noise levels are relatively uniform between the buildings with a fixed horizontal separation (greater than about $1.5w$) from the source and at a constant height above the ground. Without loss of generality, it can therefore be assumed that a point source S and a receiver R are located at the coordinates of $(0, 0, z_s)$ and $(0, y, z_r)$, respectively. Hence, the sound source is separated from the receiver by a horizontal distance

$$r_l = \sqrt{y^2 + (z_r - z_s)^2} . \quad (2.1)$$

A row of image sources, shown as the upper row in Fig. 2.2, is formed because of the reflections from the two vertical façade surfaces. Based on this series of image sources, the lower row of image sources can be constructed below the $z = 0$ plane due to the reflection from the ground surface. All image sources can be linked to the receiver and the total sound field is computed by summing the contributions from these image sources. Making use of the image source model, the total sound energy at the receiver due to the image sources located above the ground is given by

$$\Lambda_I = \sum_{m=-\infty}^{\infty} \frac{Qe^{m \ln(1-\bar{\alpha}_v) - \alpha_a d_m}}{d_m^2} , \quad (2.2)$$

where Q is the source strength, $\bar{\alpha}_v$ is the mean absorption coefficient of the façade surfaces, and α_a is the air absorption factor, which can be obtained from Ref. 85 for different frequencies. The path length of the $\pm m$ th image source can be determined by

$$d_m = \sqrt{(mw)^2 + r_l^2}, \quad (2.3)$$

where r_l is determined according to Eq. (2.1). Here, in Eq. (2.2), the attenuation due to the reflection from the boundary surfaces is written in its exponential form by noting the following algebraic identity:

$$e^{m \ln(1-\bar{\alpha}_v)} = (1-\bar{\alpha}_v)^m, \quad (2.4)$$

where $\ln(1-\bar{\alpha}_v) < 0$ because $\bar{\alpha}_v < 1$ and m is the number of reflections from the façades.

Suppose that the façades are built with hard surfaces with small $\bar{\alpha}_v$. In this case, the total sound energy received at the reception point is composed of many terms due to the multiple reflections from the façade surfaces. It is possible to replace m with a continuous function in terms of x as

$$m = |x|/w. \quad (2.5)$$

A line source can now be used to replace the upper row of the discrete image sources.

Figure 2.2 shows a schematic of the effective line source. It has an effective strength

of $Q/w \text{ m}^{-1}$ because there is only one image source for the width, w , of the street canyon. The path length d_m can be replaced with

$$D_I = \sqrt{x^2 + r_I^2}. \quad (2.6)$$

From Eq. (2.2), the sound energy at the reception point due to the image sources above the ground can be written in an integral form as

$$\Lambda_I = \frac{\Lambda_0}{w} \int_0^\infty \Phi_I dx, \quad (2.7)$$

where Φ_I is a symmetric function of x given by

$$\Phi_I = \Phi_I(x) = \frac{2e^{\{x \ln(1-\bar{\alpha}_v) / w - \alpha_a D_I\}}}{D_I^2}, \quad (2.8)$$

and Λ_0 is the free-field sound energy received at a distance of 1 m from the point source. It can be determined by

$$\Lambda_0 = Qe^{-\alpha_a(1)} / 1^2 \approx Q. \quad (2.9)$$

The integral in Eq. (2.7) is difficult, if not impossible, to evaluate analytically because of the presence of D_I in the exponential term of $\Phi_I(x)$. Although the integral can be evaluated by a numerical quadrature, it is more convenient to approximate the solution in an analytical form.

To this end, D_I is approximated in the exponential term of Eq. (2.8) by a linear function

$$D_I = \sqrt{r_I^2 + x^2} \approx r_I + K_I x, \quad (2.10)$$

where K_I is the slope of the approximate function. Since the solution is given in an integral form [cf. Eqs. (2.7) and (2.8)], it is convenient to approximate K_I such that

$$\int_0^{X_I} \sqrt{r_I^2 + x^2} dx = \int_0^{X_I} (r_I + K_I x) dx, \quad (2.11)$$

where the upper limit of the integrand, X_I , is set at a sufficiently large distance in order to cover the range of x that contributes to the total sound energy at the reception point. As $\Phi_I(x)$ is a monotonic decreasing function, it can approximate X_I by the following function:

$$\varepsilon = \Phi_I(X_I) / \Phi_I(0), \quad (2.12)$$

where ε is the ratio of the minimum sound energy and the maximum sound energy contributed due to the effective line source. The minimum sound energy is contributed from a source located at $x = X_I$ and the maximum contribution comes from the source located at $x = 0$. Preliminary numerical analyses have suggested that the predicted results are relatively the same for a wide range of ε . Hence, for simplicity, ε is chosen as 1×10^{-6} in the following numerical analyses.

It is remarkable that both integrals in Eq. (2.11) can be evaluated analytically to give closed-form expressions. As a result, K_I can be written in an analytical form to yield

$$K_I = \frac{2}{X_I^2} \left\{ \frac{r_I^2}{2} \left[\ln \left(\frac{X_I + \sqrt{r_I^2 + X_I^2}}{r_I} \right) + \frac{X_I \sqrt{r_I^2 + X_I^2}}{r_I^2} \right] - r_I X_I \right\}. \quad (2.13)$$

Substituting Eqs. (2.8), (2.10), and (2.13) into Eq. (2.7), it can approximate Λ_I by

$$\Lambda_I \approx \frac{2\Lambda_0 e^{-\alpha_a r_I}}{w} \int_0^\infty \frac{e^{-v_I x}}{r_I^2 + x^2} dx, \quad (2.14)$$

where

$$v_I = -\ln(1 - \bar{\alpha}_v) / w + \alpha_a K_I. \quad (2.15)$$

By using the following identity of an indefinite integral for the exponential integral

[86]:

$$\int \frac{e^x}{a^2 + x^2} dx = -\frac{1}{a} \operatorname{Im}\{e^{ia} E_1(-x + ia)\} + \text{const}, \quad (2.16)$$

it can simplify Eq. (2.14) to yield

$$\Lambda_I \approx \frac{-2\Lambda_0 e^{-\alpha_a r_I}}{w r_I} \operatorname{Im}[e^{iv_I r_I} E_1(iv_I r_I)], \quad (2.17)$$

where E_1 is the exponential integral with complex arguments.

The accuracy of Eq. (2.17) is demonstrated by comparing the numerical results obtained by direct numerical integration of Eq. (2.7). Figure 2.3 shows comparisons of these two numerical results in which the relative sound pressure level (SPL) is plotted against the air absorption factor α_a . In the plots, the relative SPL is defined as

$$SPL_r = 10 \log(\Lambda_I / \Lambda_0), \quad (2.18)$$

where Λ_0 is the free-field sound energy at 1 m from the source. In Fig. 2.3, a street

canyon of 3 m wide and 100 m high is used in the numerical calculations. The building façades are assumed as perfectly reflecting surfaces, i.e., $\bar{\alpha}_v = 0$. Numerical results with the horizontal separation between the source and receiver of 5, 15, and 50 m, respectively, are shown. Both source and receiver are located equidistance from façades and at the same height above the ground. It follows from Fig. 2.3 that the numerical results according to both schemes agree very well with each other. These comparisons have demonstrated the accuracy of the approximate model, which is sufficient to estimate the effect of the atmospheric absorption in a street canyon of typical source/ receiver geometrical configurations.

Similarly, an analogous expression for the sound energy due to the image sources located below the ground is derived as follows:

$$\Lambda_G = \frac{\Lambda_0 e^{-\alpha_a r_G}}{w} \int_0^{\infty} \Phi_G dx \quad (2.19)$$

where the subscript G denotes the corresponding parameters for the ground-reflected waves. The symmetric function $\Phi_G(x)$ is given by

$$\Phi_G = \Phi_G(x) = \frac{2(1 - \alpha_G) e^{\{x \ln(1 - \bar{\alpha}_v) / w - \alpha_G D_G\}}}{D_G^2}, \quad (2.20)$$

where α_G is the absorption coefficient of the ground, D_G is the total distance between the receiver and the image sources below the ground

$$D_G = \sqrt{x^2 + r_G^2}, \quad (2.21)$$

and r_G is the corresponding horizontal separation

$$r_G = \sqrt{y^2 + (z_r + z_s)^2}. \quad (2.22)$$

Using an analogous approach, an approximate expression can be derived for the sound energy at the reception point due to the image sources below the ground as follows:

$$\Lambda_G = \frac{-2\Lambda_0(1-\alpha_G)e^{-\alpha_a r_G}}{w r_G} \text{Im}[e^{i v_G r_G} E_1(i v_G r_G)], \quad (2.23)$$

where the parameters v_G and K_G are given by

$$v_G = -\ln(1 - \bar{\alpha}_v) / w + \alpha_a K_G \quad (2.24a)$$

and

$$K_G = \frac{2}{X_G^2} \left\{ \frac{r_G^2}{2} \left[\ln\left(\frac{X_G + \sqrt{r_G^2 + X_G^2}}{r_G}\right) + \frac{X_G \sqrt{r_G^2 + X_G^2}}{r_G^2} \right] - r_G X_G \right\}. \quad (2.24b)$$

By means of the same approach, it is possible to determine X_G by solving an analogous equation [cf. Eq. (2.11)] numerically. However, it is significant that the same term (i.e., $X_G = X_I$) may also be used in Eq. (2.24b) for calculating K_G . A numerical analysis has suggested that a small variation in X_G does not cause a significant change in the numerical values of Λ_G . The details of these numerical analyses are not shown here for brevity.

The total sound energy can now be found by summing the contributions from all image sources (above and below the ground) to give

$$\Lambda_T = \Lambda_I + \Lambda_G, \quad (2.25)$$

where Λ_I and Λ_G are determined by Eqs. (2.7) and (2.19), respectively. It is possible to give a closed-form solution for Λ_T by substituting Eqs. (2.17) and (2.23) into Eq. (2.25) to yield

$$\Lambda_T = \frac{-2\Lambda_0 e^{-\alpha_a r_I}}{w r_I} \text{Im}[e^{i v_I r_I} E_1(i v_I r_I) + A_G (1 - \alpha_G) e^{i v_G r_G} E_1(i v_G r_G)], \quad (2.26)$$

where A_G is a correction factor for the change in distances because the image sources are located below the ground. It is given by

$$A_G = (r_I / r_G) e^{-\alpha_a (r_G - r_I)}. \quad (2.27)$$

If the source is located near the ground and at a large horizontal separation from the receiver (i.e., $r_I \approx r_G$), A_G is approximately equal to unity.

2.2.2 Reverberation time in street canyons

To assess the effect of multiple reflections, it is useful to determine the reverberation times in a street canyon. The problem may be treated as the determination of the transient sound field when the source is either switched on or turned off. According to the principle of reciprocity, it may consider the receiver as the centre of the wave fronts: that is the crests of spherical waves radiating from the receiver, which arrive at different image sources at different times. For convenience, the initial time $t = 0$ is set at the moment when the direct sound wave reaches the receiver R . Suppose that the

source is turned on at time $t = -r_I/c$. Then the position of a wave crest at time $t > 0$ is located at a horizontal distance $x_I(t)$ from the source S . By a simple geometrical consideration, the path length D_I from the receiver to an image source above the ground can be determined by

$$D_I(t) = \sqrt{x_I(t)^2 + r_I^2} = r_I + ct, \quad (2.28)$$

where r_I is given by Eq. (2.1); see Fig. 2.4 for a schematic of the wave crests at time $t = 0$ and at time t .

According to Eq. (2.14), the transient sound energy due to the image sources above the ground can then be written as

$$\Gamma_I(t) = \frac{2\Lambda_0 e^{-\alpha_a r_I}}{w} \int_0^{x_I(t)} \frac{e^{-v_I x}}{r_I^2 + x^2} dx, \quad t > 0, \quad (2.29)$$

since only those sources located in the region $-x_I(t) \leq x \leq x_I(t)$ can contribute to the sound field at the reception point. Equation (2.29) can be reduced to Eq. (2.14) when $t \rightarrow \infty$, i.e., the total transient sound energy $\Gamma_I(\infty)$ becomes the steady-state sound energy at the reception point.

A complimentary situation that the source is originally turned on but it is deactivated at $t = -r_I/c$ where c is the sound speed in air can also be considered. In this case, the transient sound energy at time t is simply given by

$$\Gamma_I^*(t) = \frac{2\Lambda_0 e^{-\alpha_a r_I}}{w} \int_{x_I(t)}^{\infty} \frac{e^{-v_I x}}{r_I^2 + x^2} dx, \quad t > 0. \quad (2.30)$$

The integrals given in Eqs. (2.30) and (2.29) can be evaluated, respectively, to yield

$$\Gamma_I^*(t) = -\frac{2\Lambda_0 e^{-\alpha_a r_I}}{w r_I} \text{Im}\{e^{iv_I r_I} E_1[v_I(x_I + ir_I)]\} \quad (2.31)$$

and

$$\Gamma_I(t) = \Lambda_I - \Gamma_I^*(t), \quad (2.32)$$

where Λ_I is determined from Eq. (2.17).

Similarly, the transient sound energy due to the image source located below the ground can be determined when the source is turned off at $t = -r_I/c$. However, the sound energy starts to decay at a later time at $t = (r_G/r_I)/c$ because r_G/r_I . The transient sound energy is given by

$$\Gamma_G^*(t) = -\frac{2\Lambda_0 e^{-\alpha_a r_G}}{w r_G} \text{Im}\{e^{iv_G r_G} E_1[v_G(x_G + ir_G)]\}, \quad t \geq (r_G - r_I)/c, \quad (2.33)$$

where x_G is determined by the following equation:

$$D_G(t) = \sqrt{x_G(t)^2 + r_G^2} = r_G + ct. \quad (2.34)$$

On the other hand, if the source is activated at $t = 0$, then the transient sound energy is given by

$$\Gamma_G(t) = \Lambda_G - \Gamma_G^*(t), \quad t \geq (r_G - r_I)/c. \quad (2.35)$$

The effect of multiple reflections on street canyons can be assessed by considering the

reverberation times, T_{60} and T_{30} , where T_{60} is the time for the noise level to reduce by 60 dB below the initial level and T_{30} is the decay time for the noise level to drop from -5 to -35 dB. A decay curve in the noise level is normally needed to determine T_{60} and T_{30} . Therefore, it should focus on the transient sound energy when the source is turned off in favour of the transient sound energy when the source is activated. The total transient sound energy can be obtained by summing the contributions from the image sources located above and below the ground. From Eqs. (2.31) and (2.33), we can obtain

$$\begin{aligned}\Gamma_T^*(t) &= \Gamma_I^*(t) + \Gamma_G^*(t) \\ &= -\frac{2\Lambda_0 e^{-\alpha_a r_I}}{w r_I} \text{Im}\{e^{i v_I r_I} E_1[v_I(x_I + i r_I)] + A_G(1 - \alpha_G) e^{i v_G r_G} E_1[v_G(x_G + i r_G)]\}. \quad (2.36)\end{aligned}$$

Since the current formulation is based on the image source method, it is important to demonstrate the validity of the model by comparing the current numerical results with those predicted by the image source model. It is sufficient to show plots of the decay curves with the source turned off at $t = r_I / c$. Figure 2.5 displays these comparisons at different mean absorption coefficients of all boundary surfaces of 0.15, 0.2, 0.25, and 0.3, respectively. The width of 10 m and the source/receiver separation of 10 m are used in the calculations. In the graphs, the relative SPLs are defined as

$$L(t) = 10 \log[\Gamma_T^*(t) / \Gamma_T^*(0)], \quad (2.37)$$

where the reference level $\Gamma_T^*(0)$ is taken as the initial noise level. The source and receiver are placed, respectively, at 0.5 and 5.0 m above the ground and they are located equidistance from the façade surfaces. It can see from Fig. 2.5 that the predicted decay curves according to the image source method and the integral formulation agree tolerably well with each other in all cases.

Using Eq. (2.36), the decay curve can be produced by a reverse-time integration of the transient response. This process is known as the Schroeder approach [54, 87]. The reverberation time T_{60} is then determined by using the rate of decay given by the linear regression with the noise level reducing by 60 dB from the initial level. In other words, T_{60} can be determined for the time when the ratio of $\Gamma_T^*(t)/\Gamma_T^*(0)$ is reduced to 10^{-6} . If the reverberation time T_{30} is required, Eq. (2.37) will be used to obtain the decay curve. A linear regression analysis is conducted to determine the rate of decay for the noise level varying between 5 and 35 dB below $\Gamma_T^*(0)$.

T

2.3 Comparison with experimental measurements

2.3.1 Full scale field measurements in a town street

In the 1970s, Steenackers *et al.* [34] carried out a series of measurements for the reverberation time of typical town streets with their widths varying between 9 and 60

m. An alarm gun was used as an impulsive noise source where the sound decay curves were measured. The reverberation time was then used to estimate the sound absorption coefficient of the town street. Their experimental data [34] will be used to validate the integral expression given in Eq. (2.36). It also compares the numerical results based on the image source model with geometrically reflected boundary surfaces [38].

Figure 2.6 displays the measured time histories of the relative SPLs adapted from the published data [34]. They were the sound level decay curves in the town streets with the respective widths of 12, 18, and 40 m. The horizontal distances between the source and receiver for all measurements, which were estimated from the experimental data, were 10 m. Since the exact locations of the source and receiver are not available in Ref. 34, they were assumed to be placed at 1.2 m above the ground and equidistance from the flanking buildings.

To confirm the validity of this assumption, a prior numerical analysis is conducted to examine the effect of the source location on the SPLs at different receiver locations along the street canyon. It is found that the sound fields are generally uniform within the same cross sections of the street canyon, especially, when the source and receiver are close to the ground and their horizontal separation is sufficiently large. These

numerical simulations are not shown here but this finding is in agreement with the conclusion suggested by Kang [38]. With these prior numerical simulations, it can be expected that their assumption on the source/receiver locations will be sufficient to give accurate predictions of the sound fields in the street canyons.

In addition to the published data, Fig. 2.6 also presents the numerical predictions according to the image source model [38] and the current formulation. In his numerical analyses, Kang [38] also used the incoherent model but he computed the overall SPL by summing the contributions from all image sources, which have been “switched” on. The number of image sources increases discretely to its steady-state level after the first arrival of the direct wave. The number of “switched-on” image sources reaches its maximum level after a short duration. Hence, the image source model predicts a step change in the sound energy level shortly after the first arrival time but time-varying sound energy will gradually become the steady-state level as the time increases.

In the numerical calculations of all town streets, the air absorption factor is assumed as zero because no pertinent information is provided for the atmospheric conditions during the measurement periods. In Fig. 2.6(a), the predicted and measured results for

the town street 12 m wide are presented. According to Steenackers *et al.* [34], the ground was assumed to be a perfectly reflecting surface and the average mean absorption coefficient of the building façades was 0.15. For the given source and receiver locations, Eq. (2.37) is used to evaluate the time history of the relative SPLs. The numerical predictions according to the image source model and the integral formulation agree to within 1.1 dB in the relative SPL. Furthermore, both predicted results show good agreements with the experimental data.

Figure 2.6(b) presents a set of data taken from Fig. 1 of Ref. 34 where the width of the town street was 18 m. The estimated sound absorption coefficient, which was taken from Table I of Ref. 34, was 0.17. Again, Eq. (2.37) is used to calculate the time histories of the relative SPLs. The average discrepancy between the measured data and the image source model is 1.21 dB while it is 1.15 dB for the integral formulation.

The compared results for the last set of data are displayed in Fig. 2.6(c). Based on the information obtained from Steenackers *et al.* [34], it estimated that the mean absorption coefficient of the façade was 0.3. Figure 2.6(c) shows tolerably good agreements between the measured data and the numerical results according to both prediction methods. The average discrepancies between the image source method and

measured results are 1.54 and 1.35 dB for that of the integral formulation.

By comparing with published experimental data, the validity of the analytical formulation for predicting the relative SPL in a street canyon can be confirmed. The proposed model provides a simple closed-form solution, which compares well with the standard image source model and with the published experimental results.

2.3.2 Indoor model experiments

A model street canyon was built and placed in an anechoic chamber with internal dimensions of 6 x 6 x 4 m³ (high). Hard plywood boards of 20 mm thickness were used to construct the model street canyon of 0.8 m wide, 5 m long, and 2.6 m high.

The hard plywood boards were varnished to prevent leakage of sound. To simulate the façade surfaces with finite impedance, the two vertical walls were covered with acrylic light diffusers of 5 mm thickness; see Fig. 2.7. The light diffusers had rectangular grids with dimensions of 15 x 15 mm² and open volumes. The light diffusers may give diffused sound fields but, nevertheless, Daigle *et al.* [88] demonstrated experimentally that a hard ground covered with light diffusers can be used to simulate an indoor impedance plane. In light of the suggestion of Daigle *et al.* [88], a set of short-range measurements for the propagation of sound above the hard

plywood board covered with and without light diffusers has been conducted. In these measurements, the source and receiver were placed at a horizontal separation of 1 m and at heights of 0.01 m above the model ground.

Figure 2.8(a) shows a typical measured spectrum to demonstrate the interference effects due to the direct and reflected waves for sound propagation above the model impedance ground. The excess attenuation, which is defined as the ratio of the total field above the impedance surface to the free-field measurement at 1 m in the anechoic chamber, is plotted against the source frequency in Fig. 2.8(a). Similar measurements have been conducted also for the propagation of sound over the hard plywood board. Its measured excess attenuation spectrum is shown in Fig. 2.8(b). From both graphs in Fig. 2.8, there are clear interference dips due to the interference of the direct and reflected waves although the primary dip occurs at higher frequency for the hard ground. This is because the impedance of a hard surface is usually higher than that of the model plane with finite impedance. From these two sets of short-range measurements in the anechoic chamber, the suitability of treating the plywood board covered with light diffusers as a model impedance plane can be confirmed.

The measured excess attenuation spectra in Fig. 2.8 has been used to determine the

acoustic impedances of the plywood board with (impedance façade surfaces) and without (hard ground surfaces) the cover of light diffusers. Attenborough's two-parameter model [89] was used to characterise the surface impedances, Z , of the vertical wall and the ground in the present study. The surface impedance is calculated by

$$Z = 0.538\sqrt{\sigma_e/f} + i[0.538\sqrt{\sigma_e/f} + 19.74\alpha_e/f], \quad (2.38)$$

where f is the source frequency, σ_e is the effective flow resistivity, and α_e is the effective rate of change in porosity with depth. The parametric values of σ_e and α_e are deduced from the short-range propagation measurement over the surface.

The best-fit parametric values for σ_e and α_e were 80 kPa s m⁻² and 450 m⁻¹ for the vertical walls (plywood boards covered with light diffusers) and 80 000 kPa s m⁻² and 50 m⁻¹ for the ground made of the plywood board. These parametric values for different boundary surfaces used in the numerical simulations are summarised in Table 2.1 for the ease of reference. Figure 2.8 also shows typical predicted excess attenuation spectra for the propagation of sound above the vertical walls and the ground where their impedances are calculated by using Eq. (2.38) with the parametric values given in Table 2.1.

For the image source model and the current integral formulation, the one-third octave band absorption coefficients (α) of the boundary surfaces are calculated from the measured impedance by [54]

$$\alpha = \frac{|Z - 1|^2}{|Z + 1|^2} . \quad (2.39)$$

Using the Attenborough two-parameter impedance model [89], the absorption coefficients of the ground and vertical walls in one-third octave bands are calculated and listed in Table 2.2.

In indoor measurements, a Renkus-Heinz PN 61 self-powered loudspeaker was used as the source and a “B&K” 4189 pre-polarized free-field 1/2 in. condenser microphone was used as the receiver. A PC-based maximum length sequence system analyser (Ref. 90) was used as both signal generator for the source and data analyser of the measurements. The source strength was characterised by conducting prior measurements to measure its SPL at 1 m free field in the anechoic chamber. In the present indoor experiments, results for steady-state SPLs at various horizontal distances at different frequency bands are presented. The source was located at 0.545 m away from the left vertical wall and at heights varying between 0.10 and 2.1 m. For the receiver, it was also situated at 0.545 m from the left vertical wall and 0.2 m above the ground.

Figure 2.9 shows the typical spectra of the steady-state SPLs where the receiver was located at 2 and 4 m from the source. The source and receiver were, respectively, placed at 0.6 and 0.2 m above the ground and at the same distance of 0.545 m from the left vertical wall. The graphs compare the measured spectra with the numerical predictions according to the integral formulation. The measured and numerical predictions agree reasonably well with each other except for one or two individual one-third octave bands, e.g., a discrepancy of about 5 dB was found for 3150 Hz in the 2 m separation and about 7 dB for 5 kHz in the 4 m separation. It is also observed that the integral formulation can predict the general trend of the measured spectral SPLs. The average discrepancies in the one-third octave bands were found to be 1.9 and 2.7 dB, respectively, for the 2 and 4 m separations.

The variation of the steady-state SPL with the horizontal separation is shown in Fig. 2.10 where four sets of typical results for the frequencies of 500 Hz, 1.25 kHz, 2.5 kHz, and 5 kHz are presented. The relative source/receiver positions with the ground and with the vertical walls are the same as in Fig. 2.9. These plots serve to highlight the capability of the integral formulation in predicting the general trend of measured data for the indoor model experiments.

Before end of this section, it is worth pointing out that there were other studies [91, 92] examining an improved technique for simultaneously selecting both an optimal scale factor and optimal model materials for use in indoor scale model experiments. However, there is no attempt to select the most appropriate materials for modelling the façade surfaces in the present study. The use of a model impedance plane is sufficient to validate the integral formulation by comparing its predicted SPLs with the precise indoor measurements [93].

2.3.3 Outdoor field measurements in an alley street

To confirm the versatility of the integral formulation, a further set of full scale field measurements in an alley street was conducted. The alley street was 3.13 m wide, 20 m long, and the height of the two parallels was 54 m. It had a concrete ground and both vertical walls were covered with hard mosaic tiles. The same set of instruments for indoor measurement was used in outdoor measurements again. Figure 2.11 shows the experimental setup in the alley street. In the experiments, the source was located at the centre of the alley street and 0.1 m above the ground. The receiver was placed at a height of 1.6 m above the ground and at 0.69 m from one of the vertical walls. The distance between source and receiver was adjusted between 1 and 20 m. In the measurement, one end of the alley street was connected to a truck road. The wide of

the truck road was much greater than the wide of the alley street. Then, most of reflecting sound waves went into the truck road when they arrived the end of the street. Furthermore, previous long enclosure study found that, the effect of end walls on the sound attenuation was in-significant [94]. The sound field reflection from end of the alley street was neglected in this study.

Prior *in-situ* measurements were conducted to determine the sound absorption coefficient of the vertical walls and the ground. The source and receiver were placed at 0.01 m above the respective surfaces and their horizontal separation was set at 1 m in these measurements. Again, the Attenborough two-parameter impedance model [89] was used to characterise the respective impedances of the surfaces and their parametric values are listed in Table 2.1. All these boundary surfaces were made of acoustically hard construction materials, which led to fairly high parametric values for σ_e according to the short-range characterisation measurements.

The sound absorption coefficients of the concrete ground and the vertical walls covered with mosaic tiles can then be calculated according to Eq. (2.39). These absorption coefficients, which are listed in Table 2.2, will then be used in subsequent calculations of the reverberation times and SPLs in the alley street.

During the measurement, the outdoor temperature was about 30° C and the relative humidity was 80%. The air absorption factors which are used in the following predictions are obtained from Ref. 85. The air absorption coefficients at different frequency bands are listed in Table 2.2. Due to the relatively high background noise levels in the field measurements, the reverberation time T_{30} was measured in favour of T_{60} . The SPL of the loudspeaker was measured at 1 m free field in the anechoic chamber before the field measurements. It was used to compare with the SPLs measured in the alley street.

Figure 2.12 shows the experimental data of T_{30} in one-third octave bands for the source and receiver located along the alley street. The numerical predictions of reverberation times for horizontal separations of 4 and 12 m are compared with the measured data. The numerical results according to the integral formulations are also shown in Fig. 2.12. It is shown that the numerical predictions can only give an estimation of the general trend of T_{30} as the source frequency increases. Comparison of results for other source/receiver separations was generally similar to those shown in Fig. 2.12 but they are not shown here for succinctness. In this set of data, the source and receiver are placed at respective heights of 0.1 and 1.6 m above the ground. They are located at respective distances of 1.56 and 0.69 m from one of the vertical walls.

Figure 2.13 displays the variations of reverberation times with the horizontal separation. The source/receiver positions relative to the vertical walls and the ground are the same as above. Numerical results and measured data are presented for the source frequencies of 800 Hz, 1.6 kHz, 2 kHz, and 4 kHz. Similar results are also obtained for other frequencies but only four frequencies are selected for presentation. As shown in the plots, the predicted T_{30} varies marginally along the horizontal range (up to 15 m) although the experimental data show a fluctuation in T_{30} . In general, the integral formulation can predict the average level of measured T_{30} over the range of interest.

Subsequently, the same source/receiver geometries as above are used for the next two sets of the experimental measurements. In the first set of data, the predicted and measured spectra for the steady-state SPLs are compared in Fig. 2.14 for the respective horizontal separations of 4, 12, and 20 m. Apparently, the numerical predictions according to the integral formulation give reasonably good agreements with the general trends of the measured frequency spectra in all cases. In the second set of data, the variations of steady-state SPLs with the horizontal range were shown in Fig. 2.15 for the respective frequencies of 500 Hz, 800 Hz, 2 kHz, and 4 kHz. Again, the predicted results show tolerably good agreements with the general trend for

the reduction in the SPLs when the separation between the source and receiver increases.

2.4 Summaries

By modelling a street canyon as a long enclosure with an open top, it is possible to use an energy approach to sum the contribution from all image sources incoherently. In the present study, an integral formulation has been developed to estimate the noise levels in a street canyon by replacing the discrete image sources with an effective line source. The integral formulation is used to predict the decay curve of sound energy where the reverberation time in the street canyon can be estimated. Based on the reverberation time, the steady-state SPLs in the street canyon can be calculated. It has been demonstrated that the predictions according to the integral formulation agreed reasonably well with published data conducted in a town street. The numerical results according to the integral formulation also show good agreements with indoor and outdoor experimental data obtained in the present study. The integral formulation can be used to provide an efficient model for predicting noise levels and the reverberation effect in a street canyon. Moreover, the integral formulation is a simple closed form solution. It is much useful than a numerical model in practice especially for daily application.

Tables

	$\sigma_e / \text{kPa s m}^{-2}$	α_e / m^{-1}
Indoor façade	80	450
Indoor ground	80000	50
Outdoor façade	50000	500
Outdoor ground	200000	500

Table 2.1: The best fit parametric values of the effective flow resistivity (σ_e) and the effective rate of change of porosity with depth (α_e) for predicting the acoustic impedance of the boundary surfaces used in the indoor and outdoor experiments.

Numerical Models for Sound Propagation in Long Spaces

Frequency (Hz)	400	500	630	800	1000	1250	1600
Absorption coefficient (Indoor façade)	0.07	0.09	0.11	0.14	0.18	0.21	0.25
Absorption coefficient (Indoor ground)	0.026	0.028	0.032	0.036	0.04	0.045	0.05
Absorption coefficient (Outdoor façade)	0.028	0.03	0.036	0.041	0.046	0.052	0.059
Absorption coefficient (Outdoor ground)	0.011	0.013	0.014	0.016	0.018	0.020	0.023
Air absorption (30°C, 80% R.H.) / dB per km	1.98	2.79	4.14	5.66	7.41	9.28	11.2
Frequency (Hz)	2000	2500	3150	4000	5000	6300	8000
Absorption coefficient (Indoor façade)	0.29	0.32	0.34	0.36	0.37	0.36	0.35
Absorption coefficient (Indoor ground)	0.056	0.062	0.07	0.079	0.088	0.098	0.11
Absorption coefficient (Outdoor façade)	0.067	0.075	0.084	0.094	0.11	0.12	0.13
Absorption coefficient (Outdoor ground)	0.026	0.028	0.032	0.036	0.04	0.045	0.05
Air absorption (30°C, 80% R.H.) / dB per km	13.3	15.7	18.8	23.1	29.7	39.8	55.7

Table 2.2: The estimated mean absorption coefficients of the boundary surfaces and the absorption coefficient of air at 30°C and 80% relative humidity given in dB per kilometre.

Figures

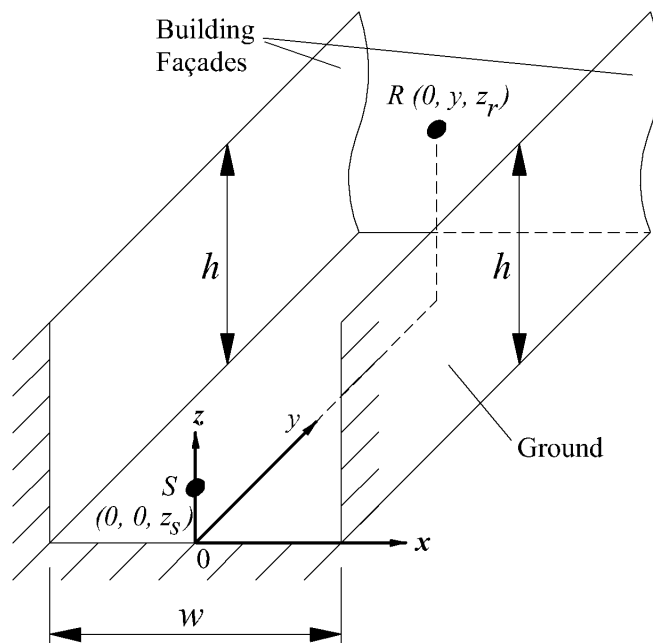


Fig. 2.1: Schematic diagram showing the rectangular coordinate system and the geometrical configuration of a street canyon.

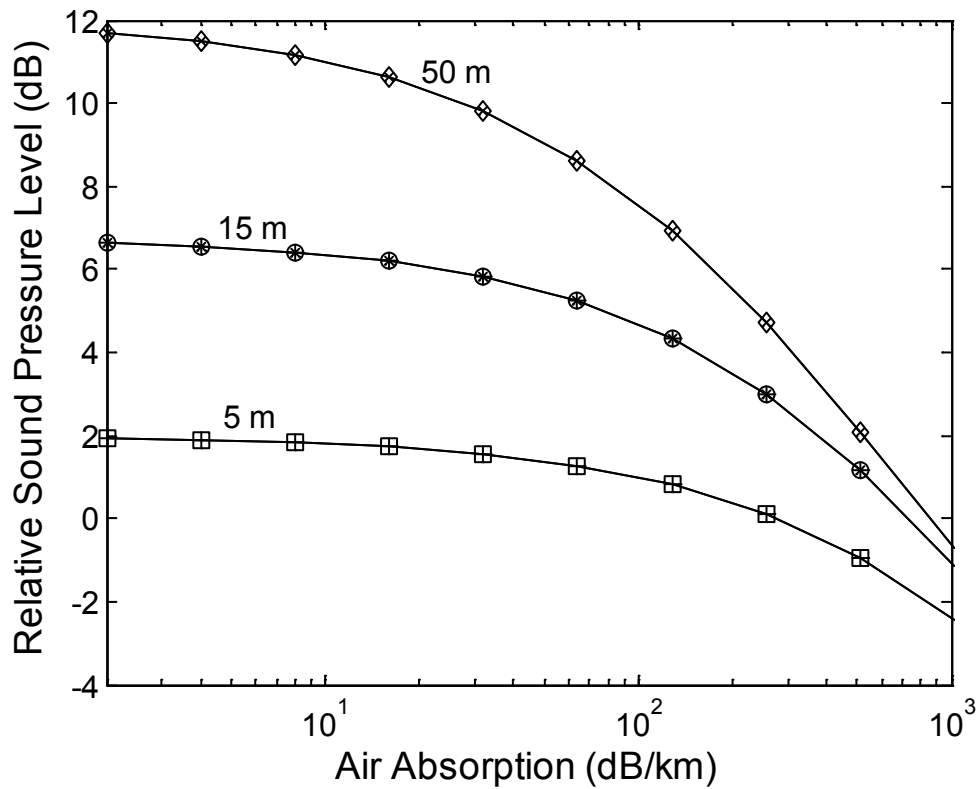


Fig. 2.3: The relative sound pressure level is plotted versus the absorption factor in air.

The squares, circles and diamonds are the numerical results based on the direct numerical integration of Eq. (2.7) for the source/receiver separation of 5 m, 15 m and 50 m respectively. The plus, asterisks and crosses are the corresponding results based on the approximate formula given in Eq. (2.17). The source and receiver are located at the centre line of the street canyon and at the same height above the ground. The reference sound pressure level is taken as 1 m free field sound pressure level, see Eq. (2.18).

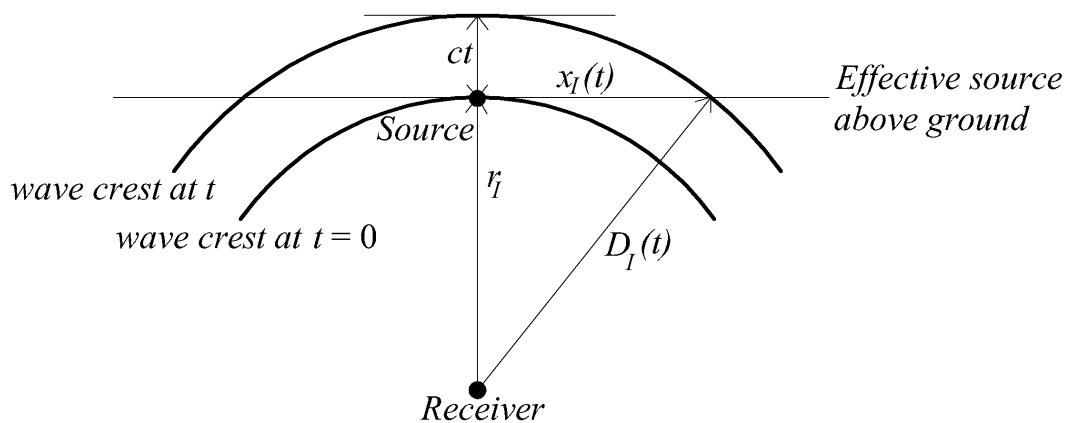


Fig. 2.4: Schematic diagram to show the wave crests centring at the receiver at time $t = 0$ and at time t .

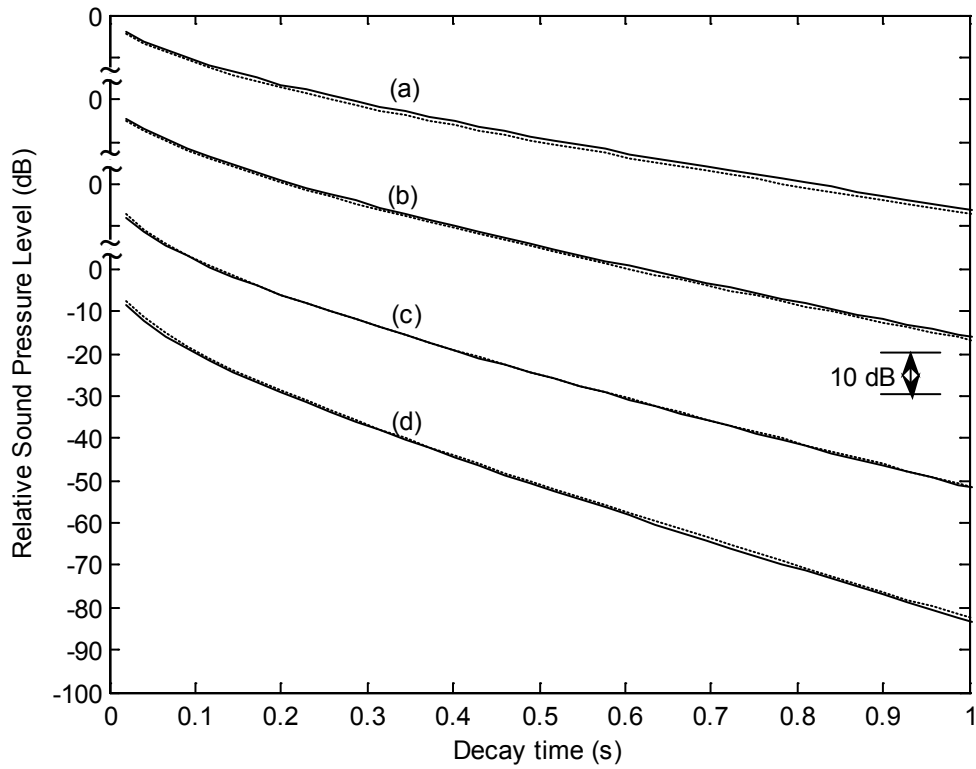


Fig. 2.5: The relative sound pressure level is plotted versus time in a street canyon with the width of 10 m, and the source/receiver separation of 10 m. The source and receiver are placed, respectively, at 0.5 m and receiver at 5 m above the ground and they are located equidistance from the façade surfaces. The mean absorption coefficients of all boundary surfaces are the same at (a) 0.15, (b) 0.2, (c) 0.25, and (d) 0.3. The solid lines (—) are the predictions by the integral formulation and the dotted lines (····) are the predictions by the image source method. The reference sound pressure level is taken at the initial time when the source is turn off, see Eq. (2.37).

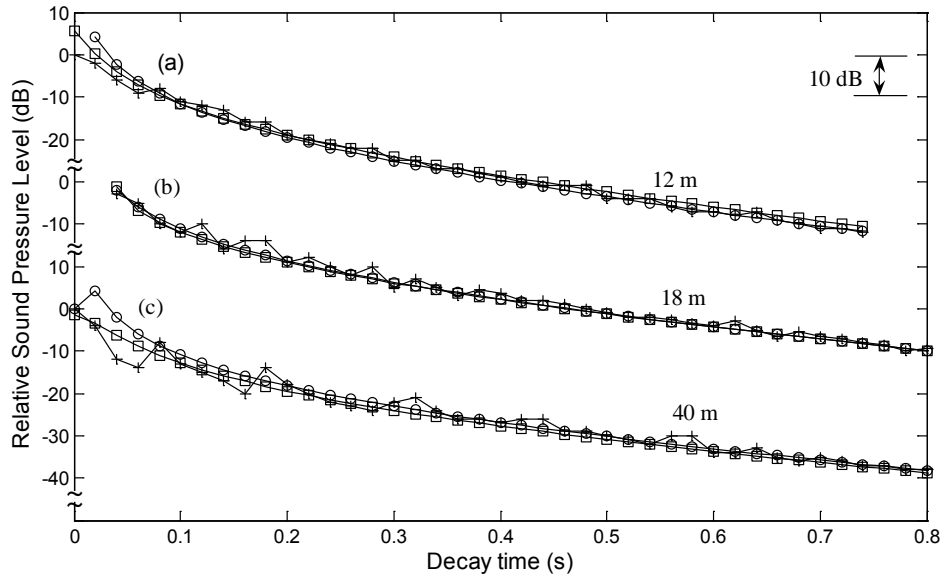


Fig. 2.6: The relative sound pressure level is plotted versus time in town streets with the source/receiver separation of 10 m and the source and receiver were located at 1.2 m above the ground. The width of the town street is (a) 12 m, (b) 18 m, and (c) 40 m. The lines with plus signs (+) are measurement results taken from Ref. 34. The lines with squares (\square) are predictions by the integral formulation. The lines with circles (O) are predictions by the image source method. The reference sound pressure level is taken at the initial time when the source is turn off, see Eq. (2.37).



Fig. 2.7: Photograph showing the set-up of the indoor experiment conducted in an anechoic chamber.

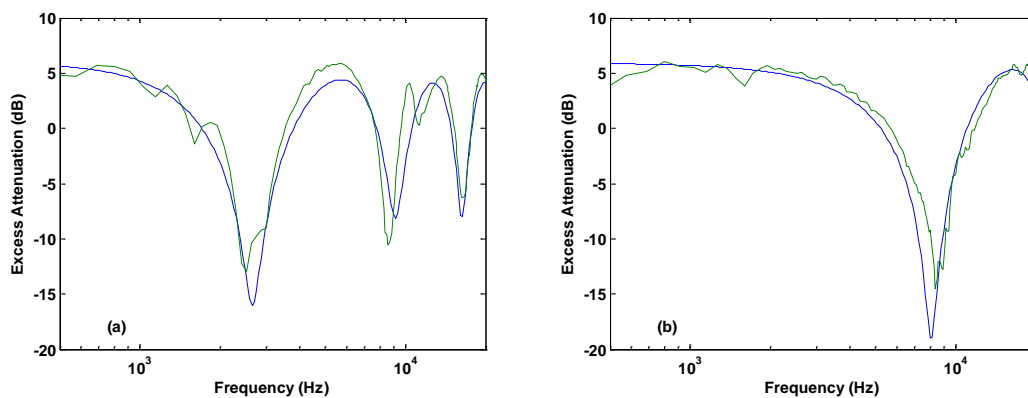


Fig. 2.8: The acoustic characterisation of (a) the vertical walls (indoor façades) and (b) the hard floor (indoor ground). The two-parameter model was used to characterise the surface impedances. These parametric values are listed in Table 2.1 for information. The solid lines (—) are theoretical predictions and the dotted lines (-----) are experimental data.

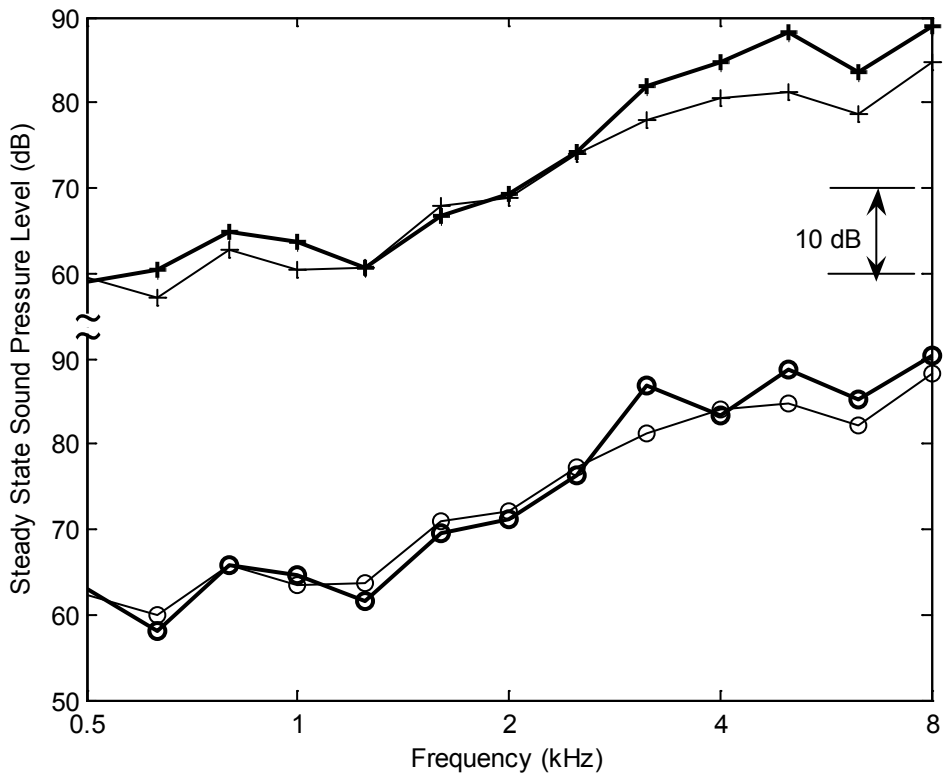


Fig. 2.9: The sound pressure level spectra for the indoor model experiments. The source was located at 0.6 m above the ground and at 0.565 m from one side of the vertical wall. The receiver was placed at 0.2 m above the ground and 0.215 from the same wall. The thick solid lines are experimental data and the thin solid lines are predictions by the integral formulations. The lines with open circles and plus signs are for the horizontal separations of 2 m and 4 m respectively.

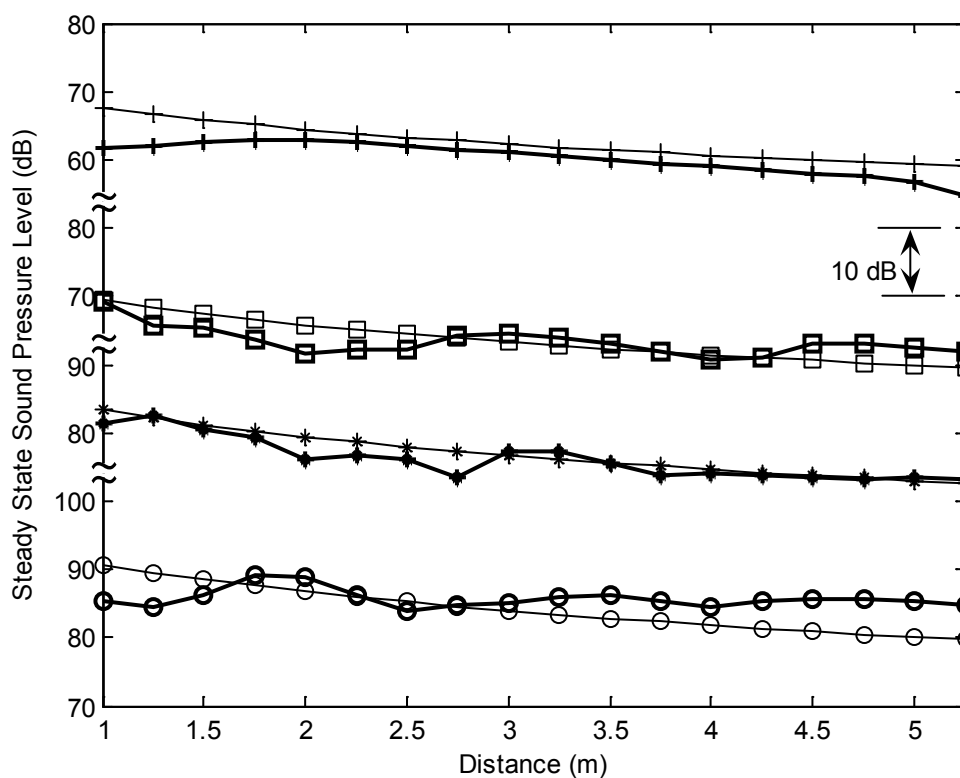


Fig. 2.10: The sound pressure level is plotted versus the horizontal distance. The source and receiver locations are the same as Fig. 2.9. The thick solid lines are for experimental data and thin solid lines are for predictions by the integral formulation. (Plus signs: 500 Hz; squares: 1.25 kHz; asterisks: 2.5 kHz; open circles: 5 kHz).



Fig. 2.11: Photograph showing the experiment setup of the field measurements in an alley street.

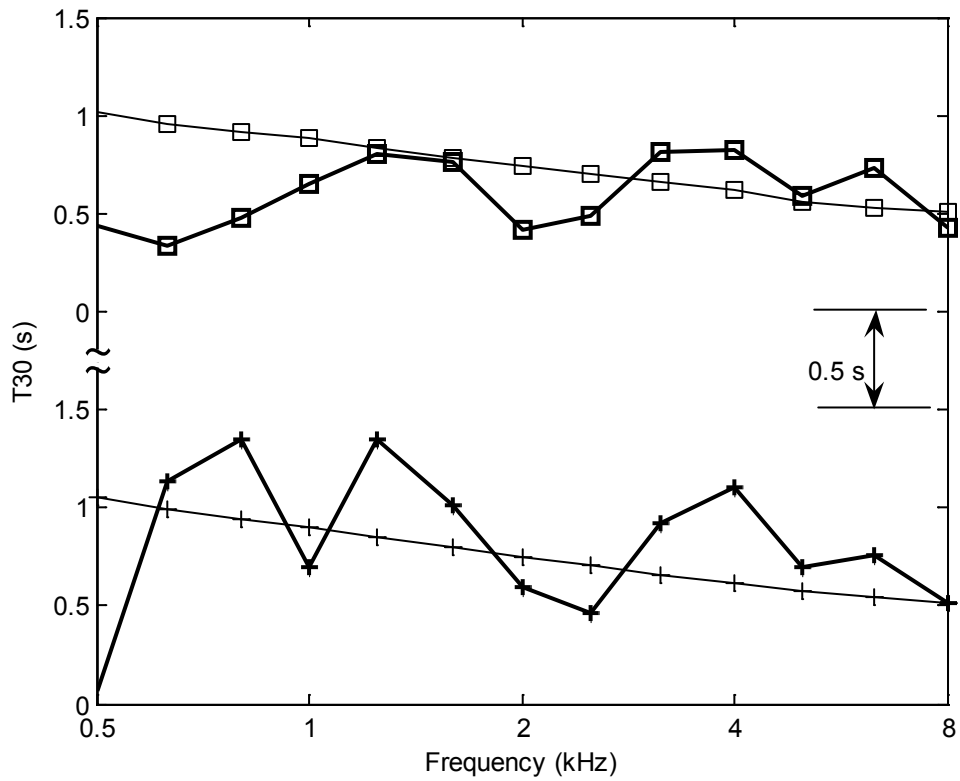


Fig. 2.12: The reverberation time, T_{30} , is plotted versus the source frequency where the source is placed at 0.1 m above the ground and at 1.56 m from one side of the vertical wall. The receiver was located at 1.6 m above the ground and 0.69 from the same vertical wall. The thick solid lines are for experimental data and thin solid lines are for predictions by the integral formulation. (Plus signs: source/receiver separation of 4 m; squares: source/receiver separation of 12 m).

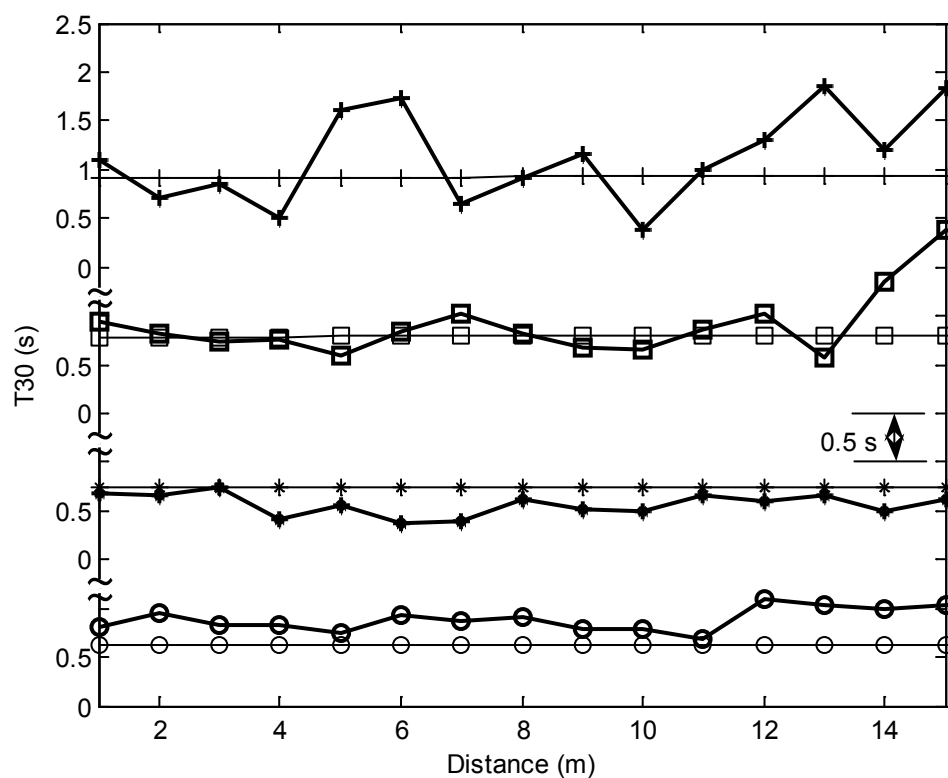


Fig. 2.13: The reverberation time, T_{30} , is plotted versus the distance. The source and receiver have the same relative positions from the vertical walls and the ground as described in Fig. 2.12. The thick solid lines are for experimental data and thin solid lines are for predictions by the integral formulation. (Plus signs: 800 Hz; squares: 1.6 kHz; asterisks: 2 kHz; open circles: 4 kHz).

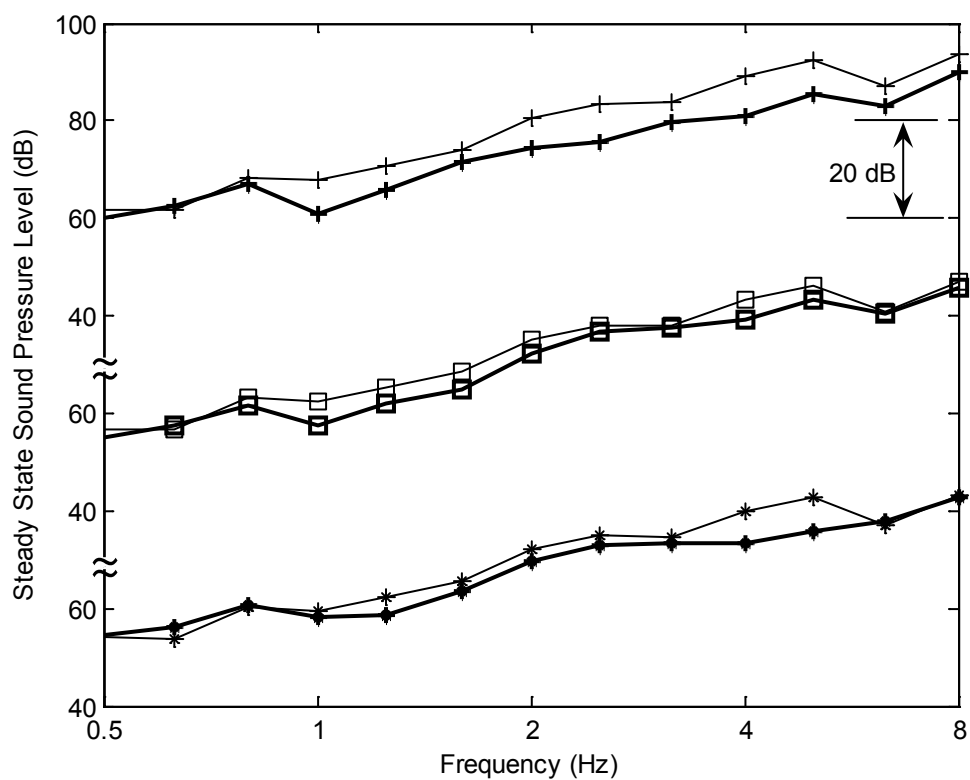


Fig. 2.14: The steady-state sound pressure level is plotted versus the source frequency with the same source/receiver geometry as Fig. 2.12. The thick solid lines are for experimental data and thin solid lines are for predictions by the integral formulation. The respective source/receiver separations are 4 m (plus signs), 12 m (squares) and 20 m (asterisks).

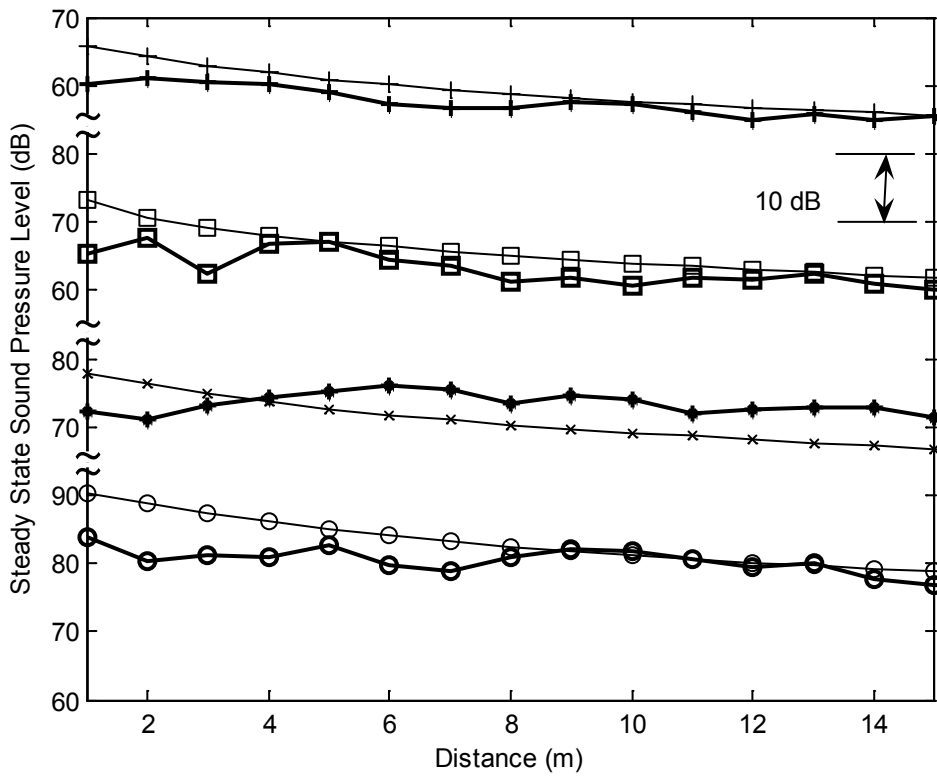


Fig. 2.15: The steady-state sound pressure level is plotted versus the distance. The source/receiver geometry is same as Fig. 2.13. The thick solid lines are for experimental data and thin solid lines are for predictions by the integral formulation. (Plus signs: 500 Hz; squares: 800 Hz; asterisks: 2 kHz; open circles: 4 kHz.)

Chapter 3

An analytical model for predicting sound propagation in long enclosures

3.1 Introduction

Sound pressure level (SPL) is one of factors that indicate the acoustic environment of an enclosed area. It is frequently used for determining the quality of sound perception because it reflects the level of sound absorption in an enclosed space, affects the speech intelligibility, clarity index and definition. Houtgast and Steeneken [1 - 2] developed the so-called modulation transfer function. This was based on the reverberation time and useable sound pressure level to background noise level and it is used to assess the quality of speech transmission in a communications channel. Their method established a physical parameter known as the speech transmission index (STI) that is commonly used today for rating the intelligibility of a sound source.

It is worth noting that the assumption of diffuse field [4] has been used for more than a century to predict the reverberation time. From the reverberation time, the steady-state

sound field of an enclosed area can be obtained [5]. Based on this assumption, related studies were carried out to improve the prediction accuracy in different room environments [18 – 21]. More recently, the ray tracing technique and the image source method are two popular approaches that have been used to develop numerical models for predicting sound propagation in rooms [23 – 25]. Despite these efforts, the sound pressure level obtained from the simplest formula is still used today [4 - 5], especially, in the preliminary design stage because of its simplicity and ease of application. It can give a reasonable estimate of the steady state sound pressure level in rooms.

Due to the extreme dimensions of a long enclosure, where one dimension is much larger than the other two, those classical assumptions of diffuse field do not hold [46]. Studies that focus on long enclosures can be dated back to the 1960s with a number of investigations relating to sound propagation having been conducted [6, 34, 44]. Most of the theoretical formulas are developed either from the image source method or from a ray tracing model [47, 49, 50, 54, 93].

In acoustic design, steady state sound pressure level plays the important rules. Although most of methods described above can give an accurate estimate of steady state sound pressures directly or indirectly, they did not provide any closed form

solution. The present study forces the process to be simplified by developing simple empirical formulas to predict the steady state sound pressure level in long enclosures.

3.2 Theory

In the current study, the long enclosure is modeled to have a rectangular cross section and to be of infinite length. It is constructed of two parallel sidewalls and two parallel horizontal planes, the ground and ceiling. Based on the idea of the image source method, all boundaries of walls are assumed to be geometrically reflective. The effect of diffusion due to boundary surfaces is generally ignored.

3.2.1 Sergeev's model

In 1970s, Sergeev [44] proposed that the scattered sound field can be represented by an array of infinite image sources for both one-dimensional enclosures, e.g. a city street and two-dimensional enclosures, e.g. a tunnel. Each of these image sources contributes incoherently to give the total sound energy for a distant observer. The real source is assumed to be located at a half way point between the horizontal and vertical planes. By summing contributions from all image sources incoherently, Sergeev approximated the solution in an integral form that led to a closed form analytical solution. He further suggested that the sound energy density of image sources

contribution for two-dimensional enclosure can be divided into four patterns.

First, when the receiver is very close to the source (i.e. $X = z/\overline{R}_\varphi \leq 1$ where z is the source-receiver distance, $\overline{R}_\varphi = \pi S / 2(w+h)$, S is the cross-sectional area of the rectangular enclosures $S = wh$, w is the tunnel width and h is the tunnel height), sound energy density contributed by image sources at the receiver, w_s , is almost constant. It can be calculated by,

$$w_s = -\frac{K}{2cS} \ln \alpha \quad (3.1)$$

where K is the sound power of the real source, c is the sound speed in air and α is the absorption coefficient of the boundary surfaces.

For intermediate separations between the source and receiver (i.e. when $X > 1$, $(\alpha + M\overline{R}_\varphi)X \ll 1$, where M is the air absorption factor), w_s can be estimated by,

$$w_s \approx \frac{K}{2cS} \left[-0.6 - \ln(\alpha + M\overline{R}_\varphi)X \right]. \quad (3.2)$$

For longer separations when $X \sim 1/(-\ln(1-\alpha) + M\overline{R}_\varphi)$, w_s is given by

$$w_s \approx \frac{K}{2cS} \frac{\sqrt{3}}{2X} \frac{1}{1 - (1-\alpha)\exp(-M\overline{R}_\varphi)} \exp\left[-\frac{2}{\sqrt{3}}(M\overline{R}_\varphi - \ln(1-\alpha))X \right] \quad (3.3)$$

Finally, when $X \gg 1/(-\ln(1-\alpha) + M\overline{R}_\varphi)$, w_s can be approximated by

$$w_s \approx \frac{K}{16cS} e^{-(d+M\overline{R}_\varphi)X} \quad (3.4)$$

and the sound pressure level can be calculated from the sound energy density by

$$SPL_z = 10 \log(\rho c^2 w_s) \quad (3.5)$$

Although Sergeev suggested a method of estimating the decay of the sound field due to a point in a long enclosure, he did not offer any experimental measurements to validate his formulation.

3.2.2 Kang's image source method

By applying an image source model, Kang [47, 94] proposed two analogous methods to predict the reverberation time in a long enclosure. The first approach is referred to as the summation method: contributions of all image sources are considered and summed to yield an equivalent continuous sound level of an impulse response at the receiver. The second approach is known as the statistical method and was developed to simplify the process used in the summation method for estimating the contributions from all image sources.

Referring to figure 3.1, an infinite long enclosure with the width of w and the height of h , if a point source is positioned at a distance L_w from a side wall and L_h from the ceiling, the receiver is at the centre of the cross-section and the source-receiver separation is z , while the distance between an image source (m, n) and the receiver is

$$D_z \equiv D(z, m, n) = \sqrt{[w|m - g(m)| + 2L_w \operatorname{sgn}(m)g(m)]^2 + [h|n - g(n)| + 2L_h \operatorname{sgn}(n)g(n)]^2 + z^2} \quad (3.6a)$$

where m and n are integers ranging from $-\infty$ to ∞ , $\operatorname{sgn}(\)$ is a sign function defined as

$$\operatorname{sgn}(x) = \begin{cases} -1 & \text{if } x < 0 \\ 1 & \text{if } x > 0 \end{cases} \quad (3.6b)$$

and the function g is given by

$$g(I) = \begin{cases} 1 & \text{if } I \text{ is an odd integer} \\ 0 & \text{if } I \text{ is an even integer} \end{cases} \quad (3.6c)$$

The scattered sound energy and the sound pressure level (SPL_z) contributed by the image source (m, n) at the reception point is given, respectively by,

$$E_z \equiv E(z, m, n) = K(1 - \alpha)^{|m|+|n|} / D_z^2 \quad (3.7)$$

$$SPL_z = 10 \log \left[K(1 - \alpha)^{|m|+|n|} / D_z^2 \right] \quad (3.8)$$

where K is a constant relating to the sound power of the source, and α is the absorption coefficient of the boundaries. The arrival time, $t_z \equiv t(z, m, n)$, of the reflected waves for an image source (m, n) at the reception point with a horizontal separation of z can be determined by

$$t_z \equiv t(z, m, n) = T_D + (D_z - z) / c \quad (3.9)$$

where T_D is the arrival time of the direct sound wave and c is the speed of sound. For a finite duration between time t and $t + \Delta t$, a short time equivalent continuous sound pressure level of the energy responses at the receiver is

$$SPL(t)_z = 10 \log \left[\sum_{m=-\infty}^{\infty} \sum_{n=-\infty}^{\infty} E_z \exp(-MD_z) \right] \quad (3.10)$$

where M is the air absorption factor which can be calculated by ANSI table [85].

In order to simplify the above calculation, the statistical method also has been developed by Kang. The idea of the statistical approach is as follows:

- find out the average image distance D_0 ,
 - approximate the number of image sources N , that contributes in the period Δt ,
- and
- the average number of reflections of image sources r between time t and $t + \Delta t$.

When the source and receiver are located at the centre of the cross-sectional area (figure 3.2), D_0 , N and R can be calculated straightforwardly by,

$$D_0 = c \left(\frac{z}{c} + t + \frac{1}{2} \Delta t \right) \quad (3.11)$$

$$\begin{aligned} N &= \frac{1}{S} \left\{ \pi \left[c^2 \left(\frac{z}{c} + t + \Delta t \right)^2 - z^2 \right] - \pi \left[c^2 \left(\frac{z}{c} + t \right)^2 - z^2 \right] \right\} \\ &= \frac{\pi c^2}{S} \left[2 \left(\frac{z}{c} + t \right) + \Delta t \right] \Delta t \end{aligned} \quad (3.12)$$

$$R = \frac{2\Delta \mathcal{G}}{\pi} \sum_{\mathcal{G}=0, \text{step:}\Delta \mathcal{G}}^{\pi/2} \left(\frac{D_p \sin \mathcal{G}}{h} + \frac{D_p \cos \mathcal{G}}{w} \right) \quad (3.13)$$

The term z/c in equations (3.11) and (3.12) is introduced to scale the arrive time of direct sound wave to zero. S is the cross-sectional area, $S = wh$. In equation (3.13), \mathcal{G} is an angle for determining the position of image sources, and D_p is the projection of D_0 into the image source plan.

$$D_p = \frac{1}{2} \left[\sqrt{c^2 \left(\frac{z}{c} + t + \Delta t \right)^2 - z^2} + \sqrt{c^2 \left(\frac{z}{c} + t \right)^2 - z^2} \right] \quad (3.14)$$

$$SPL(t)_z = 10 \log \left[N \frac{Kw}{D_0^2} (1 - \alpha)^R \right] - MD_0 \quad (3.15)$$

Kang showed that equation (3.15) is the average of the fluctuation of equation (3.10) and provides the same results. The theory was validated by comparing with an experimental measurement conducted in a corridor where the average absorption coefficient of the boundary surfaces was about 0.1 at 1 kHz. Kang's statistical model agreed reasonably well to within a 10 percent difference with the measurements. Kang also applied his numerical formulation in several underground stations and also found good qualitatively agreements with his experimental measurements.

3.2.3 Analytical prediction model

In current study, the idea of an image source model is made use of to deliver the formulae to predict the steady-state sound pressure levels. Suppose that the long enclosure is infinitely long and has a rectangular cross-sectional area. The width and height of the enclosure is w and h . The origin is assumed to be located at the centre of the source plane, and the locations of source and receiver can represent by $(x_s, 0, z_s)$ and (x_r, y, z_r) . Figure 3.3 shows the schematic diagram of the rectangular coordinate system and the source/receiver geometrical configuration of the assumption. Bases on the concept of the image source model, an infinitely large image plane is created by multi reflections caused by the two vertical walls and two horizontal boundaries. Each

column of image sources are formed by the multi reflections from the two vertical boundaries and rows of each column are created by the multi reflections from the two horizontal walls. See figure 3.4 for the geometrical configuration of the problem. The receiver can now link up to image sources by ray paths and the distance between each image source to receiver can be estimated. It is not difficult to imagine that the distance of each image source is different to each other.

The prime objective of the current study is to estimate the steady-state sound pressure levels for a given geometrical configuration of a rectangular enclosure. Without loss of generality [50], it is sufficient to consider that both source and receiver are located at their geometric centres of the respective planes, i.e. source and receiver are represented by $(0, 0, 0)$ and $(0, y, 0)$ and the horizontal separation is y . At the mean time, all image sources can be replaced by an equivalent area source with the unit strength of $1/wh$ per unit area where w is the width of the enclosure (measured in the x -axis) and h is the height of the enclosure (measured in the z -axis) of the cross-sectional area as shown in figure 3.5. Then, the separation between an equivalent area sources locate at $(x, 0, z)$ and receiver can be obtained from a simple geometrical relationship:

$$D = \sqrt{x^2 + y^2 + z^2} \quad , \quad (3.16)$$

where y is the horizontal separation between the real source and receiver. By using the concept of area source, the mean squared pressure, p_δ^2 , of a small area of image sources (of size δx by δz) located at $(x, 0, z)$ can be estimated by

$$p_\delta^2 = P_0^2 \frac{y^2 e^{m \ln(1-\bar{\alpha}_v) + n \ln(1-\bar{\alpha}_h)}}{D^2} \frac{\delta x \delta z}{wh} \quad , \quad (3.17)$$

where P_0^2 is the free field mean squared pressure at 1 m from the source, $\bar{\alpha}_v$ is the mean absorption coefficients of the vertical walls and $\bar{\alpha}_h$ is the mean absorption coefficients of the horizontal walls. The m and n are the parameters of the number of reflections created by vertical and horizontal walls respectively. They can be approximated by

$$m = |x|/w \quad \text{and} \quad n = |z|/h \quad , \quad (3.18a, b)$$

and the exponential terms are represented by the attenuation due to the reflection from the boundaries and noted as the algebraic identity of,

$$e^{m \ln(1-\bar{\alpha}_v)} = (1-\bar{\alpha}_v)^m \quad \text{and} \quad e^{n \ln(1-\bar{\alpha}_h)} = (1-\bar{\alpha}_h)^n \quad (3.19a, b)$$

with $\ln(1-\bar{\alpha}_v) < 0$ and $\ln(1-\bar{\alpha}_h) < 0$ since $\bar{\alpha}_v$ and $\bar{\alpha}_h$ are less than 1.

To determine the steady-state sound pressure level, it can sum up the contribution from real source and all image sources. Actually, the real source is represented by the image source arrived at the initial time. The mean squared steady-state pressure, p^2 ,

now can be expressed by summing up the sound energy incoherently to give:

$$p^2 = 4 \int_0^\infty \int_0^\infty \frac{P_0^2 y^2}{wh} \frac{e^{-k_1 x - k_2 z}}{x^2 + r_l^2} dx dz \quad (3.20)$$

where k_1 and k_2 is the related absorption coefficient of the vertical and horizontal boundaries and given by

$$k_1 = -\ln(1 - \bar{\alpha}_v) / w, \quad k_2 = -\ln(1 - \bar{\alpha}_h) / h \quad (3.21a, b)$$

and $r_l = \sqrt{y^2 + z^2}$. (3.22)

By applying the equation of an indefinite integral for the exponential integral [86] as follows:

$$\int \frac{e^x}{a^2 + x^2} dx = -\frac{1}{a} \text{Im}\{e^{ia} E_1(-x + ia)\} + \text{const}, \quad (3.23)$$

it can simplify Eq. (3.19) to yield

$$p^2 = \frac{-4P_0^2 y^2}{wh} \int_0^\infty \frac{e^{-k_2 y} \text{Im}\{e^{ik_1 r_l} E_1(ik_1 r_l)\}}{r_l} dz, \quad (3.24)$$

where $E_1(Z)$ is the complex exponential integral of a complex argument Z .

The above integral equation is still difficult but can be further simplified. Referring to the mathematical handbook [86], the exponential integral for complex argument

$e^z E_1(z)$ can be expressed as

$$e^z E_1(z) = \sum_{i=1}^3 \frac{b_i}{a_i + z} + \varepsilon_1 \quad |\varepsilon| < 3 \times 10^{-6} \quad (3.25a)$$

where $a_1 = 0.415775$, $b_1 = 0.711093$ (3.25b)

$$a_2 = 2.29428, \quad b_2 = 0.278518 \quad (3.25c)$$

$$a_3 = 6.2900, \quad b_3 = 0.010389 \quad (3.25d)$$

By following the equation of Eq. (3.25), exponential integral for complex argument

$e^{ik_1 r_1} E_1(ik_1 r_1)$ can be approximated as

$$e^{ik_1 r_1} E_1(ik_1 r_1) = \sum_{i=1}^3 \frac{b_i}{a_i + ik_1 r_1} \quad (3.26)$$

Then, the imagery part of the $e^{ik_1 r_1} E_1(ik_1 r_1)$ can be estimated as

$$\text{Im}\{e^{ik_1 r_1} E_1(ik_1 r_1)\} = \sum_{i=1}^3 \frac{-b_i k_1 r_1}{a_i^2 + k_1^2 r_1^2} \quad (3.27)$$

where a_i and b_i are given by Eq. (3.25b) to Eq. (3.25d). By substituting Eq. (3.27)

into Eq. (3.24), the mean squared steady state pressure is given by

$$p^2 = \frac{4k_1 P_0^2 y^2}{wh} \sum_{i=1}^3 \int_0^\infty \frac{b_i e^{-k_2 y}}{a_i^2 + k_1^2 r_1^2} dz \quad (3.28)$$

The integral in Eq. (3.28) can be evaluated by the indefinite integral shown in Eq.

(3.23) and gives

$$p^2 = \frac{-4P_0^2 y^2}{wh} \sum_{i=1}^3 \frac{b_i}{\sqrt{a_i^2 + k_1^2 y^2}} \text{Im}\{e^{ik_2 \sqrt{a_i^2 / k_1^2 + y^2}} E_1(ik_2 \sqrt{a_i^2 / k_1^2 + y^2})\} \quad (3.29)$$

In normal numerical result presentation, it always compares the steady-state sound pressure level to the source at a distance of 1 m free field condition. So, the relative steady-state sound pressure level (RSPL) due to source is given as,

$$RSPL = 10 \log_{10}(p^2 / P_0^2) \quad (3.30)$$

3.3 Experimental validation

In order to validate the formulation developed in the current study, a theoretical comparison was conducted in two locations to validate the accuracy of the model. Before carrying out the field measurements, the proposed model should be validated by comparing the theoretical prediction of the current model with those predicted results by using the image source method since the current model is developed from the image source method. After that, field measurements were conducted in a model tunnel and in a long pedestrian subway. The relative steady-state sound pressure level (RSPL) shown in figures is a reference to the sound pressure level measured 1 m away from the source in free field condition that is obtained from Eq. (3.30).

3.3.1 Theoretical comparison

An infinite long tunnel with width of 1 m and height of 1 m is used to validate the proposed formulae. Both source and receiver are located at the geometric centres of their respective planes. Figure 3.6 displays the theoretical predictions of mean absorption coefficients of 0.05, 0.1, 0.15 and 0.2. The absorption coefficients of all boundary surfaces are assumed to be the same as in the calculation. For validating the proposed formulae, the numerical predictions of the image source method are also displayed in the figure. In the figure, it can be seen that the prediction results of the

analytical prediction model agree well with the prediction of the image source method except when the receiver is very close to the source and the boundary surface is acoustical hard, i.e. 1 m source/receiver separation and the mean absorption coefficient of all surfaces is 0.05. This tolerance is caused from the error term of Eq. (3.25a). This is the main limitation of using the proposed formulae.

In order to minimise the prediction error of the analytical prediction model, a correction factor is added to Eq. (3.30) to optimise the theoretical prediction of the analytical prediction model. After some calculations, the correction factor (CF) of different combinations of source/receiver separations and mean absorption coefficients is shown in Figure 3.7. The correction factor is developed from comparing the prediction results of the image sound method and the analytical prediction model. Since the correction factor is estimated from the long enclosure with both width and height of 1 m, the separation of source and receiver in real application should be scaled to the size of the correction factor obtained. The related distance shown in figure 3.7 is given as

$$\text{Related Distance} = \text{Source/receiver separation} \div \text{mean of width/height} \quad (3.31)$$

By substituting the correction factor into Eq. (3.30), the related steady state sound

pressure level is given

$$RSPL = CF + 10 \log_{10}(p^2 / P_0^2). \quad (3.32)$$

3.3.2 Indoor model measurements

A 28.5 m long, 1.16 m width and 1.46 m height model tunnel was built for verifying the analytical prediction model. All horizontal and vertical boundary surfaces of the tunnel were fully covered by gypsum board. Part of the gypsum board was used to determine the absorption coefficient. A Brüel & Kjær type 4942 two-microphone impedance measurement tube was used to determine the absorption coefficients of different frequency bands [95]. The gypsum board sample was mounted on one end of the impedance measurement tube. A broadband stationary random signal was generated at the other end of the tube. By using two microphones, the frequency response function H_1 , the frequency response function associated with the incident component H_i and the frequency response function associated with the reflected component H_j can be determined. The complex reflection coefficient R is given by,

$$R = \frac{H_1 - H_i}{H_r - H_1} e^{j2k(1+s)} \quad (3.33)$$

where k is wave number, l is the distance between the first microphone and the front of the sample and s is the spacing between the microphones. The absorption coefficient α it used for predicting in the current study can be calculated by

$$\alpha = 1 - |R|^2 \quad (3.34)$$

The measured absorption coefficients of gypsum board from 125Hz to 6300Hz are listed in Table 3.1.

A Renkus-Heinz PN81 self-powered loudspeaker was used as the sound source and a Brüel & Kjær 4942 pre-polarized diffuse field 1/2-inch condenser microphone, connected to a Brüel & Kjær 2671 preamplifier and a Brüel & Kjær NEXUS condition amplifier was used as the receiver in this measurement. A software-based maximum length sequence system (MLSSA) was installed in a personal computer as an analyser for the experiment [90]. It delivers the predefined pseudorandom signal to the sound source through a special sound card and analyses most of the acoustical parameters such as steady-state sound pressure level, signal to noise ratio and reverberation time from the measured impulse response. Actually, same measuring technique was employed in Chapter 2.3.1.

The sound source was placed at a distance 0.86 m from the left vertical boundary, 0.4 m above ground and receiver was placed at the centreline of the tunnel, 0.8 m above ground, i.e. the x - y - z coordinates of source and receiver were represented by (-0.28, 0, -0.33) and (0, y , 0.07) where y was an interval of 1 m from the source. Figure 3.8

shows the experimental setup in the indoor model. Due to the possible resonance effect of the model tunnel, measured data below 500 Hz are not presented.

Figure 3.9 displays the typical spectra of the steady state sound pressure where the receiver was located at 3 m, 8 m and 20 m from the source. It also shows the numerical predictions of the analytical prediction model and image source method.

During simulations, Sergeev's model [44] is included in the prediction but the difference between experimental results to the theoretical predictions of Sergeev's model is much more than the difference of the image source method and the analytical prediction model. The numerical predictions of Sergeev's model are not included in the figure. In the graph, it can be seen that the theoretical predictions of analytical prediction model agree tolerably well with the experimental results. Furthermore, the theoretical predictions of analytical prediction model agree well with the numerical predictions of the image source method. Similar results were obtained in the other source/receiver separations although those results are not displayed in the figure again.

Figure 3.10 shows the steady-state sound pressure level against source/receiver separation in two different frequencies, 500 Hz and 2 kHz. The steady-state sound pressure level of 500 Hz and 2 kHz are chosen since the acoustic characteristics of 500 Hz and 2 kHz are used to estimate the speech transmission index [2, 3]. The

source and receiver locations are the same as in figure 3.9 except the source/receiver separation. The source/receiver separation was between 1 m to 23 m. It demonstrates that the analytical prediction model can estimate the general trend of measured data. The agreement between the numerical predictions of analytical prediction model and of the image source method is reasonable close. The analytical prediction model can be used to simplify the prediction of the steady state sound pressure level in indoor model measurements.

3.3.3 Outdoor field measurements

Outdoor field measurements were conducted in a pedestrian subway. The pedestrian subway was located under a highway. The subway was 34 m long, 3.64 m wide and 2.4 m high. The vertical walls were finished with plaster. The ceiling and ground were hard concrete. There were two rows of fluorescent tubes installed on two top edges of the subway for illumination. The same set of instruments mentioned in indoor model measurement was used in field measurements again. Both sound source and receiver were located in the centreline of the subway during measurement. The sound source was 1.55 m above ground and receiver was 1.25 m above ground. Since the subway was located under a highway, the background noise level was up to 70 dB at both entrances. In order to maintain the signal level of the measurement 10 dB higher than

the background noise, the experiment was only conducted in the centre part of the subway. Figure 3.11 shows the experimental setup in the subway.

Similar to Chapter 2.3.1, Attenborough's two-parameter model [89] was used to characterise the surface impedances, Z , of the vertical walls and the ground in the current study. By the deduced effective flow resistivity, σ_e and effective rate of change in porosity with depth, α_e , the surface impedance can be calculated by

$$Z = 0.538\sqrt{\sigma_e/f} + i[0.538\sqrt{\sigma_e/f} + 19.74\alpha_e/f], \quad (3.35)$$

where f is the source frequency. The parametric values of σ_e and α_e are deduced from the short-range propagation measurement over the surface (see Figure 3.12). As the covering material of the ground and the ceiling were hard concrete, the surface impedance of the ground and the ceiling are assumed to be the same during prediction. The best-fit parametric values for σ_e and α_e were 8 000 kPa s m⁻² and 50 m⁻¹ for the vertical walls, and 15 000 kPa s m⁻² and 5 m⁻¹ for the hard ground. The one-third octave band absorption coefficients (α) of the boundary surfaces used in the current study are calculated from the measured impedance by [54]

$$\alpha = \frac{|Z-1|^2}{|Z+1|^2}. \quad (3.36)$$

The calculated absorption coefficients of the vertical walls and ground in one-third octave bands are listed in Table 3.1.

Figure 3.13 shows the typical spectra of the steady-state sound pressures when the receiver was located at 6 m, 15 m and 20 m from the source. The numerical predictions of the analytical prediction model and the image source method are also displayed in the figure. The diagram demonstrates that both the numerical predictions of the analytical prediction model and the image source method agree reasonably well with the measurements. Both theoretical models can predict the general trend of the measured acoustical spectrum. The prediction capacity of the analytical prediction model is demonstrated again in the outdoor field measurements.

3.4 Summaries

The image source method is one of the popular approaches to estimating the sound fields in a long enclosure. Discrete image sources in a street canyon are replaced by an effective line source in the previous chapter, and a closed form solution is developed to predict sound fields in a street canyon. The concept of Chapter 2 is further developed in the current study. In the present study, discrete image sources in a long enclosure are replaced by effective area sources, and an analytical formulation has been developed to estimate the steady-state sound pressures. By comparing to the predictions of the image source method, a correction factor has been included in the formulation of the analytical model to improve the prediction accuracy when the

receiver is close to a source. Two experimental measurements were conducted to verify prediction accuracy of the analytical model. It has been demonstrated that the predictions according to the analytical prediction model agreed tolerably well with indoor and outdoor experimental data. It can be seen that the agreement between experimental measurement and prediction is very good [94], the accuracy is generally within 1 to 3 dB in average of each set comparison. The analytical prediction model can be used to simplify the prediction of steady-state sound pressure level in a long enclosure.

Tables

Frequency (Hz)	400	500	630	800	1000	1250	1600
Absorption coefficient of gypsum board (Indoor model)	0.025	0.032	0.034	0.042	0.058	0.08	0.126
Absorption coefficient of vertical wall (Field measurements)	0.053	0.059	0.066	0.075	0.083	0.1	0.14
Absorption coefficient of hard ground (Field measurements)	0.04	0.045	0.05	0.056	0.063	0.07	0.079
Frequency (Hz)	2000	2500	3150	4000	5000	6300	8000
Absorption coefficient of gypsum board (Indoor model)	0.114	0.116	0.128	0.156	0.161	0.207	
Absorption coefficient of vertical wall (Field measurements)	0.12	0.13	0.14	0.16	0.18	0.2	0.22
Absorption coefficient of hard ground (Field measurements)	0.087	0.098	0.11	0.12	0.14	0.15	0.17

Table 3.1: The estimated mean absorption coefficients of the boundary surfaces in the indoor model and the pedestrian subway.

Figures

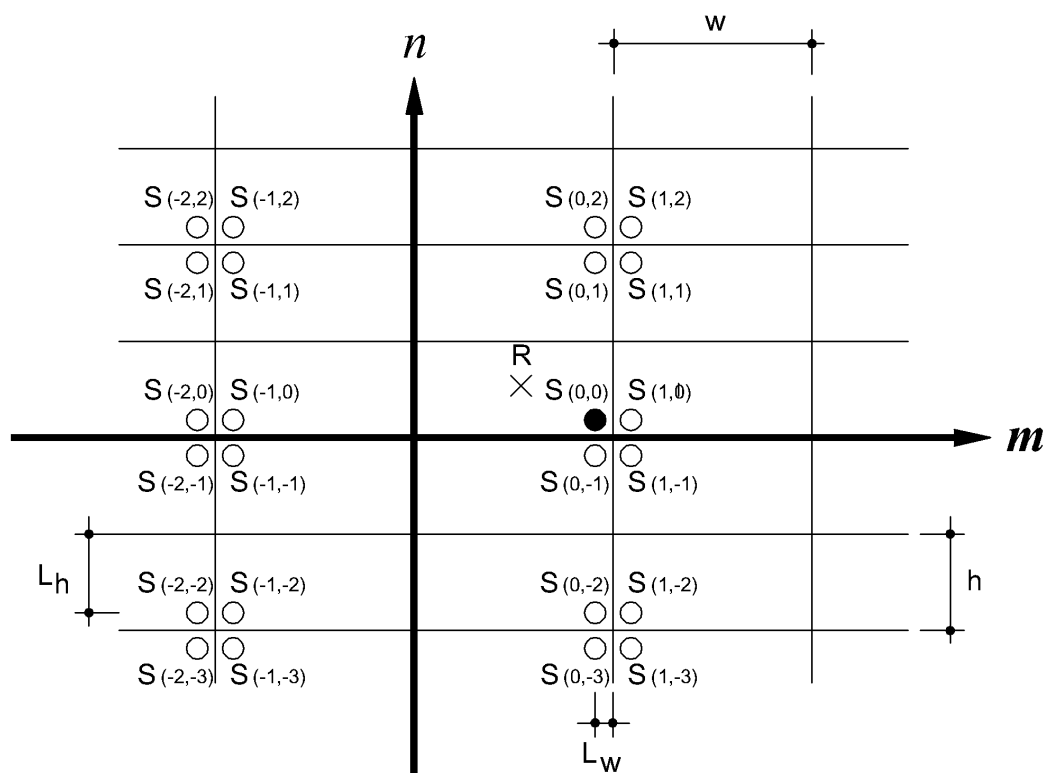


Fig. 3.1: Schematic diagram to show the relative locations of the receiver, the point source (solid circle) and image sources (open circle) of Kang's image source model in 2-D view.

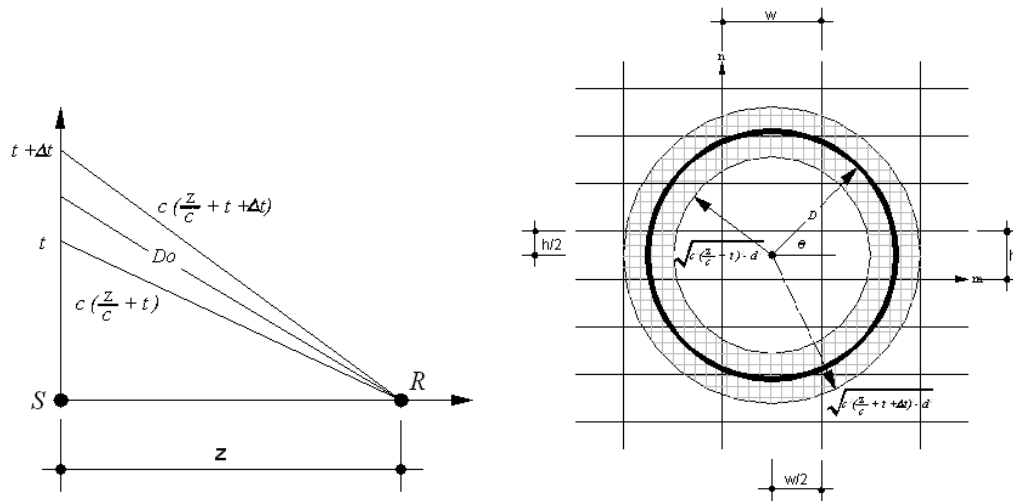


Fig. 3.2: Schematic diagram shows the calculation of D_o , N and R between time t and $t + \Delta t$ of Kang's statistical image source method.

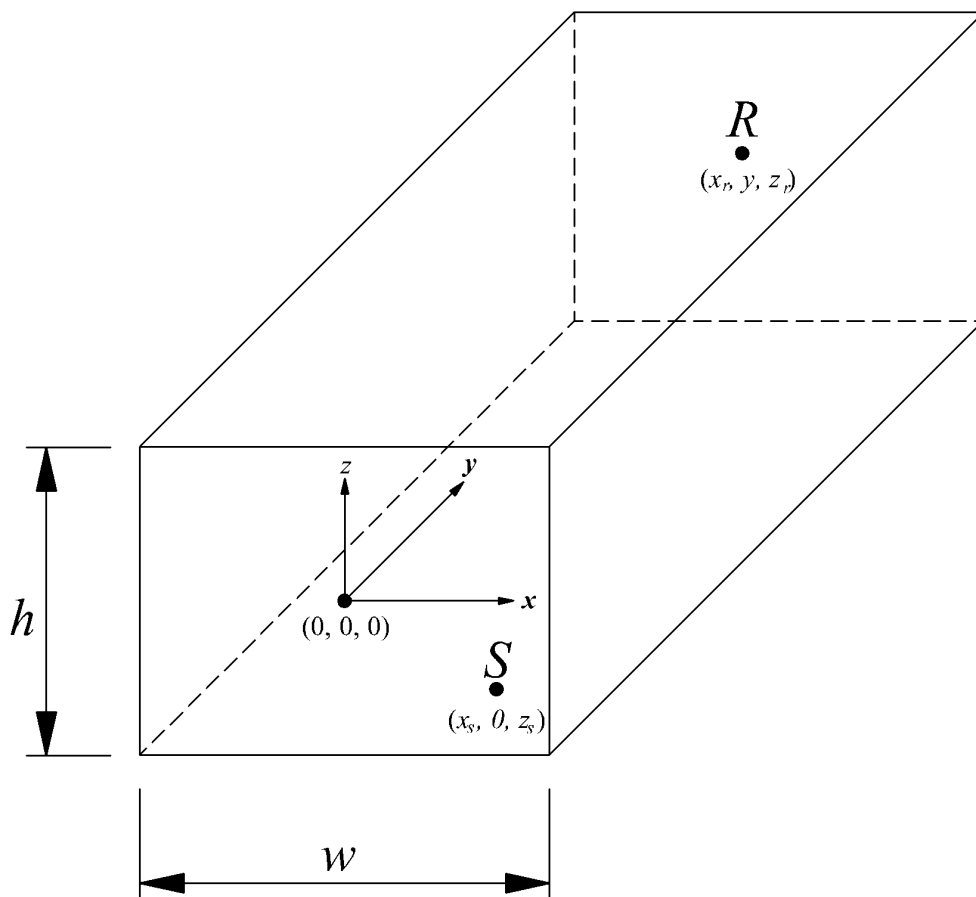


Fig. 3.3: Schematic diagram showing the rectangular coordinate system and the geometrical configuration of a long enclosure with source and receiver locations.

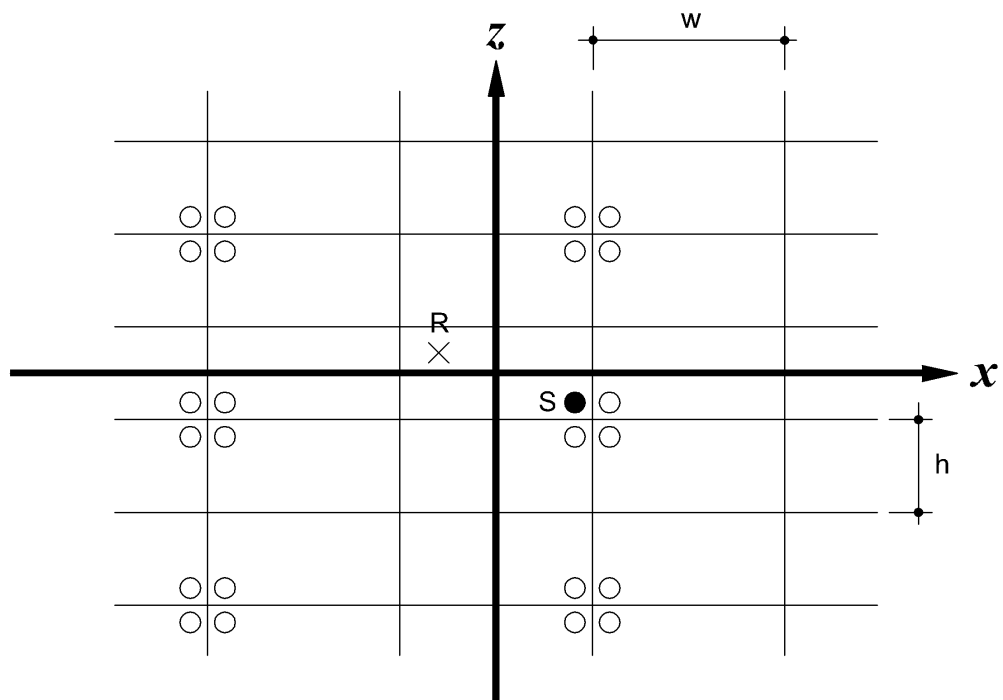


Fig. 3.4: Schematic diagram of the relative locations of the receiver, the point source (solid circle) and image sources (open circle) of the image source method in 2-D view.

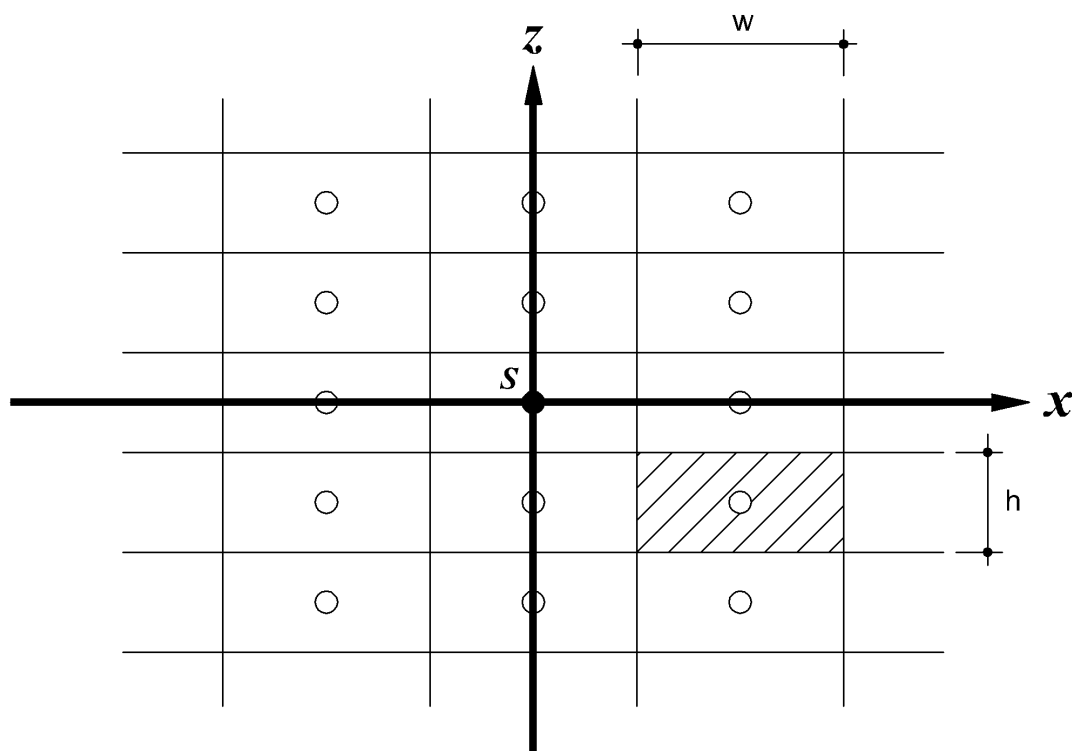


Fig. 3.5: Schematic diagram of the source plane and an equivalent area source of the analytical prediction model. The solid circle is the point source and open circles are the image sources caused from the multi reflections of two vertical walls and two horizontal boundaries. The field strength of the equivalent area source (in shadow) is the same as the correlated image source.

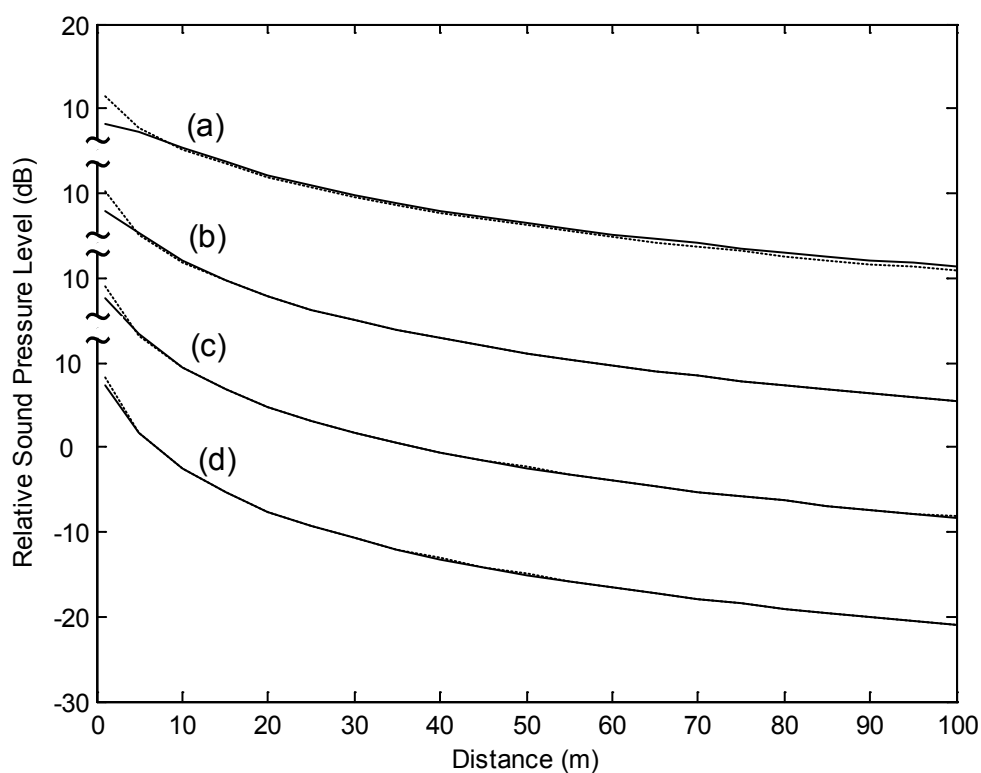


Fig. 3.6: The relative sound pressure level is plotted versus distance in a long enclosure with the width and height both of 1 m. The source and receiver are placed, respectively, at the centre of the cross section of the source plane and receiver plane. The absorption coefficients of all boundary surfaces are the same at (a) 0.05, (b) 0.1, (c) 0.15, and (d) 0.2. The solid lines (—) are the predictions by the analytical prediction model and the dotted lines (····) are the predictions by the image source method.

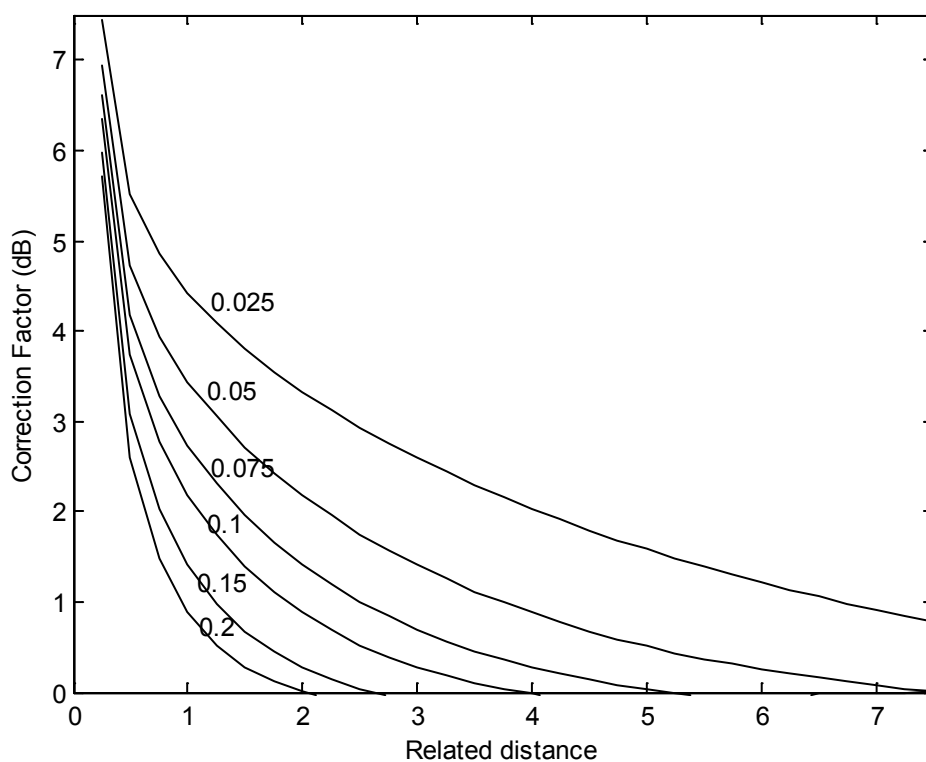


Fig. 3.7: Correction factor of the analytical prediction model. The correction factor is obtained from the absorption coefficient and the related distance. The related distance is estimated by dividing the source/receiver separation by the mean of width and height of the long enclosure.



Fig. 3.8: Photograph showing the experiment setup of the indoor model measurements.

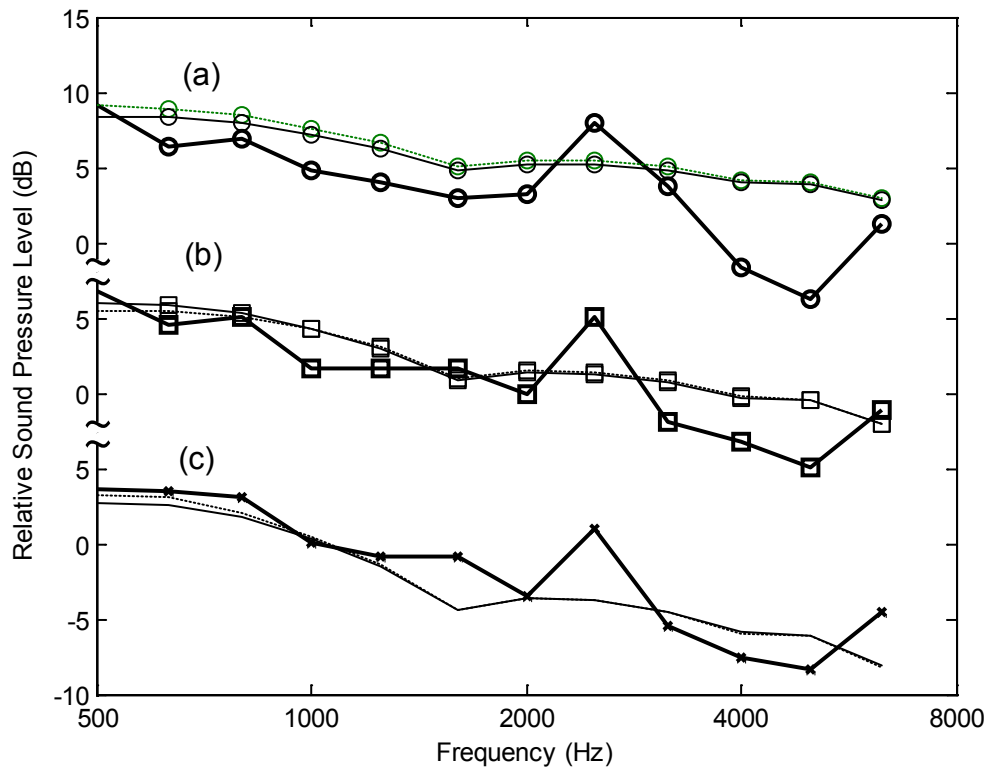


Fig. 3.9: The relative sound pressure level is plotted versus the source frequency where the source was located at 0.86 m from the left vertical boundary and at 0.4 m above ground. The receiver was placed at the centreline of the tunnel and 0.8 m above ground. The thick solid lines are experimental data, the thin solid lines are predictions by the analytical prediction model and the dotted lines are the predictions by the image source method. The source/receiver separations were 3 m in (a), 8 m in (b) and 20 m in (c).

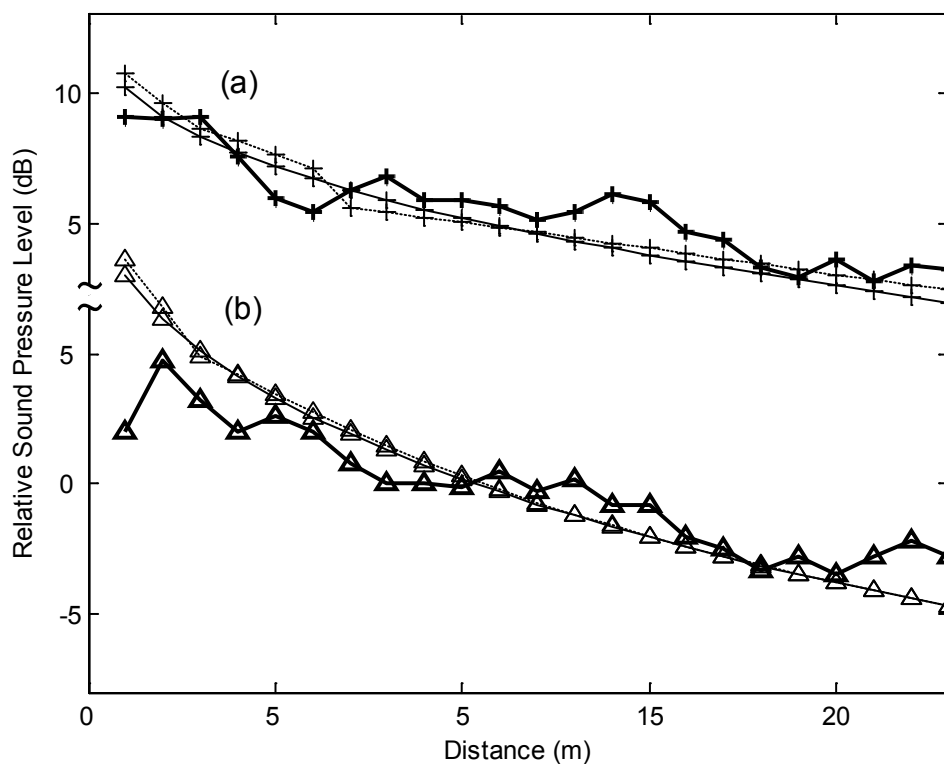


Fig. 3.10: The relative sound pressure level is plotted versus the horizontal separation.

The source location, receiver locations and the keys for the lines shown in the figure are the same as figure 3.9 except for the source/receiver separation. The source frequencies were 500 Hz in (a) and 2 kHz in (b).



Fig. 3.11: Photograph displaying the experiment setup of the outdoor field measurements. The foreground is the sound source, PN 81 self-powered loudspeaker. The receiver is located in the centre of the photograph.

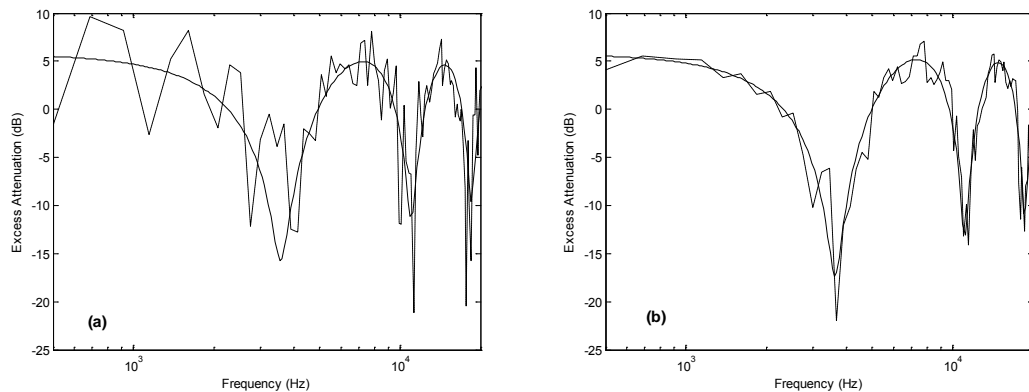


Fig. 3.12: Plot of excess attenuation against frequency for the characterisation of (a) the vertical walls and (b) the hard floor of the pedestrian subway. The solid lines (—) are theoretical predictions by the two-parameter model. The dotted lines (-----) are experimental data.

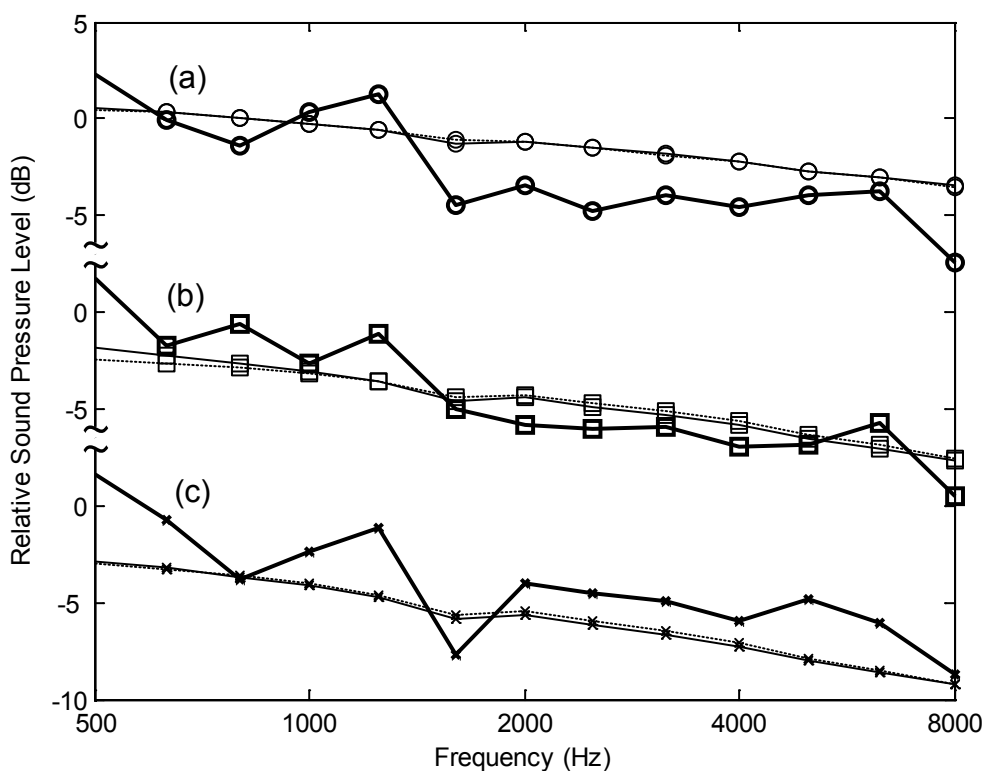


Fig. 3.13: Comparison of measured and predicted relative sound pressure levels in the outdoor field measurements. Both numerical predictions of the image sound method and the analytical prediction model are displayed in the figure. The source was located at the centreline of the subway, 1.55 m above ground. The receiver was placed at centreline of the subway and 1.25 m above ground. The source/receiver separations were 6 m in (a), 15 m in (b) and 20 m in (c). The keys for the lines show in the figure are the same as figure 3.9.

Chapter 4

Transmission of noise through a junction in a street canyon

4.1 Introduction

Community noise has been recognized as a major problem in urbanised high-rise city.

The noise sources include transportation, industry and other sources. Studies show that transportation is the greatest contributor to the community noise [96 - 98]. In order to investigate the characteristics of transportation noise in the urban area, theoretical studies were conducted and most of them were focused on the noise propagation in straight street canyons [29, 34, 38, 42, 51, 56, 99, 100].

Apart from the straight street canyon, cross junction is the other importance facility of a city. Actually, a city is a combination of building façades, street canyons, cross junctions and flat land such as squares and parks. The building façade is assumed to be an obstacle which sound waves can not pass through, although sound waves travelling in a city should pass through street canyons, cross junctions of streets and

flat lands to reach a receiver. Most previous studies focused on predicting the propagation loss in an open area and in straight street canyons. There are fewer studies of sound field propagation through a junction in a street canyon although this is a useful study area. Besides the study for street junctions, there are limited related studies in long enclosures. So *et al.* [39, 40], using a coherent image source model to predict the sound field in a long enclosure with a T-intersection and U-turn long enclosures, being one of the limited cases. However, they do not provide the detail prediction formula. The aims of this study are, first, the development a systematic formulation to obtain the sound field when, (1) the source and receiver maintain a sight-line contact, and (2) the source cannot ‘see’ the receiver directly in the cross-junction of a street canyon; and second, display the sound field characteristics of the after junction regions by comparing the sound field of a straight street canyon. Since So [39, 40] used a coherent image source method to predict the source field in “T” and “U” sharp long enclosures successfully, the same method can be applied in the current study. Both coherent and incoherent image source methods are employed in the study to develop the systematic formations. The systematic formations are validated by comparing the predictions with full scale outdoor experimental results. As shown by comparison, the systematic formation by using coherent method provides better accuracy than the incoherent method but the incoherent method still

can predict the general trend of the measurements. The sound field attenuation characteristics of the after cross junction region is study afterwards by the incoherent method. A short summary will be given at the end of the chapter.

4.2 Theory

4.2.1 Formulation of the problem

Consider two streets which cross perpendicularly at a junction in an urban setting where both sides of the streets are surrounded by tall buildings. The respective widths of the two streets are W and B . Hence, the cross-sectional area of the junction is W by B . A sound source S_1 is placed at height z_s above the ground and a horizontal distance of x_s from the left vertical walls of the first street. A three-dimensional rectangular co-ordinate system, x - y - z , is chosen such that the x - z plane coincides with that of the source. The x -direction is measured from the left walls of the first canyon street where $0 \leq x_s \leq W$. The y -direction is measured along the first street from the source. The z -direction is measured positively upwards where $z_s \geq 0$. Suppose that the source is placed at a horizontal distance Y_L from the junction along the y -axis. Figure 4.1 shows the schematic diagram of the problem at hand where the receiver is situated at a horizontal distance Y_T from the opposite junction along the y -axis.

The problem is how to estimate the transmission of noise through the cross junctions where tall buildings are aligned along the streets. The source \mathbf{S}_1 is located at $(x_s, 0, z_s)$.

The receiver \mathbf{R}_1 has a co-ordinate of (x_r, y_r, z_r) where $y_r = Y_L + Y_T + B$. It is either situated

- (i) at the opposite end of the first street across the junction, i.e. $x_r \leq W, Y_T \geq 0$ and $z_r \geq 0$,
- (ii) along the second street round the corner of the junction where $-B \leq Y_T \leq 0$.

Because the sound fields are asymmetric in case (ii), we only need to consider the situation where the receiver is situated at the left side of the second street canyon, i.e. $x_r \leq 0$ and $z_r \geq 0$. If the sound field at the right side of the second street canyon (i.e. $W \leq x_r$) is needed, we can simply change the source location to $(W - x_s, 0, z_s)$ and the receiver location to $(W - x_r, y_r, z_r)$.

To simplify the numerical analysis, the street canyons may be modelled by two infinitely high vertical planes erected parallel to each other on an impedance ground [34, 42]. The sound diffracted at the top edges of the buildings can generally be ignored because the sound field is dominated by the direct and reflected waves in this urban environment.

In earlier studies, Oldham [56] and Li [51] used an image source method for prediction of the sound field in a street canyon with no intersections. Figure 4.2 shows a schematic diagram of the relative locations of images sources and the receiver. The façades and their images, ..., L_{-3} , L_{-2} , L_{-1} , L_1 , L_2 , L_3 , ... are also shown in Figure 4.2.

With these façade surfaces, the image sources can be constructed as follows. An image source S_{-1} is created because of the reflection of the source S_1 on the façade surface L_{-1} . The image sources S_2 and S_3 are then formed because of the reflection of the sound source S_1 and the image source S_{-1} on the façade surface L_1 . Next, the image sources S_{-2} and S_{-3} are created on reflection from L_{-1} due to the image sources S_2 and S_3 . These image sources are referred to as noise sources in the following paragraphs.

Based on the sound source S_1 , this process repeats to create a series of image sources S_2 , S_3 , ... located at the right side of L_1 . The image source S_2 creates a sound ray that hits the façade L_1 before it reaches the receiver. The source S_3 is formed for a sound ray that hits the façade L_1 and then the façade L_{-1} before the sound ray reaches the receiver. The procedure continues for determining the ray paths traced by other sources, S_3 , S_4 , and so on. Similarly, the ray paths for S_{-1} , S_{-2} , S_{-3} etc. can also be constructed. There is an analogous series of image sources ... \bar{S}_{-3} , \bar{S}_{-2} , \bar{S}_{-1} , \bar{S}_1 , \bar{S}_2 , \bar{S}_3 ... that can also be identified because of the presence of a reflecting ground. The

sound rays of these image sources hit the ground once before they reach the receiver.

The locations of these sound sources, $\mathbf{S}_{\pm m} = (x_{\pm m}, 0, z_s)$ and $\bar{\mathbf{S}}_{\pm m} = (x_{\pm m}, 0, -z_s)$, can be determined from the geometrical configuration of the problem, where the x -coordinates of these image sources are given by

$$x_{\pm m} = mW \mp W_{(m)} \quad \text{for } m = 1, 2, 3, \dots, \quad (4.1a)$$

where

$$W_{(m)} = \begin{cases} W - x_s & \text{if } m \text{ is odd} \\ x_s & \text{if } m \text{ is even} \end{cases} . \quad (4.1b)$$

Figure 4.2 shows the ray paths connecting the image sources \mathbf{S}_2 and $\bar{\mathbf{S}}_2$ with the receiver.

Here, the image source theory is extended to include the case where the street canyon has a junction in the present study. By a geometrical consideration, the distance between a source \mathbf{S} at (S_x, S_y, S_z) and a receiver \mathbf{R} at (R_x, R_y, R_z) is given by

$$D(\mathbf{S} | \mathbf{R}) \equiv D(S_x, S_y, S_z | R_x, R_y, R_z) = \sqrt{(S_x - R_x)^2 + (S_y - R_y)^2 + (S_z - R_z)^2} . \quad (4.2)$$

If the image source and receiver are placed near an impedance plane with the specific normalised admittance of β , then the reflected sound field $P_\beta(\mathbf{S} | \mathbf{R}, \beta)$ can be computed by

$$P_{\beta}(S | R, \beta) = \frac{Q(S | R, \beta) e^{ikD}}{4\pi D} \quad (4.3)$$

where $k(\equiv \omega/c)$ is the wave number, ω is the angular frequency of the source, c is the speed of sound in air and $Q(S | R, \beta)$ is the spherical wave reflection coefficient determined according to [89]

$$Q \equiv Q(S | R, \beta) = R_p + (1 - R_p) F(w) \quad . \quad (4.4)$$

In the above equation, the plane wave reflection coefficient R_p is given by

$$R_p = \frac{\cos \theta - \beta}{\cos \theta + \beta} \quad (4.5)$$

where θ is the incident angle of the reflected wave measured from the normal of impedance plane. The boundary loss factor $F(w)$ is determined by

$$F(w) = 1 + i\sqrt{\pi} w e^{-w^2} \operatorname{erfc}(-iw) \quad , \quad (4.6)$$

where w , which is known as the numerical distance, is defined by

$$w = \sqrt{kD/2} (1+i)(\cos \theta + \beta) \quad . \quad (4.7)$$

Suppose that the source and receiver are placed between two parallel façade surfaces which have the respective specific normalised admittance of β_- and β_+ . The spherical wave reflection coefficients due to the image source S and the receiver R can be written as $Q_- \equiv Q(S | R, \beta_-)$ and $Q_+ \equiv Q(S | R, \beta_+)$ for the left and right façade surfaces respectively. For a sound ray emanating from S , multiple reflections occur between the parallel surfaces before it reaches the receiver R . A combined complex wave reflection factor is needed in favour of $Q_- \equiv Q(S | R, \beta_-)$ or $Q_+ \equiv Q(S | R, \beta_+)$ in Eq. (4.3).

The combined reflection factors due to the j^{th} source S_j can be determined by counting the number of reflections from each of these boundary surfaces and multiplying their respective spherical wave reflection coefficients together. It follows immediately that

$$\Gamma(S_j | \mathbf{R}, j, Q_+, Q_-) = \begin{cases} Q_+^{\lceil j+g(j) \rceil / 2} Q_-^{\lceil j-g(j) \rceil / 2} & \text{if } j < 0 \\ Q_+^{\lfloor j-g(j) \rfloor / 2} Q_-^{\lfloor j+g(j)-2 \rfloor / 2} & \text{if } j > 0 \end{cases}, \quad (4.8)$$

where $\text{sgn}(x)$ is a sign function defined as

$$\text{sgn}(x) = \begin{cases} -1 & \text{if } x < 0 \\ 1 & \text{if } x > 0 \end{cases} \quad (4.9)$$

and the functions $g(x)$ is given by

$$g(x) = \begin{cases} 1 & \text{if } x \text{ is an odd integer} \\ 0 & \text{if } x \text{ is an even integer} \end{cases}. \quad (4.10)$$

4.2.2 Transmission of noise through a cross junction

Using the concept of the combined wave reflection factors, the total sound field due to a monopole source of unit strength can now be calculated by summing all contributions coherently. In the presence of a cross junction in a street canyon, the sound field is given by

$$P(\omega) = \frac{1}{4\pi} \sum_m \left[V_m \Gamma_m \frac{e^{ikD_m}}{D_m} + \bar{V}_m \bar{\Gamma}_m \frac{e^{ik\bar{D}_m}}{\bar{D}_m} \right], \quad (4.11)$$

where $D_m = D(S_m | \mathbf{R}_I)$ and $\bar{D}_m = D(\bar{S}_m | \mathbf{R}_I)$ are the respective distances from the receiver \mathbf{R}_I to the sources S_m and \bar{S}_m . The reflection factor Γ_m is defined as

$$\Gamma_m \equiv \Gamma(S_m | \mathbf{R}_I, m, Q_A, Q_B) \quad (4.12)$$

for the source and receiver placed between the left façade surface L_I and the right façade surface L_J . These two surfaces have the respective specific normalised admittance of β_A and β_B and their spherical wave reflection coefficients are $Q_A \equiv Q(S_m | \mathbf{R}_I, \beta_A)$ and $Q_B \equiv Q(S_m | \mathbf{R}_I, \beta_B)$ respectively, cf Eq. (4.4). The parameter V_m is the visibility factor which is set to 1 when a direct link can be established between the receiver and the image source S_m . Otherwise it is set to zero.

The overbar in R_m , Γ_m and V_m which appears in the second term of the square bracket of Eq. (4.11) represents the respective parameters for the images sources \bar{S}_m which are located below the ground surface. Their combined spherical wave factors are obtained by

$$\bar{\Gamma}_m = Q_G \Gamma(\bar{S}_m | \mathbf{R}_I, m, Q_A, Q_B) \quad , \quad (4.13)$$

where $Q_G \equiv Q(\bar{S}_m | \mathbf{R}_I, \beta_G)$ is the spherical wave reflection coefficient of the ground surface which have the specific normalised admittance of β_G . Again, the visibility factor \bar{V}_m is set to 1 when the image source \bar{S}_m can link with the receiver and it is set to 0 for other cases.

For a street canyon with no junction, all images sources S_m and \bar{S}_m can link with the receiver. As a result, all visibility factors (V_m and \bar{V}_m) are set to 1 for all m . On

the other hand, some visibility factors are zero if the source and receiver are located at the opposite sides of the junction as shown in Figure 4.1. A systematic method has been developed to determine the visibility factors as follows.

Figure 4.3 shows a cross-sectional view where the horizontal branches of the junction are not shown for clarity. However, the left façade surface L_{-1} , the right façade surface L_1 and the image façade surfaces ($\dots, L_{-3}, L_{-2}, L_2, L_3, \dots$) are shown instead. A gap in each of the façade surfaces represents an opening in each of the image façades. If a sound ray interacts with one of these gaps, the visibility factor will be zero because the sound ray will not be able to reflect back to the main branch of the street canyon where the receiver resides. These gaps can be treated essentially as anechoic surfaces with perfect absorption.

To determine whether a sight-line contact has been established, the situation when the receiver and the source have the same height above the ground in the street canyon should be considered initially. In the x - y plane, the coordinates of the upper and lower edges (marked as $A_j^{(u)}$ and $A_j^{(d)}$ in Figure 4.3) of the anechoic surfaces are determined as $([j + H(-j)]W, Y_L + B)$ and $([j + H(-j)]W, Y_L)$ where $j = \pm 1, \pm 2, \pm 3, \dots$ and $H(Z)$ is the Heaviside step function given by

$$H(Z) = \begin{cases} 0 & \text{if } Z < 0 \\ 1 & \text{if } Z > 0 \end{cases} . \quad (4.14)$$

Then, the equations, $\Lambda_u^{(j)}$ and $\Lambda_d^{(j)}$ can be determined, for the respective sight lines of the sound rays which start from the receiver and pass through the upper and lower edges of the gaps as follows:

$$\Lambda_j^{(u)} : x = y / \tan \theta_j^{(u)} + X_j^{(u)} \quad (4.15a)$$

and

$$\Lambda_j^{(d)} : x = y / \tan \theta_j^{(d)} + X_j^{(d)} \quad (4.15b)$$

where the angles $\theta_j^{(u)}$ and $\theta_j^{(d)}$ are the respective angles between sight-lines $\Lambda_j^{(u)}$ and $\Lambda_j^{(d)}$ with the y -axis. All sight-line angles vary between 0 and π . The respective slopes of the sight lines are given by:

$$\tan \theta_j^{(u)} = \frac{Y_T}{x_r - [j + H(-j)]W} , \quad (4.16a)$$

and

$$\tan \theta_j^{(d)} = \frac{Y_T + B}{x_r - [j + H(-j)]W} , \quad (4.16b)$$

where $\pi/2 \geq \theta_j^{(d)} > \theta_j^{(u)} \geq 0$ when $j < 0$ and $\pi/2 \leq \theta_j^{(d)} < \theta_j^{(u)} \leq \pi$ when $j > 0$. The

x -intercepts of the sight-lines, $X_j^{(u)}$ and $X_j^{(d)}$, are given by

$$X_j^{(u)} = \frac{[j + H(-j)]y_r W - (Y_L + B)x_r}{Y_T} , \quad (4.17a)$$

and

$$X_j^{(d)} = \frac{[j + H(-j)]y_r W - Y_L x_r}{B + Y_T} . \quad (4.17b)$$

In the above equations, the equations for the sight lines $\Lambda_j^{(u)}$ and $\Lambda_j^{(d)}$ are derived for the case when the source and receiver have the same height. It can be shown that the same equations are also applicable when the source and receiver are located at different heights. In a three-dimensional system, Eqs. (4.15a) and (4.15b) represent planar surfaces where the respective sight lines reside. As a result, we can use them to determine the visibility factors for the sound rays used in Eq. (4.11).

If an image source is bounded between $\Lambda_j^{(u)}$ and $\Lambda_j^{(d)}$, the sound ray radiated from the image source will hit the anechoic surfaces. In other words, no sound energy can reach the receiver which is located at the main branch of the street canyon. As a result, the visibility factors in Eqs. (4.11) can be set to zero. Since $\Lambda_j^{(u)}$ and $\Lambda_j^{(d)}$ are independent of the receiver and source heights, the visibility factor for the source located above the ground is the same for sources situated below the ground, i.e. $V_j = \bar{V}_j$ for all j . Therefore, it is sufficient just to determine the visibility factor, V_j .

To facilitate the analysis, the x -intercepts $X_j^{(u)}$ and $X_j^{(d)}$ with the x -co-ordinates of the sources should be compared. It can be seen immediately that sound rays will be transmitted to the main branch of the first street canyon when $X_{\pm j \pm 1}^{(d)} \leq x_m \leq X_{\pm j}^{(u)}$ but they will turn into the second street canyon when $X_{\pm j}^{(u)} \leq x_m \leq X_{\pm j}^{(d)}$. Hence, the

visibility factors can be expressed as

$$V_m = \begin{cases} 1 & \text{if } x_m \in \dots [X_{-3}^{(d)}, X_{-2}^{(u)}], [X_{-2}^{(d)}, X_{-1}^{(u)}], [X_{-1}^{(d)}, X_1^{(d)}], [X_1^{(u)}, X_2^{(d)}], [X_2^{(u)}, X_3^{(d)}], \dots \\ 0 & \text{if } x_m \in \dots [X_{-3}^{(u)}, X_{-3}^{(d)}], [X_{-2}^{(u)}, X_{-2}^{(d)}], [X_{-1}^{(u)}, X_{-1}^{(d)}], [X_1^{(d)}, X_1^{(u)}], [X_2^{(d)}, X_2^{(u)}], \dots \end{cases} \quad - (4.18)$$

where m is set at $\pm 1, \pm 2, \pm 3, \dots$ in turn to check whether the image source S_m is

bounded by any of pair of sight-line planes $\Lambda_j^{(u)}$ and $\Lambda_j^{(d)}$.

A close examination of Eq. (4.18) suggests that only a finite number of image sources have non-zero visibility factors. To demonstrate this point, the slopes of the sight-line planes, $\Lambda_j^{(u)}$ and $\Lambda_j^{(d)}$, for $j > 0$ can be considered. By considering Eqs. (4.16a) and (16b), it can show that $\theta_j^{(d)}$ is always less than $\theta_j^{(u)}$. Hence, $X_j^{(u)} > X_j^{(d)}$ and the regions $[X_j^{(d)}, X_j^{(u)}]$ are always present.

On the other hand, Eqs. (4.17a) and (4.17b) suggest that the condition of $X_j^{(u)} > X_{j+1}^{(d)}$

is valid when $j < J_+$ where

$$J_+ = \frac{Y_r W + B x_r}{B W} \quad . \quad (4.19)$$

For $j < 0$, the condition for $X_{j-1}^{(d)} > X_j^{(u)}$ is valid when $j > J_-$ where

$$J_- = -\frac{Y_r W + B(W - x_r)}{B W} \quad . \quad (4.20)$$

As a result, the series in Eq. (4.18) for $V_m = 1$ can be determined with the following condition:

$$J_- < j < J_+ . \quad (4.21)$$

Setting $j = J_+$ in Eq. (4.17a) and $j = J_-$ in Eq. (4.17b), $X_{J_+}^{(u)}$ and $X_{J_-}^{(d)}$ can be obtained respectively. They can then be used to calculate the number of image sources used in Eq. (4.11). To illustrate this point, a normalised bar chart of $X_{j+1}^{(d)}$, $X_j^{(u)}$ and $X_j^{(d)}$ for different positive values of j is shown in Fig. 4.4 where a typical geometrical configuration of the source and receiver is used.

4.2.3 The sound field round a corner of a cross junction

The next task is to determine the sound field for a receiver that lies in the second street round the corner. It is convenient to introduce image receivers to account for the multiple reflections between the façade surfaces M_1 and M_{-1} in the second street canyon. The image receivers are generated in an analogous manner as with that for the image receivers. Figure 4.5 shows a schematic diagram for these image receivers which are denoted by $\mathbf{R}_1, \mathbf{R}_2, \mathbf{R}_3 \dots$ located above the ground. The coordinates of these image receivers are $\mathbf{R}_{\pm n} = (x_r, y_{\pm n}, z_r)$ where

$$y_{\pm j} = Y_L + jB \mp B_{(j)} \quad \text{for } j = 1, 2, 3, \dots , \quad (4.22a)$$

where

$$B_{(j)} = \begin{cases} B - (y_r - Y_L) & \text{if } j \text{ is odd} \\ y_r - Y_L & \text{if } j \text{ is even} \end{cases} . \quad (4.22b)$$

Suppose that the receiver is located at the left branch of the street canyon, i.e. $x_r < 0$. A

close examination of the ray tracing diagram suggests that the image sources at the right side of the first street canyon (i.e. S_{+m} and \bar{S}_{+m}) can only contribute to the total sound field. On the other hand, the image sources at the left side of the first street canyon (S_{-m} and \bar{S}_{-m}) cannot contribute to the total sound field because direct linkage between the image sources and image receivers cannot be established.

In this case, linking the image sources with image receivers allows the determination of all possible ray paths for the calculation of the total sound field. It is then straightforward to show that the pressure field is given by

$$P(\omega) = \frac{1}{4\pi} \sum_{n=1}^{\infty} \sum_{m=1}^{\infty} \left[V_{m,n} \Gamma_{m,n} \frac{e^{ikD_{m,n}}}{D_{m,n}} + \bar{V}_{m,n} \bar{\Gamma}_{m,n} \frac{e^{ik\bar{D}_{m,n}}}{\bar{D}_{m,n}} \right] , \quad (4.23)$$

where the source/receiver separations are now denoted by $D_{m,n} = D(S_m | R_n)$ and $\bar{D}_{m,n} = D(\bar{S}_m | R_n)$. The visibility factors are represented by $V_{m,n}$ and $\bar{V}_{m,n}$ but, as discussed in Sec. 4.2.2, these two visibility factors are identical.

In addition, the reflection factor $\Gamma_{m,n}$ is determined by multiplying the corresponding complex wave reflection coefficients for each interaction with L_{-1} , L_1 , M_{-1} and M_1 . It can be shown that

$$\Gamma_{m,n} = \Gamma(S_m | R_n, m, Q_A, Q_B) \times \Gamma(S_m | R_n, n, Q_C, Q_D) , \quad (4.24a)$$

and

$$\bar{\Gamma}_{m,n} = Q_G \times \Gamma(\bar{S}_m | \mathbf{R}_n, m, Q_A, Q_B) \times \Gamma(\bar{S}_m | \mathbf{R}_n, n, Q_C, Q_D) \quad , \quad (4.24b)$$

where $Q_C \equiv Q(\mathbf{R}_n | S_m, \beta_C)$ is the spherical wave reflection coefficient with β_C as the specific normalised admittance for the façade surfaces M_{-1} . Similarly, $Q_D \equiv Q(\mathbf{R}_n | S_m, \beta_D)$ and β_D are the spherical wave reflection coefficient and the specific normalised admittance for the façade surfaces M_1 respectively.

Based on earlier analysis, the visibility factor can be established by determining the sight-line planes. In the present situation, x_r is located at the left side of the second street canyon (i.e. $x_r < 0$) and y_r is replaced by the image receiver y_n . The image receiver is calculated by Eq. (4.22a) with n restricted to positive integers only. Hence, the sight-line planes are modified from Eqs. (4.15a) and (4.15b) to

$$\Psi_n^{(u)} : x = y / \tan \phi_n^{(u)} + \Upsilon_n^{(u)} \quad (4.25a)$$

and

$$\Psi_n^{(d)} : x = y / \tan \phi_n^{(d)} + \Upsilon_n^{(d)} \quad (4.25b)$$

where the sight-line angles $\phi_n^{(u)}$ and $\phi_n^{(d)}$ are expressed in term of the slope by:

$$\tan \phi_n^{(u)} = \frac{y_n - (Y_L + B)}{x_r} \quad , \quad (4.26a)$$

and

$$\tan \phi_n^{(d)} = \frac{y_n - Y_L}{x_r} \quad . \quad (4.26b)$$

All sight-line angles vary between $\pi/2$ and π except $\phi_1^{(u)}$ where it is bounded

between 0 and $\pi/2$.

The respective x -intercepts, $\Upsilon_n^{(u)}$ and $\Upsilon_n^{(d)}$, can be determined by

$$\gamma_n^{(u)} = \frac{-(Y_L + B)x_r}{y_n - (Y_L + B)} \quad , \quad (4.27a)$$

and

$$\gamma_n^{(d)} = \frac{-Y_L x_r}{y_n - Y_L} \quad . \quad (4.27b)$$

If a sound ray is bounded by the sight-lines, $\Psi_n^{(u)}$ and $\Psi_n^{(d)}$, it will be transmitted through the opening of the second street canyon. On the other hand, some sound rays pass through the opening of the first street canyon. This condition can be determined by introducing the sight line plane joining the receiver to the lower edge of the opening of the façade surface L_l . Suppose that this sight line is denoted by $\Psi_n^{(h)}$

which can be determined by

$$\Psi_n^{(h)} : x = y / \tan \phi_n^{(h)} + \Upsilon_n^{(h)} \quad (4.28a)$$

where the slope and x -intercept are given, respectively, as

$$\tan \phi_n^{(h)} = \frac{y_n - Y_L}{x_r - W} \quad (4.28b)$$

and

$$\gamma_n^{(h)} = \frac{y_n W - Y_L x_r}{y_n - Y_L} \quad . \quad (4.28c)$$

By a simple geometrical construction of the ray path, it can be seen that sound rays are

bounded by $\Psi_1^{(d)}$ and $\Psi_1^{(h)}$ if $\phi_n^{(h)}$ is greater than $\phi_n^{(d)}$. On the other hand, the sound rays are bounded by $\Psi_1^{(u)}$ and $\Psi_1^{(d)}$ if $\phi_n^{(h)}$ is less than $\phi_n^{(d)}$.

Since the study is interested in the possibility of a sound ray reaching the second street canyon, the visibility factors can then be adapted from Eq. (4.15) to yield

$$V_{m,n} = \bar{V}_{m,n} = \begin{cases} 1 & \text{if } \Upsilon_+(n) > x_m > \Upsilon_-(n) \\ 0 & \text{otherwise} \end{cases}, \quad (4.29)$$

where $\Upsilon_+(n)$ and $\Upsilon_-(n)$ are defined as follows:

$$\Upsilon_+(n) = \begin{cases} \Upsilon_n^{(h)} & \text{if } \phi_n^{(u)} > \phi_n^{(h)} \\ \Upsilon_n^{(u)} & \text{otherwise} \end{cases}, \quad (4.30a)$$

and

$$\Upsilon_-(n) = \Upsilon_n^{(d)}. \quad (4.30b)$$

Substituting Eqs. (4.26), (4.27a) and (4.27b) into Eq. (4.20), it can rewrite the ray series as

$$P(\omega) = \frac{1}{4\pi} \sum_{n=1}^{\infty} \sum_{m=m_-(n)}^{m_+(n)} \left[\Gamma_{m,n} \frac{e^{ikR_{m,n}}}{R_{m,n}} + \bar{\Gamma}_{m,n} \frac{e^{ik\bar{R}_{m,n}}}{R_{m,n}} \right], \quad (4.31)$$

where $m_-(n)$ and $m_+(n)$ are obtained by comparing Eqs. (4.27a) and (4.27b) with Eq. (4.1b) in order to determine whether an image source contribute to the total sound field. The expressions for $m_-(n)$ and $m_+(n)$ can be simplified considerably if the source is located at the centre of the street canyon, i.e. $x_s = W/2$. In this case, $W_{(m)}$ can be set as $W/2$ in Eq. (4.1b). It is then straightforward to show that

$$m_-(n) = \frac{-(W/2 + x_r)Y_L + W[nB - B_{(n)}]/2}{[y_n - Y_L]W} \quad (4.32)$$

and

$$m_+(n) = \begin{cases} \frac{y_n W - Y_L x_r}{(y_n - Y_L)W} & \text{if } \phi_n^{(u)} > \phi_n^{(h)} \\ \frac{-(Y_L + B)x_r}{[y_n - (Y_L + B)]W} & \text{otherwise} \end{cases} \quad (4.33)$$

4.2.4 An incoherent model for noise transmission

Using the ray model described in the last two sections, the total sound intensity by summing all contributory components incoherently can be calculated. For the receiver located at the opposite end of the cross junction in a street canyon, the total sound intensity, I , is given by

$$I = I_{\text{ref}} \sum_m V_m \left(\frac{R_m}{D_m^2} + \frac{\bar{R}_m}{\bar{D}_m^2} \right) , \quad (4.34)$$

where I_{ref} is the free field sound intensity of the source at 1 m from the source of unit strength. Again, the visibility factor V_m is determined according to Eq. (4.18). The respective distances from the source or image sources to the receiver R_I are denoted by $D_m = D(S_m | R_I)$ and $\bar{D}_m = D(\bar{S}_m | R_I)$. The reflection factors, R_m and \bar{R}_m , are the combined reflection coefficient associated with the respective image source S_m and \bar{S}_m .

The reflection factors are calculated by using the absorption coefficients of the walls (α_A and α_B respectively for the left and right façade of the first street canyon) and the

ground (α_G). The amplitude of R_m is reduced by a reflection factor $(1-\alpha_A)$ for each interaction with the left façade and a factor of $(1-\alpha_B)$ for the right façade. In addition to the corresponding interaction with the façade surfaces, an extra reduction factor of $(1-\alpha_G)$ is required for the amplitude of \bar{R}_m as the rays hit the ground surface.

In light of Eq. (4.34), the sound intensity for the receiver located in the second street canyon can be calculated analogously to give

$$I = I_{\text{ref}} \sum_{n=1}^{\infty} \sum_{m=m_-(n)}^{m_+(n)} \left[\frac{R_{m,n}}{D_{m,n}^2} + \frac{\bar{R}_{m,n}}{\bar{D}_{m,n}^2} \right] \quad , \quad (4.35)$$

where $D_{m,n} = D(S_m | R_n)$ is the distance from the image source S_m to the image receiver R_n and $\bar{D}_{m,n} = D(\bar{S}_m | R_n)$ is the distance from the image source \bar{S}_m to the image receiver R_n . The parameters, $R_{m,n}$ and $\bar{R}_{m,n}$, are the respective reflection factors due to multiple reflection from the four façade surfaces (with the respective absorption coefficients of α_A , α_B , α_C and α_D) and the ground surface (with the absorptive coefficient of α_D). Again, these reflection factors are determined in the same way as R_m and \bar{R}_m .

4.3 Experimental validations

A full scale field measurement was conducted in a junction of an alley street in order

to validate the theoretical models described in Sec. 4.2. The main street where the source was located 3.1 m wide, 50 m long. The second street was 3.25 m wide and 70 m long. The surrounding buildings were about 65 m high, the façade surfaces were decorated with hard mosaic tiles and the ground was constructed of concrete.

Initial measurements were conducted to characterise the acoustic impedances of the boundary surfaces. In these measurements, the source was separated at a distance of 1 m from the receiver and both of them were placed at the same perpendicular distance of 0.1 m from the respective boundary surfaces. The excess attenuation (EA) spectrum was measured where EA is defined as the ratio of the total field above the boundary surface to the free field at 1 m. See later in this chapter for the equipment used in these measurements.

The corresponding acoustic characteristics of the façade and ground surfaces can be deduced from the measured EA spectra. Again, Attenborough's two-parameter model [89] that mentioned in Chapter 2.3.1 was used to model the acoustic impedance of the boundary surfaces in the present study. According to Attenborough's model, the normalised surface impedance is calculated by

$$Z = 0.538\sqrt{\sigma_e / f} + i[0.538\sqrt{\sigma_e / f} + 19.74\alpha_e / f] \quad (4.36)$$

where f is the frequency of the acoustic excitation, σ_e is the effective flow resistivity and α_e is the effective rate of change of porosity with depth. Essentially, σ_e and α_e were deduced by obtaining the best agreement between the predicted and measured EA spectrum. Figures 4.7(a) shows typical experimental results compared with theoretical predictions based on best-fit parameters for the acoustical characterisation of the façade surface. The best-fit parametric values for σ_e and α_e were 50,000 kPa s m⁻² and 500 m⁻¹ respectively. The acoustical characterisation of the hard ground is shown in Figure 4.7(b). The best-fit parametric values for σ_e and α_e were 200,000 kPa s m⁻² and 500 m⁻¹, respectively.

It is remarkable that the one-third octave band absorption coefficients (α) of the boundary surfaces are required for the incoherent model. They can be calculated from the deduced impedance by using the following formula [54],

$$\alpha = \left| \frac{Z - 1}{Z + 1} \right|^2 \quad (4.37)$$

The calculated absorption coefficients of the hard ground and the façade surfaces from 400 Hz to 8000 Hz in one-third octave bands are listed in Table 4.1.

A Renhus-Heinz type PN 61 self-powered loudspeaker and a Brüel & Kjær type 4189 pre-polarised free field 1/2” condenser microphone were connected to a PC-based

maximum length sequence system analyser (MLSSA) [89]. A set of pseudo-random signals was generated and broadcast through the loudspeaker. The signals received at the microphone were then recorded and subsequently processed by MLSSA.

The source was situated at the centreline of the main street and at 1.235 m above the ground. The co-ordinate of the source is given by (1.55, 0, 1.235). The receiver was placed at 0.995 m above ground but it was moved along the centreline of the two streets for different sets of measurements. The first set of measurements was conducted where the receiver was placed along the main street in which the sight-line contacts between the source and receiver was maintained. In this case, the receiver location is given by (1.55, h_y , 0.995) where h_y is the horizontal distance measured from the source plane to the reception point. The second set of measurements was carried out when the receiver was placed in the second street at (h_x , 6, 0.995) where the horizontal distance h_x is measured from the centreline of the main street to the reception point along the second street. Figure 4.8 shows the experimental setup of the outdoor measurements.

To illustrate the validity of the numerical models, the narrow-band EA spectra for three different receiver locations are first compared. Figures 4.9 (a) and (c) show the

measured EA spectra for the receiver locating along the main street before and after the junction at (1.55, 3, 0.995) and (1.55, 12, 0.995) respectively. Figures 4.9 (b) and (d) show the respective numerical predictions according to the coherent ray model described in Secs. 4.2 (A) and (B). Figure 4.9 (e) and 9(f) display comparisons of the corresponding EA spectra for the receiver located along the second street at (-4.45, 6, 0.995) where the numerical model is based on the coherent ray model discussed in Sec. 4.2.3.

As shown in the characterisation of the boundary surfaces (see Fig. 4.7), the façade and ground used in the present study are relatively hard acoustically. Hence, the total sound field in the street canyon is composed of many small ray terms with different phase angles due to the effect of multiple reflections. The EA spectra are expected to be highly oscillatory especially at high frequencies which are confirmed by the measured data. As shown in Fig. 4.9, there are places where discrepancies between the measured results and numerical predictions are significant. It is understandable because a smooth and flat impedance plane is used to approximate the rather complicated façade surfaces. For instance, downpipes, recess areas and large scattering surfaces are present at the experimental test site as shown in Fig. 4.8. Despite these apparent non-uniformities in the test site, the coherent ray model is able

to predict comparable interference patterns and similar levels of fluctuations in the excess attenuation spectra.

It is also useful to conduct octave-band analyses of the measured sound fields. These results can be compared with the incoherent ray models described in Sec. 4.3.4. From the narrow-band EA spectrum, it is possible to determine the sound pressure level relative to the free field noise level measured at 1 m from the source. Suppose that there are i narrow bands within an octave band, then the relative sound pressure level (ΔSPL) at this octave band is given by

$$\Delta SPL = \left[\sum_i p_i^2 \times 10^{|EA_i|/10} \right] / \left[\sum_i p_i^2 \right] \quad (4.38)$$

where p is the free field sound pressure and EA is the excess attenuation and the subscript i represents the corresponding parameters at each of the narrow bands.

Figure 4.10 shows the measured ΔSPL spectra for 5 receiver locations at (1.55, 3, 0.995), (1.55, 9, 0.995), (1.55, 12, 0.995), (-1.45, 6, 0.995) and (-4.45, 6, 0.995). It can be seen that the numerical predictions according to the coherent ray model agree reasonable well with experimental measurements. The incoherent model can estimate the general trend of the measuring results. The agreement between numerical predictions of the coherent model to experimental measurements is better than the

incoherent model to the measurements. However, the average deviation of two prediction models was about 3 dB.

Finally, Fig. 4.11 shows the variation of ΔSPL with the horizontal distance from a source plane where it is either:

- (i) h_y for the receiver located along the centreline of the main street at $(1.55, h_y, 0.995)$, or
- (ii) h_x for the receiver located along the second street at $(h_x, 6, 0.995)$.

Typical numerical results and measured data are presented for the source frequencies at 2 and 4 kHz. Shown in the figure, both the coherent ray model and inherent model tolerable agreed with the measuring results. The agreements between measurements and numeral predictions of both models are similar.

4.4 Prediction of noise attenuation in street canyons with a cross-junction

By referring to the Sec. 4.3 results, it can be seen that the coherent ray model suggests better prediction than the incoherent model but the incoherent model still can predict the general trend of the measurements. In order to speed up the following study, all predictions in the current section are calculated by the incoherent ray model rather

than the coherent model. In order to generalise the calculation, all distance units are based on the width of the first street and shown as DWR (Distance to Width Ratio) which can be calculated by dividing the source/receiver separation by the width of the first street. In the following study, the width of the second street is assumed to be the same as the first street, i.e. $W = B$. Both source and receiver are located in the centre of the street but the source is located in 0.2 DWR above ground and the receiver is located in 0.3 DWR above ground.

First, it is found that the sound fields within the same cross sections of the second street and the after junction region of the first street are generally uniform except when the receiver is very close to the junction. This is similar to what previous studies obtained [56, 101]. For approximation, the sound fields within the same cross section can be assumed as uniform in all four legs of a street junction. Since the prediction results are similar to previous studies, simulation results are not shown here again.

On the other hand, it is interesting to find out the noise attenuation characteristics of the junction location in the first street when the source/receiver separation is fixed. In the simulation, the widths of both the first street and second street are the same. The distance between the junction and the source was 1.5 DWR and increased to 4.5 DWR

in step of 1 DWR. As shown in figure 4.12, basically, the noise level at the receiver do not relate to the distance between the source and the junction.

Figure 4.13 shows the relationship between the absorption coefficient of both the vertical/horizontal boundary surfaces and the noise attenuation in the after junction region of the first street. Since it was confirmed that the distance between the junction and source does not affect the noise level at the receiver, the source is fixed 1.5 DWR away from the junction in the simulation.

By comparing the excess attenuation of a normal street canyon, it can be seen that the opening of the second street is an efficient absorber when the receiver is close to the junction. The sound field “absorbed” by the second street decreased as the separation between the junction and receiver increased or the absorption coefficient of the boundaries increased. This is an interesting characteristic but not difficult to understand. First, the opening of the second street is assumed as a full absorber. The sound field at the receiver decreased proportional as the area of absorber increased. In other words, most of the sound field is absorbed by the opening of the second street when the receiver is close to the junction but “averaged” absorption decreased as the separation between the receiver and junction increased. On the other hand, part of the

sound energy is absorbed by the boundary surfaces when sound wave travels in the street canyon. The sound power absorbed by the opening of the second street becomes less importance when the absorption coefficient of the boundary surfaces increased and can be neglected when the absorption coefficient of the boundary surfaces is 0.35.

Fig. 4.14 displays the sound field in the second street which refers to the co-related location of a normal street canyon. It is demonstrated that the sound field in the second street is much smaller than the sound field in the co-related location of the normal street canyon, especially when the receiver far away from the source. As shown in the figure, the sound field in the second street is 2.5 dB smaller than in the co-related location of a normal street canyon when the absorption coefficient is 0.05 and decreased to 26 dB when the absorption coefficient increased to 0.35. An effective way to reduce the transportation noise in the second street is by increasing the absorption coefficient of the boundary surfaces. Planting is one of the solutions.

The width of the second street is the other factor that affects the sound field in the after junction region of the first street. The sound fields in the after junction region of first street are simulated against the widths of the junction. In figure 4.15, the prediction results are compared with the excess attenuation of a normal street canyon

and the direct sound field between source and receiver with related ground reflection.

It can be seen that the excess attenuation of the after cross region of first street does not relate to the width of the junction while the width of the junction is smaller than the width of the first street. The sound field at the after cross region decreases as the width of the second street increases. By comparing to the sound field of the sound and receiver which is placed on a flat plane with the same configuration, it can be seen that most of the sound rays go into the second street when the receiver is close to the junction but the absorption of the junction becomes less important when the receiver is far away from the junction.

4.5 Summaries

Transportation noise is one of the major issue in a high-rise city. A single point transportation noise can be propagated through street canyons, cross junctions and flat land before reaching the whole city. Although the propagation network of the transportation noise includes street canyons, cross junctions and flat lands, the studies related to sound field propagation in cross junctions are related limited. In the present study, a coherent ray model has been developed to estimate the steady-state sound fields and reverberation times for the four legs of a cross junction. An incoherent model also has been mentioned in the study. It has been demonstrated that the

predictions according to the coherent ray model agreed reasonably well with experimental data obtained in a real application. The incoherent model can estimate the “mean” value of the experimental data. The absorption effect of the second street was studied by incoherent model. The second street can be considered as an effective absorber when the receiver is close to the junction but the absorption power decreased as the receiver/junction separation increased. The separation of source/junction does not affect the steady-state sound field at the opposite end of the street canyon. For simple consideration, the opening of the second street can be neglected if the receiver is faraway from the junction.

Tables

Frequency (Hz)	400	500	630	800	1000	1250	1600
Absorption coefficient of vertical façades	0.028	0.03	0.036	0.041	0.046	0.052	0.059
Absorption coefficient of hard ground	0.011	0.013	0.014	0.016	0.018	0.020	0.023
Frequency (Hz)	2000	2500	3150	4000	5000	6300	8000
Absorption coefficient (Outdoor façade)	0.067	0.075	0.084	0.094	0.11	0.12	0.13
Absorption coefficient of hard ground	0.026	0.028	0.032	0.036	0.04	0.045	0.05

Table 4.1: The estimated mean one-third octave band absorption coefficients of the boundaries given in dB.

Figures

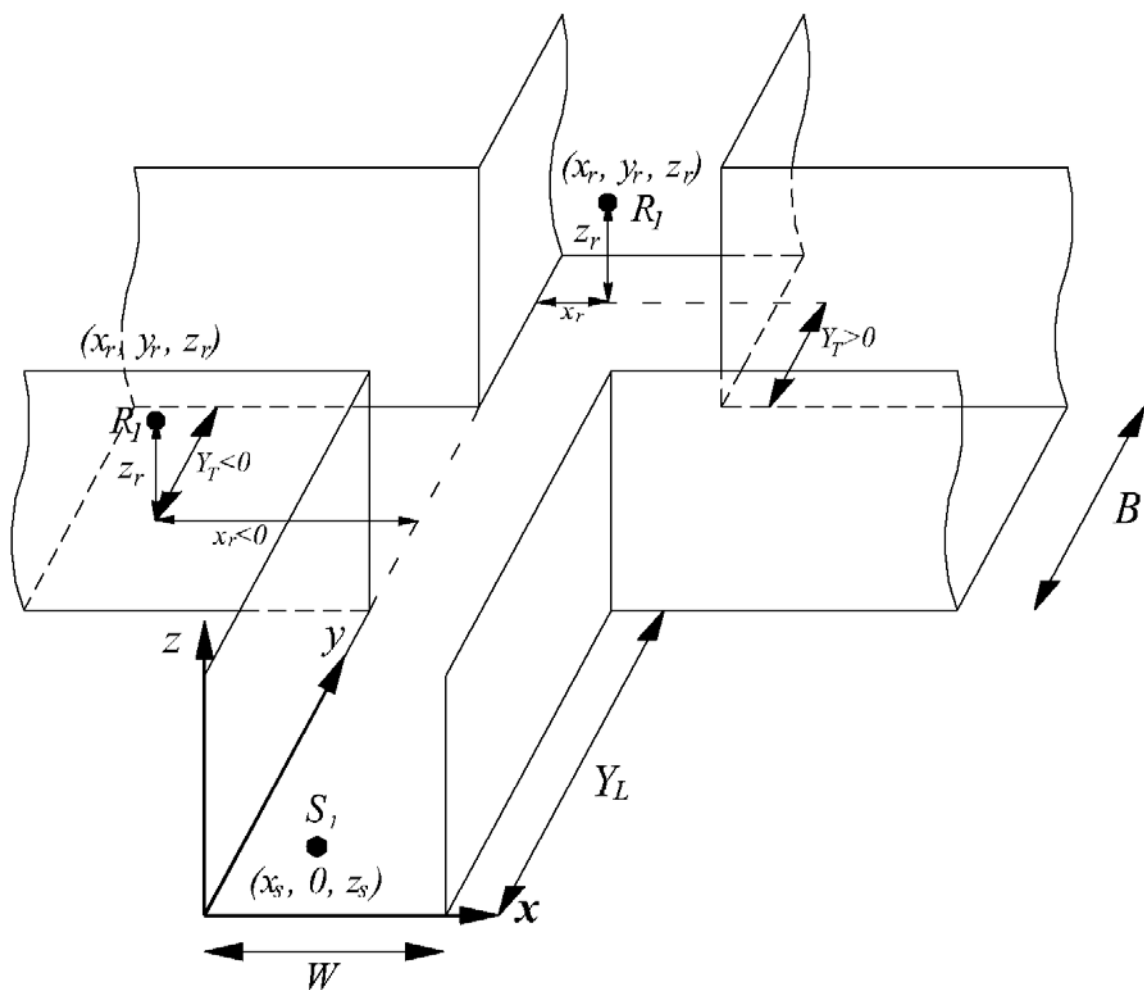


Fig. 4.1: Schematic diagram showing the rectangular coordinate system and the geometrical configuration of a junction in a street canyon.

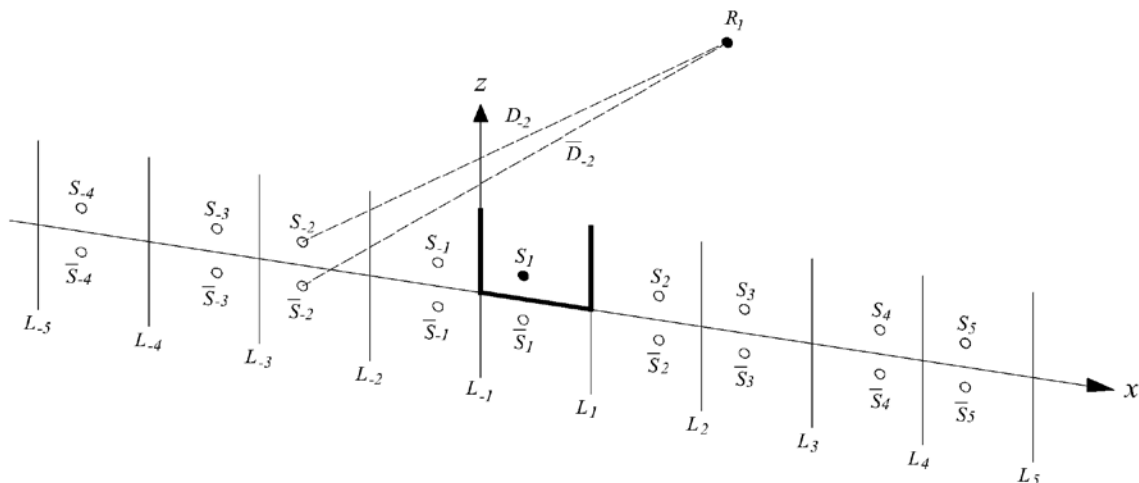


Fig. 4.2: Schematic diagram shows the relative locations of the receiver, the real sound source (solid circle), image sources (open circle) and the corresponding distances of the receiver (above and below the ground surface).

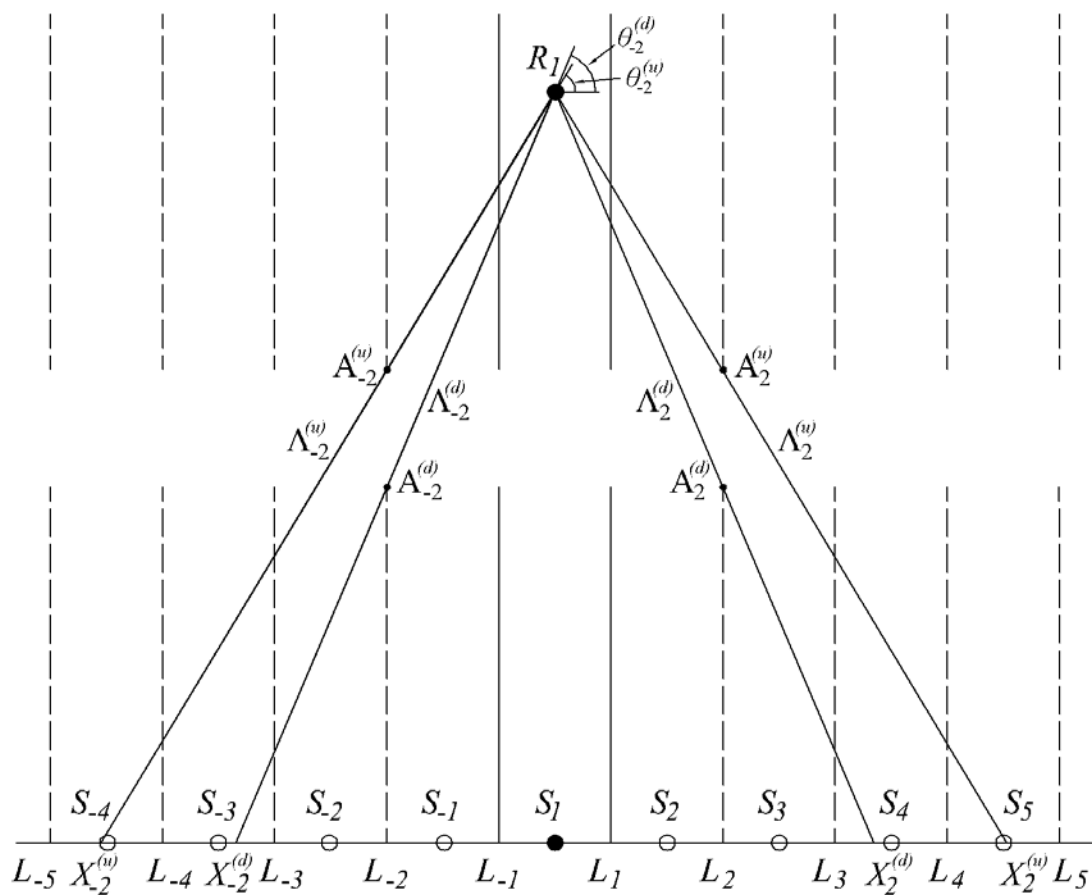


Fig. 4.3: Schematic diagram showing the simplified 2-D geometrical configuration of a junction in a street canyon with the point source and receivers locations.

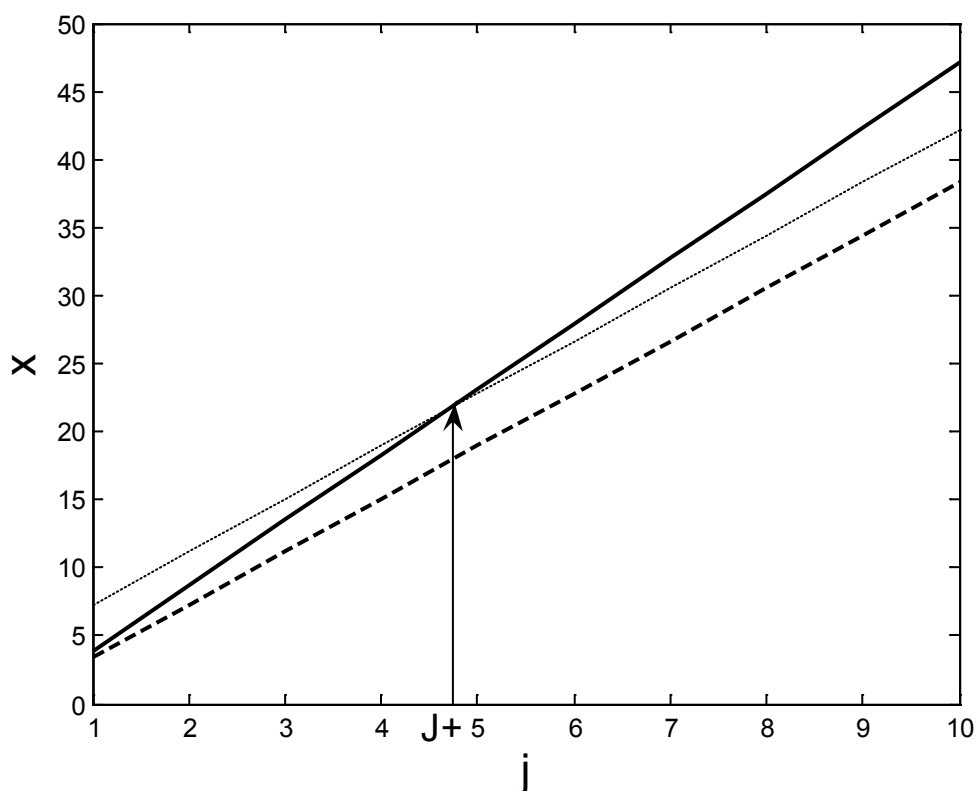


Fig. 4.4: Schematic diagram showing the number of term (J_+) required while all image sources go into the second street. The thick solid line is the value of $X_j^{(u)}$, the dashed thick line is the value of $X_j^{(d)}$ and the dashed thin line is the value of $X_{j+1}^{(d)}$. The width of the first street and second street are 3 m. The second street crosses the first street at 4.5 m away from the source. Both source and receiver are located at the centre of the first street and separation is 20 m.

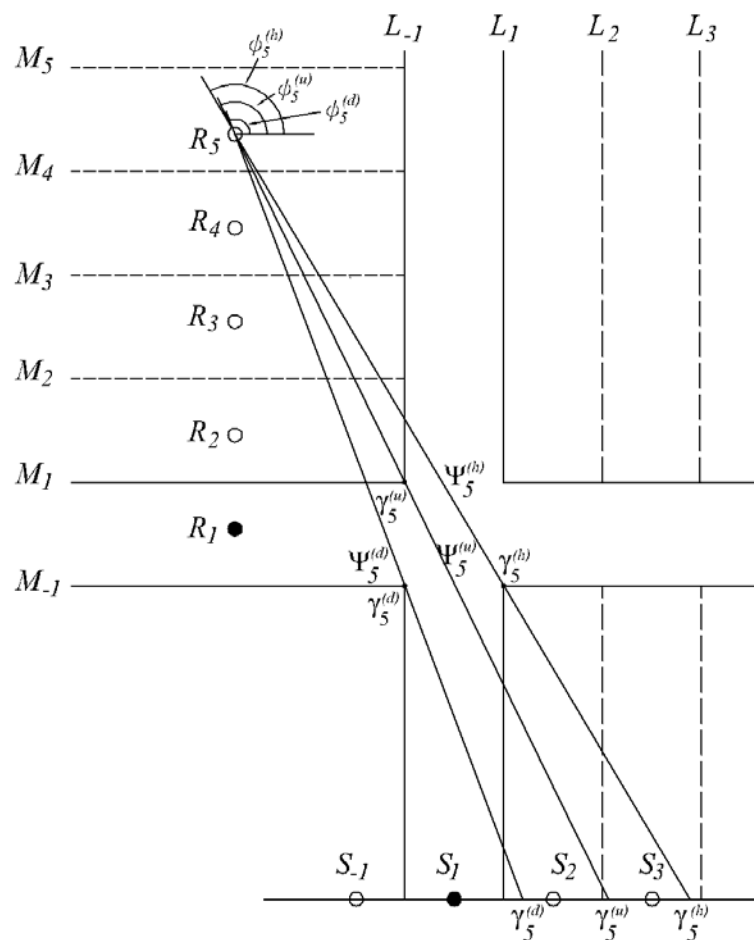


Fig. 4.5: Schematic diagram to show the sound ray travelling path from image receiver n to image sources when the receiver located in the second street canyon.

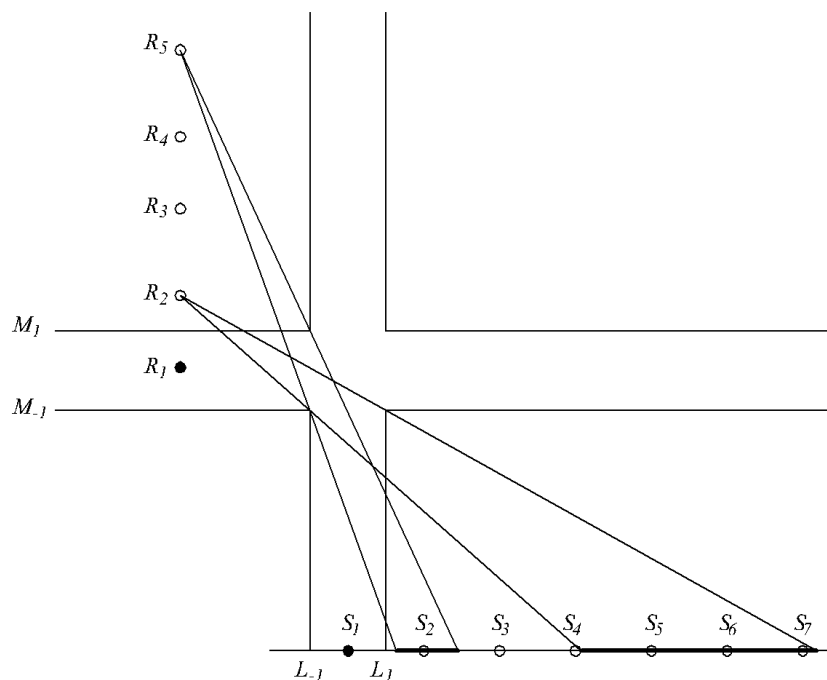


Fig. 4.6: Schematic diagram to show the image sources which can reach the image receivers when the source is located in the first street but the receiver locates is located in the second street and both source and receiver cannot “see” each other.

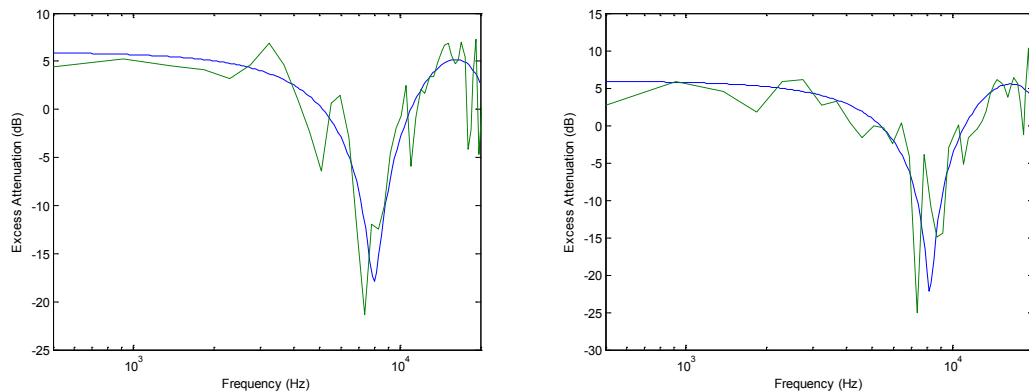


Fig. 4.7: The acoustic characterisation of (a) the vertical facades and (b) the hard ground. The two-parameter model was used to characterise the surface impedances. The solid lines are (—) are theoretical predictions and the dotted lines (-----) are experimental data.



Fig. 4.8: Photograph showing the setup of the field measurement.

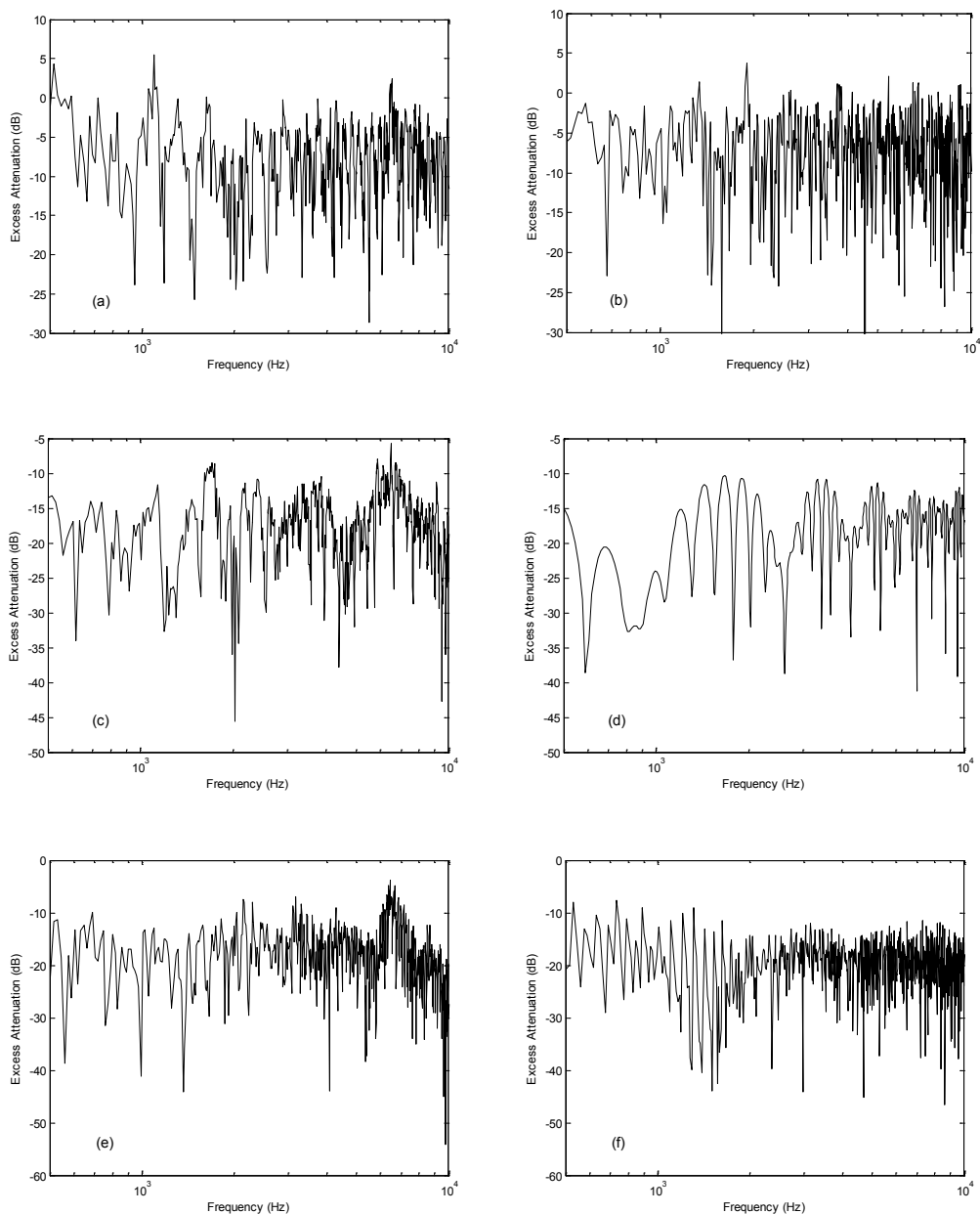


Fig. 4.9: Comparisons of measured data with predicted excess attenuation by coherent ray model for different receiver locations. Figures marked with (a), (c) and (e) are the measured data and the (b), (d) and (f) are the predictions of the correlated location. The detail location of the measurement pointed are given in Ch. 4.3.

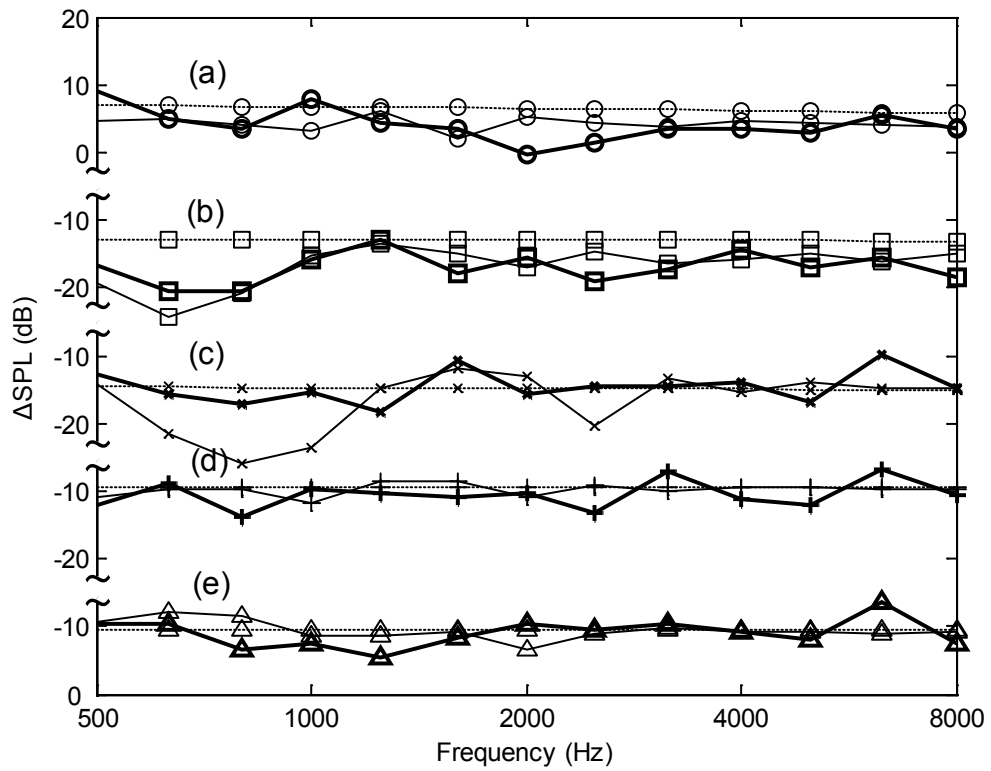


Fig. 4.10: The relative sound pressure level (ΔSPL) verse frequency for various receiver locations. The thick solid lines are experimental data, the thin solid lines are predictions by the coherent ray model and the dashed thin lines are predictions by the incoherent model. In (a) to (c), receivers were located in first street but fixed in second street in (d) to (e), The detail source and receiver locations are listed out at Ch. 4.3.

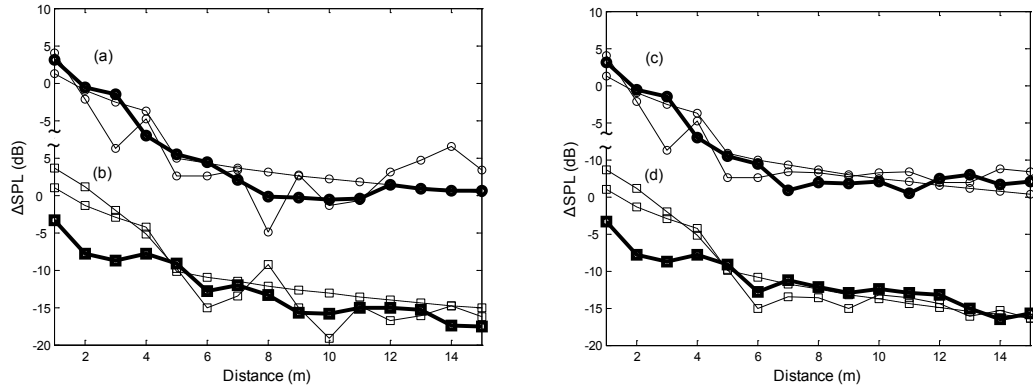


Fig. 4.11: The relative sound pressure level (ΔSPL) is plotted versus the horizontal distance. The source was fixed in the first street, 1.55 m away from both vertical boundaries and 1.235 m above the ground. The receiver was located at centreline of the first street in (a) and (b), 0.995 m above the ground. In (c) and (d), the receiver was located at centreline of the second street and above the ground. The distance shown in (c) and (d) is referenced to the centre point of the junction. The thick solid lines are experimental data, the thin solid lines are predictions by the coherent ray model and the dashed lines are predictions by the incoherent model. The lines with open circles and squares are for the frequencies of 2 kHz and 4 kHz.

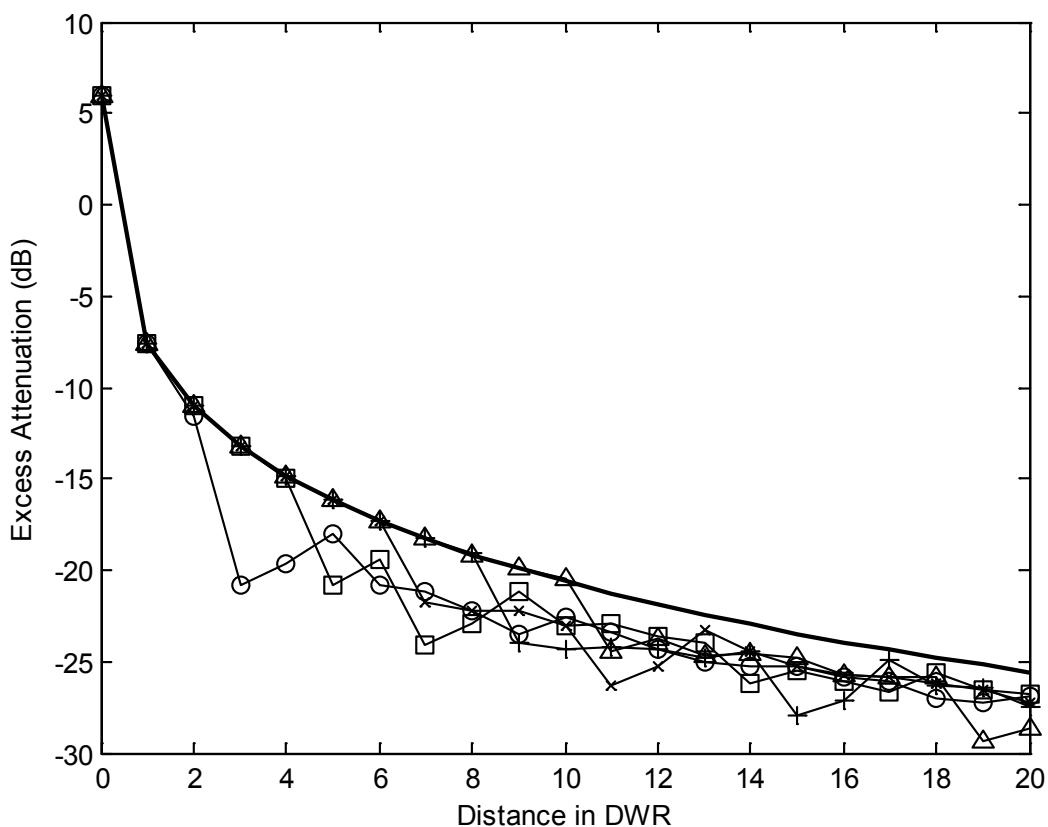


Fig. 4.12: The excess attenuation (EA) against distance in DWR (distance to width ratio). The widths of both the first street and second street are the same. Both source and receiver are located at the centre of the street and the source is 0.2 DWR above ground but the receiver height is 0.3 DWR. The thick solid line is the excess attenuation of a normal street canyon. Thin solid line marked with open circles is the EA when the second street crosses the first street at 1.5 DWR, thin solid line marked with squares is 3.5 DWR, thin solid line marked with crosses is 5.5 DWR, thin solid line marked with plus signs is 7.5 DWR and thin solid line marked with triangles is 9.5 DWR.

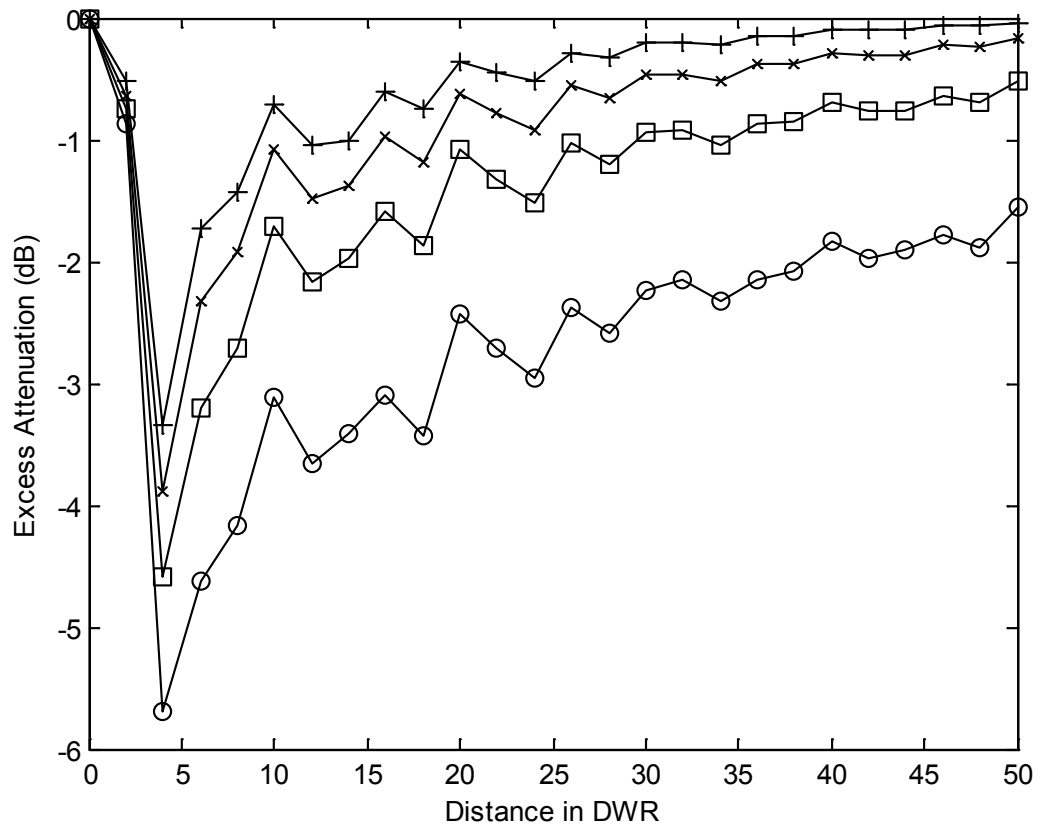


Fig. 4.13: The attenuation against distance in DWR (distance to width ratio) of the first street. The widths of both the first street and second street are the same. The second street crosses the first street at 1.5 DWR away the source. Both source and receiver are located in the centreline of the first street and the heights are 0.2 DWR and 0.3 DWR respectively. The absorption coefficient of thin solid line marked with open circles is 0.05, thin solid line marked with squares is 0.15, thin solid line marked with crosses is 0.25 and thin solid line marked with plus signs is 0.35.

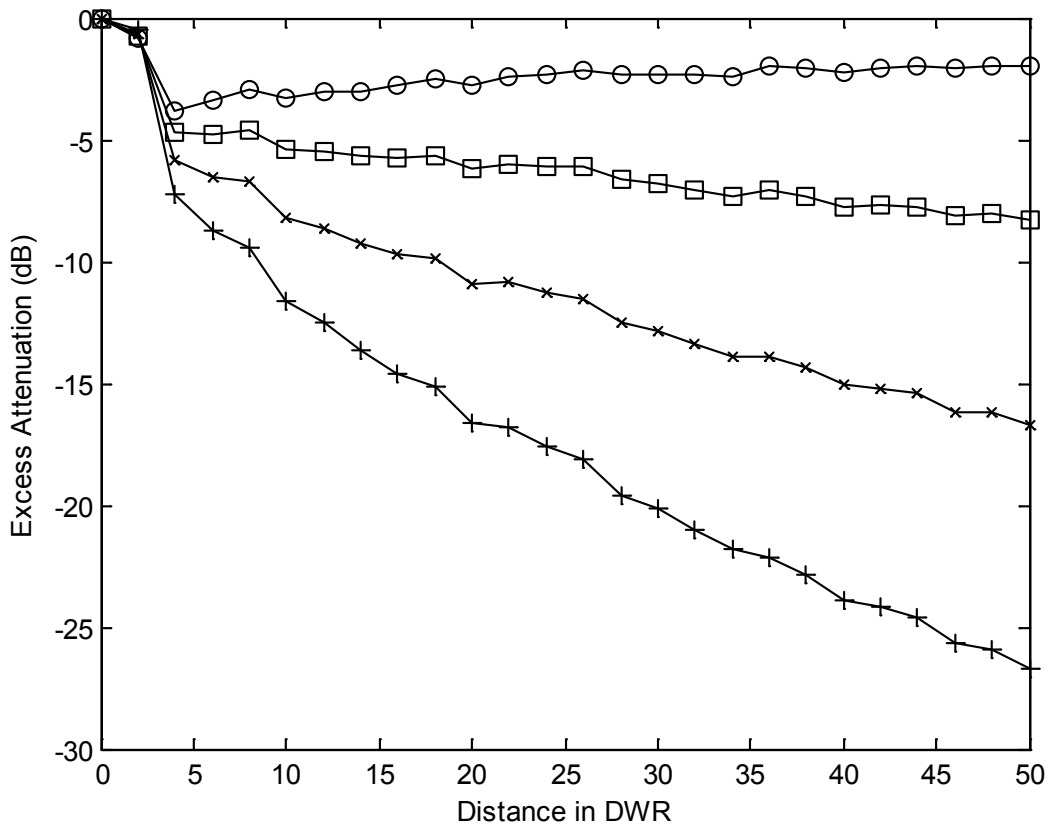


Fig. 4.14: The relative sound pressure level (ΔSPL) against distance in DWR (Distance to Width Ratio) of the second street. The second street crosses the first street at 1.5 DWR away the source. The source is located in the centreline of the first street and 0.2 DWR above ground. The receiver is located in the centreline of the second street and 0.3 DWR above. The absorption coefficient of thin solid line marked with open circles is 0.05, thin solid line marked with squares is 0.15, thin solid line marked with crosses is 0.25 and thin solid line marked with plus signs is 0.35.

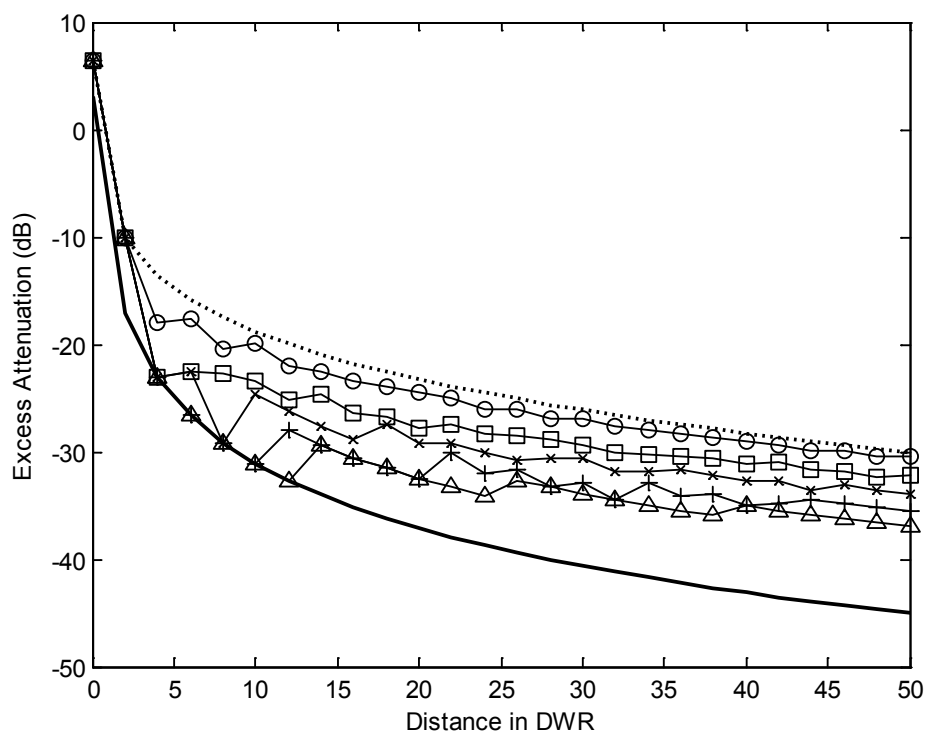


Fig. 4.15: The excess attenuation against distance in DWR (distance to width ratio) of the first street. The second street crosses the first street at 2 DWR away from the source. Both source and receiver are located in the centreline of the first street and the heights are 0.2 DWR and 0.3 DWR respectively. The absorption coefficient of all boundary surfaces is 0.05. The thick dashed line is the excess attenuation of a street canyon without any cross junction. The width of the second street is 0.5 DWR of the first street which is shown by the thin solid line marked with open circles, 1.5 DWG by the thin solid line marked with squares, 2.5 DWR by the thin solid line marked with crosses, 3.5 DWR by the thin solid line marked with plus signs, 4.5 DWR by the thin solid line marked with triangles and thick solid line is the excess attenuation between the source and receiver plus ground reflection.

Chapter 5

Sound propagation in a long enclosure with a T-intersection

5.1 Introduction

Both audibility and intelligibility are the well known factors in acoustic study. However, audibility does not imply intelligibility. In order to deliver fire drills, verbal warnings and general announcements, public address (PA) systems are normally installed in long enclosures. Increasing the sound power output of the PA system will increase the audibility but not necessarily improve the speech intelligibility directly. A loud enough public address system can delivery audibility information to public but the content of the information may not be totally identifiable. In other words, an audible speech can be completely unintelligible when the speech is blurred by reverberations and echoes. From a technical point of view, the audibility mainly relies on the signal to noise ratio (speech to noise ratio) but the intelligibility is affected by both the signal to noise ratio and reverberation times in long enclosures [1 - 2].

The long enclosure is a total different acoustical environment meaning that the classical Sabine theory is unsatisfactory [46]. Nowadays, the ray tracing technique [49] and image source methods [47, 48] are two common models to fathom both reverberation times and steady-state sound fields in long enclosures. The coherent image source method was introduced to improve the prediction accuracy of the image source method [51 – 54]. Apart from the straight long enclosure, there are other variations: a long enclosure with a T-intersection and U-turn long enclosures are commonly found in office buildings, shopping malls, residential houses and schools. Bend and cross-junction long enclosures are frequently found in railway stations and underground tunnels. This study focuses on the sound field propagation in branching long enclosure. It has become necessary because the related studies are limited in number and lacked of detail [39 – 41]. In the current study, a systematic formulation is developed to predict the steady-state sound fields and reverberation times for the long enclosure with a T-intersection. The formulation is based on the coherent image source method.

5.2 Theory

5.2.1 The steady state sound field at a receiver

5.2.1.1 Sound field of a straight long enclosure

In the current consideration, a long enclosure with width of a and height of h is modelled as a rectangular enclosure but of infinite length. The branch of a T-intersection is modelled as the other infinite length rectangular enclosure with the same height of the main enclosure but with a width of b and which intercepts the main enclosure perpendicularly in a distance of y_a to the origin. The origin is chosen at the left bottom corner of the cross section of the source plane. The x - y - z co-ordinate is chosen so that the width of the enclosure a should be measured in the x -direction, while the height of the enclosure h is measured in the z -direction. The y -axis is placed along the direction of the main long enclosure. See Figure 5.1 for detail. Suppose that the real source $S_{0,0}$ is located at $(x_s, 0, z_s)$ and that the source is placed at a distance of x_s away from left parallel wall and at z_s above ground. The receiver R_0 has a co-ordinate of (x_r, y_r, z_r) .

There is a limit of three source locations that need to be considered in the study,

- (i) the source is located in the main enclosure and the T-branch is located on the left hand side of the source,
- (ii) the source is located in the main enclosure and the T-branch is located on the right hand side of the source,
- (iii) the source is located in the T-branch.

Actually, only the first situation needs to be focused on, when the source is located at the main enclosure and the T-branch is located on the left hand side of the source. For the second situation, when the T-branch is located on the right hand side of the source, it can be considered as a mirror setup of the first situation. The source and receiver locations can be converted as $(a-x_s, 0, z_s)$ and $(a-x_r, y_r, z_r)$ and the formulation developed for first situation can be used. The third situation, when the source is located in the T-branch is out of the scope of the current study, so it will not be discussed any further.

The challenge in the current study is to estimate the transmission of sound in different locations of the enclosure. The image source method is one of the popular methods used in earlier studies to predict the sound field in long enclosures but can not directly be applied here since the receiver \mathbf{R}_0 is separated from the source $\mathbf{S}_{0,0}$ by a T-junction.

Figure 5.2 shows a schematic diagram of the relative locations of sources and receiver. Based on the image source model, a row of image sources is created by the reflections of the vertical boundaries and their images. The x -coordinates of these image sources are given by

$$x_{\pm m} = ma + a_{(m)} \quad \text{for } m = 0, 1, 2, 3, \dots, \quad (5.1a)$$

where

$$a_{(m)} = \begin{cases} a - x_s & \text{if } m \text{ is odd} \\ x_s & \text{if } m \text{ is even} \end{cases} . \quad (5.1b)$$

Similarly, infinite columns of image sources are formed due to the reflections of the horizontal boundaries and their images. The z -coordinates of these image sources are determined by

$$z_{\pm n} = nh + h_{(n)} \quad \text{for } n = 0, 1, 2, 3, \dots, \quad (5.2a)$$

where

$$h_{(n)} = \begin{cases} h - z_s & \text{if } m \text{ is odd} \\ z_s & \text{if } m \text{ is even} \end{cases} . \quad (5.2b)$$

The distance between the real source $S_{0,0}$, image source $S_{m,n}$ and receiver R_0 can be estimated by,

$$L_{m,n} = L(S_{m,n} | R_0) = \sqrt{(x_m - x_r)^2 + y_r^2 + (z_n - z_r)^2} . \quad (5.3)$$

As shown in figure 5.2, the total sound field due to a monopole source of unit strength in a straight long enclosure can be calculated by summing all contributions coherently to give:

$$P(\omega) = \frac{1}{4\pi} \sum_{m=-\infty}^{\infty} \sum_{n=-\infty}^{\infty} \frac{Q_{m,n} e^{ikL_{m,n}}}{L_{m,n}} \quad (5.4)$$

where $k(\equiv \omega/c)$ is the wave number, ω is the angular frequency of the source, c is the speed of sound in air, $Q_{m,n}$ is the combined complex wave reflection coefficient of the boundaries that the image source $S_{m,n}$ travelled through to reach the receiver R_0 .

The combined reflection coefficient $Q_{m,n}$ due to the image source $S_{m,n}$ can be determined by multiplying the individual spherical wave reflection coefficient of each vertical and horizontal boundary which image source $S_{m,n}$ travelled through and is obtained by,

$$Q_{m,n} = Q_m \times Q_n \quad (5.5)$$

where Q_x is defined as

$$Q_x = Q_+^{|x+g(x)|/2} Q_-^{|x-g(x)|/2} \quad (5.6a)$$

and the functions $g(x)$ is given by

$$g(x) = \begin{cases} 1 & \text{if } x \text{ is an odd integer} \\ 0 & \text{if } x \text{ is an even integer} \end{cases} \quad (5.6b)$$

The Q_+ is the spherical wave reflection coefficient of the boundary surface located at the positive side of the x - z co-ordinate system and Q_- is the spherical wave reflection coefficient of the boundary surface located at $(0, 0, 0)$ of the x - y - z co-ordinate system. The spherical wave reflection coefficient of individual surface is determined by

$$Q = R_p + (1 - R_p)F(w) \quad (5.7)$$

where the plane wave reflection coefficient R_p is given by

$$R_p = \frac{\cos \theta - \beta}{\cos \theta + \beta} \quad (5.8)$$

and θ is the incident angle of the reflected wave measured from the normal of impedance surface. The boundary loss factor $F(w)$ of the surface is defined by

$$F(w) = 1 + i\sqrt{\pi}we^{-w^2} \operatorname{erfc}(-iw) , \quad (5.9)$$

and w is known as the numerical distance and is determined by

$$w = \sqrt{kD/2}(1+i)(\cos\theta + \beta) . \quad (5.10)$$

5.2.1.2 Sound field at the opposite end of the main enclosure

When the receiver is located in the opposite end of the main enclosure, part of the sound waves are transmitted into the side branch and are unable to reach the receiver.

The total sound field estimated by Eq. (5.4) cannot be directly applied in the current case. In this situation, the junction between the side branch and the main enclosure can be treated as an anechoic surface with perfect absorption since it is not possible for a sound ray to reflect back to the main enclosure when it hits the junction. A visibility factor V_m is added to Eq. (5.4) to represent the establishment of direct linking between sources and receiver. The visibility factor is based on each image source and receiver pair. It is set to 1 when a direct link can be established between the receiver R_0 and the image source $S_{m,n}$. Otherwise, it is zero. After the visibility factor is added to Eq. (5.4), the total sound field due to a monopole source of unit strength is given by,

$$P(\omega) = \frac{1}{4\pi} \sum_{m=-\infty}^{\infty} \sum_{n=-\infty}^{\infty} V_m \frac{Q_{m,n} e^{ikL_{m,n}}}{L_{m,n}} . \quad (5.11)$$

Figure 5.3 shows the three dimensional view of the real source, image sources, real

boundary surfaces, image boundary surfaces of the main enclosure and the receiver. The anechoic surface is represented by a grid and the related images are represented by a shadow. All boundary surfaces of the side branch and related images are not shown for clarity. It can be seen that the side branch opening and their images create columns opening in the main enclosure and their related images. When the connection between the image source and receiver pass through the anechoic surface, whole column image sources will hit that anechoic surface as well. Actually, the vertical distance (in z -coordinates) between the image source $S_{m,n}$ and the receiver R_0 will not affect whether sound wave pass through the side branch opening or not. The visibility factor is only related to the x - y coordinates of the image source and receiver. In this case, it is much easier to consider the visibility factor in 2-D rather than 3-D.

Figure 5.4 shows the top view of Fig. 5.3. Again, the anechoic surface is replaced by an opening and the other boundaries of the side branch are not shown for clarity. It can be seen that part of the sound waves hit the anechoic surface and are unable to reflect back to the main enclosure, so the visibility factor is zero in this case. Now, the coordinates should be determined of the two edges (named as E_x^F and E_x^N in Figure 4) of the anechoic surface m as $(aj_{(m)}, y_a + b)$ and $(aj_{(m)}, y_a)$ where

$$j_{(m)} = \begin{cases} 0 & \text{if } x \text{ is a odd integer} \\ m & \text{otherwise} \end{cases} . \quad (5.12)$$

The intercept points, F_m and N_m , of the sound rays which travel back from the receiver and pass through the two edges of the anechoic surface m and then reach the x -axes, are given by.

$$F_m = \frac{ay_r j_{(m)} - (y_a + b)x_r}{y_b} , \quad (5.13)$$

$$N_m = \frac{ay_r j_{(m)} - y_a x_r}{b + y_b} . \quad (5.14)$$

As shown in figure 5.4, sound rays radiated from the image sources bounded between F_m and N_m on x -axes should go into the side branch opening and never reach the receiver. The visibility factors of the bounded image sources should be set to zero. As mention before, the visibility factor can be considered as 2-D rather than 3-D, so, while the visibility factor of one image source is set to zero, the visibility factors of whole column image sources (in z -coordinate) also can be set to zero. The visibility factor becomes only dependent on the x -coordinate and gives,

$$V_m = \begin{cases} 0 & \text{if } F_s > x_m > N_s \\ 1 & \text{otherwise} \end{cases} \quad (5.15)$$

where s is a integer between 0 to m . It is used to calculate the two edges of the anechoic surfaces and then classify whether the image source m will hit the anechoic surface or not. The visibility factor should be set to zero when any F_s is larger than x_m and the x_m larger than the N_s when s increases/decreases from 0 to m

Figure 5.5 shows the bounded area of F_s and N_s on x -axes. It is simple to see that the bounded area is increasing simultaneously with the number of reflections on a vertical surface increasing. For $m > 1$, all image sources should go into the side branch when F_m is larger than the N_{m+2} . The summation of Eq. (5.11) can be reduced to a limit, say M_+ rather than go to infinite since all the visibility factors for the image sources after the boundary of M_+ should be zero. By comparing Eq. (5.13) and (5.14), it can obtain the M_+ as,

$$M_+ = \frac{(2ay_b + bx_r)}{ab} \quad . \quad (5.16)$$

A similar case happens for $m < 1$, as all image sources should hit the junction surface when F_m is smaller than the N_{m-1} . The number of reflections on x -axes can be reduced to,

$$M_- = \frac{(bx_r - 2ay_b)}{ab} \quad . \quad (5.17)$$

By combining Eq. (5.11), (5.16) and (5.17), the total sound field of the receiver which is located at the opposite end of the main enclosure is given by,

$$P(\omega) = \frac{1}{4\pi} \sum_{m=M_-}^{M_+} \sum_{n=-\infty}^{\infty} V_m \frac{Q_{m,n} e^{ikL_{m,n}}}{L_{m,n}} \quad . \quad (5.18)$$

5.2.1.3 Sound field at the side branch

When the receiver is located at the side branch, there is no direct sight line contact

between the real source and receiver. A similar case happens in the image receivers; the sound rays emitted from the image sources are still unable to reach the receiver without reflecting from the vertical boundary of the side branch. An image receiver is a way to represent the multiple reflections on the vertical boundary of the side branch [39, 40]. Figure 5.6 shows the top view of the coordinates of image receivers. It can be seen that the coordinates of these images only change in the y-axes. The y-coordinates of these image receivers are determined by

$$y_{\pm u} = y_a + ub + b_{(u)} \quad \text{for } u = 0, 1, 2, 3, \dots \quad , \quad (5.19a)$$

where

$$b_{(u)} = \begin{cases} b - (y_r - y_a) & \text{if } u \text{ is odd} \\ y_r - y_a & \text{if } u \text{ is even} \end{cases} \quad . \quad (5.19b)$$

As show in figure 5.6, the receiver is located on the right side of the source. There is no direct link that can be estimated between the source and the receiver. Besides the direct wave, there are only parts of the image sources that can create connections to the image receivers. After a detailed study, only the image sources created on the right side of the main enclosure ($m > 1$) can link to the image receivers located at the upper part of the 2-D view ($u > 1$). Now, the contribution of the image sources that can linked to the image receivers can be summed up and the total sound field is given by,

$$P(\omega) = \frac{1}{4\pi} \sum_{u=1}^{\infty} \sum_{m=1}^{\infty} \sum_{n=-\infty}^{\infty} V_{u,m} \frac{Q_{u,m,n} e^{ikL_{u,m,n}}}{L_{u,m,n}} \quad (5.20)$$

where the distance between the image source $S_{m,n}$ and image receiver R_u can be obtained by,

$$L_{u,m,n} = L(S_{m,n} | R_u) = \sqrt{(x_m - x_r)^2 + y_u^2 + (z_n - z_r)^2} \quad (5.21)$$

and the $Q_{u,m,n}$ is given by,

$$Q_{u,m,n} = Q_u \times Q_m \times Q_n \quad (5.22)$$

where Q_u , Q_m and Q_n are defined at Eq. (5.6).

By referring for consideration Section 5.2.1.2, only part of image sources can reach the receiver when the receiver is located in main branch of the enclosure. The sound waves of the remaining image sources should go into the side branch. When the receiver is located in the side branch, similar consideration can be applied on the prediction but the connection established between image source and image receiver should pass through the anechoic surface. The x -coordinates of the two intercept points that are projected from the image anechoic surface are determined as

$$F_u = \frac{-(y_a + b)x_r}{y_b} \quad , \quad (5.23)$$

$$N_u = \frac{-y_a x_r}{y_b + b} \quad . \quad (5.24)$$

The visibility factors then can be set according to Eq. (5.23) and (5.24) where

$$V_{u,m} = \begin{cases} 1 & \text{if } F_u > x_m > N_u \\ 0 & \text{otherwise} \end{cases} \quad (5.25)$$

By combining Eq. (5.23), (5.24) and (5.25), it can be seen that only the image sources located between the F_u and N_u can reach the image receiver R_u . In other words, image sources located outside the range of F_u and N_u can not link to the receiver in anyway. The visibility factor in Eq. (5.20) becomes unnecessary. The Eq. (5.20) now can be rewritten as

$$P(\omega) = \frac{1}{4\pi} \sum_{u=1}^{\infty} \sum_{m=M_-(u)}^{M_+(u)} \sum_{n=-\infty}^{\infty} \frac{Q_{u,m,n} e^{ikL_{u,m,n}}}{L_{u,m,n}} \quad (5.26)$$

where $M_+(u)$ and $M_-(u)$ are the upper and lower limits of the range of the image sources that can establish a connection and pass through anechoic surface. The $M_+(u)$ and $M_-(u)$ can be obtained by dividing the F_u and N_u by the width of the main enclosure and gives,

$$M_-(u) = \frac{-y_a x_r}{a(y_b + b)} \quad (5.27)$$

$$M_+(u) = \frac{-(y_a + b)x_r}{ay_b} \quad (5.28)$$

5.2.2 Reverberation time in a long enclosure with a ‘‘T’’ intersection

5.2.2.1 Reverberation time of a straight long enclosure

Apart from the signal to noise ratio, reverberation time also plays an important role in the speech intelligibility. To determine the reverberation time, we should start from

measuring or predicting sound decay curve in receiver. For both measuring and predicting the sound decay curve, reference should be made to the arrival time of the direct wave or first arrival [102, 103]. Then, the initial time $t = 0$ should be set to the time of first arrival. The source switch on time becomes negative since it should be switched on earlier than the initial time and gives

$$t_s = -L_{0,0} / c \quad (5.29)$$

where $L_{0,0}$ can be determined by Eq. (5.3) and c is the speed of sound. According to Eq. (5.29), the arrival time of image source $S_{m,n}$ is determined by

$$t_{m,n} = (L_{m,n} - L_{0,0}) / c \quad (5.30)$$

Then the separation between the real source and image source $S_{m,n}$ is given by

$$d_{(t)} = \sqrt{(x_m - x_r)^2 + (z_n - z_r)^2} \quad (5.31)$$

Actually, there are more than one image sources arrival at time $t_{m,n}$. All image sources obtained the same source/image source separation as image source $S_{m,n}$ should arrival R_0 be at the same time. In order to simplify the calculation, it can be assumed that both source and receiver are located at the centre of the long enclosure,

i.e. $x_s = x_r = \frac{a}{2}$ and $z_s = z_r = \frac{h}{2}$. The Eq. (5.31) can be rewritten as

$$d_{(t)}^2 = (am)^2 + (hn)^2 \quad (5.32)$$

It can be seen that the separation between the real source and of all image sources $S_{m,n}$ which belong to

$$m \in [0, \pm d/a] \quad (5.33)$$

$$\text{and } n = \pm \frac{1}{h} \sqrt{d^2 - (am)^2} \quad (5.34)$$

are the same. Then, the transient energy from time $t = 0$ to $t = t_d$ can be determined

by,

$$P_{(t)} = \frac{1}{4\pi} \sum_{m=(-d/a)}^{d/a} \sum_{n=-\frac{1}{h}\sqrt{d^2-(am)^2}}^{\frac{1}{h}\sqrt{d^2-(am)^2}} \frac{Q_{m,n} e^{ikL_{m,n}}}{L_{m,n}} . \quad (5.35)$$

The arrive time t_d can be determined straightforwardly,

$$t_d = (L_{d/a,0} - L_{0,0}) / c . \quad (5.36)$$

The reverberation time of an enclosure can be represented by T_{60} , T_{30} and EDT. T_{60} is the time for the signal level to decay 60 dB after the source is terminated. T_{30} is the doubled decay time of the signal reduced from -5 to -35 dB. In some noisy environment, long enclosure being a typical example, the sound source may not reach 35 dB higher than the background noise. Early Decay time (EDT) is the other way to determine the reverberant time which focuses on the early part of the decay process. It can be obtained by taking the time from the sound energy decay from zero to -10 dB then multiplying by 6.

To determine the reverberation time, we should calculate the total sound energy received from time t to infinity after the source is turned off. The total sound energy can be obtained by summing up the contributions from image sources arrival on and

after time t . There is an alternate method available. The total sound energy arrival from time t to infinity can be deduced from subtracting the total steady-state sound energy by the energy arrival from initial time to time t and gives,

$$P_{(t)}^* = P(w) - P_{(t)} \quad . \quad (5.37)$$

Then, it can determine the energy decay by

$$L_{(t)} = P_{(t)}^* / P(w) \quad . \quad (5.38)$$

Now, the energy decay curve can be determined by Eqs. (5.36), (5.37) and (5.38).

According to the energy decay curve, T_{60} , T_{30} and EDT can be obtained respectively.

5.2.2.2 Reverberation time of the opposite end of the long enclosure

When the receiver is located at the opposite end of a long enclosure, the direct link between the real source and receiver still can be maintained. The theory developed in Section 5.2.2.1 can be directly applied here but the visibility factor which was developed in Section 5.2.1.2 should be included in the Eq. (5.35) since only part of image sources can reach the receiver. By combining Eq. (5.11) and (5.35), the transient energy of a receiver located in the opposite end of a long enclosure from time $t = 0$ to $t = t_d$ is given as

$$P_{(t)} = \frac{1}{4\pi} \sum_{m=(-d/a)}^{d/a} \sum_{n=\frac{1}{h}\sqrt{d^2-(am)^2}}^{\frac{1}{h}\sqrt{d^2-(am)^2}} V_m \frac{Q_{m,n} e^{ikL_{m,n}}}{L_{m,n}} \quad (5.39)$$

where V_m is determined by Eqs. (5.13) to (5.15). The total sound energy arrival from

time t to infinity and the sound decay curve can be obtained by Eqs. (5.37) and (5.38).

Then, reverberation time can be estimated accordingly.

With reference to the Eqs. (5.16) to (5.18), there are limited image sources that can reach the receiver. All image sources outside the range of M_+ and M_- are going into the side branch and are not able to be reflected back to the main enclosure except by reflecting from the ceiling and floor. By plotting the sound decay curve, it can be seen that the sound decay curve of the after junction area drops down much faster than for the receiver located in a similar location of a straight long enclosure. The reverberation time of the after junction region of a long enclosure with T-branch is shorter than in the co-related location of a straight long enclosure.

5.2.2.3 Reverberation time of the side branch

When the receiver is located in the side branch, there is no direct link that can be established between source and receiver. All theories developed in Section 5.2.2.1 can not be applied in this situation, so everything should start from zero. First, the initial time needs to be defined by finding out the shortest path between image sources and image receivers that can pass through the side branch opening. By referring to a previous study [104], the shortest wave path between the image sources and image

receivers which can pass through the side branch opening should lie 45° on the x -axes and the distance should be double the distance of the real source and receiver. By setting the initial time to zero, the arrive time of image source $S_{m,n}$ to image receiver R_u is given by

$$t_{u,m,n} = (L_{u,m,n} - 2L_{0,0}) / c \quad (5.40)$$

By taking the same assumption in section 5.2.2.1, both source and receiver are assumed to be located at the centre of the enclosure, then the distance between image receiver R_u and image sources $S_{m,n}$ is given by

$$d_{(t)}^2 = [y_a + b(u + 0.5)]^2 + (am)^2 + (hn)^2 \quad (5.41)$$

Then, all image receivers and image sources belong to

$$u \in [1, (d - y_a - 0.5b) / b] \quad , \quad (5.42)$$

$$m \in [1, \frac{1}{a} \sqrt{d^2 - \{y_a + b(u + 0.5)\}^2}] \quad (5.43)$$

and $n = \pm \frac{1}{h} \sqrt{d^2 - \{y_a + b(u + 0.5)\}^2 + (am)^2}$ (5.44)

are same. Then, the transient energy from time $t = 0$ to $t = t_d$ can be determined by,

$$P(t) = \frac{1}{4\pi} \sum_{u=1}^{(d-y_a-0.5b)/b} \sum_{m=1}^{\frac{1}{a} \sqrt{d^2 - \{y_a + b(u + 0.5)\}^2}} \sum_{n=\frac{1}{h} \sqrt{d^2 - \{y_a + b(u + 0.5)\}^2 + (am)^2}}^{\frac{1}{h} \sqrt{d^2 - \{y_a + b(u + 0.5)\}^2 + (am)^2}} V_{u,m} \frac{Q_{u,m,n} e^{ikL_{u,m,n}}}{L_{u,m,n}} \quad (5.45)$$

where V_m is given by

$$V_{u,m} = \begin{cases} 1 & \text{if } M_+(u) > m > M_-(u) \\ 0 & \text{otherwise} \end{cases} \quad (5.46)$$

The $M_+(u)$, $M_-(u)$, $Q_{u,m,n}$ and $L_{u,m,n}$ are given by Eq. (5.21), (5.22), (5.26) and

(5.27). The arrive time t_d can be calculated by

$$t_d = (L_{u,m,n} - 2L_{0,0}) / c \quad . \quad (5.47)$$

By Eqs. (5.37) and (5.38), the total sound energy arrival from time t to infinity and the sound decay curve can be obtained. Then, reverberation time can be estimated accordingly.

5.2.3 Sound field and reverberation time by incoherent model

Besides the coherent summation used in section 5.2.1 and 5.2.2, the incoherent model also provides reasonable prediction [47, 48]. The difference between the coherent and incoherent model is the phase relationship of each arrival wave. In the coherent model, it sums up all arrival waves with the phase relationship while the incoherent model does not. For the receiver located at the same end of the main long enclosure, the total sound field p obtained by incoherent model is given by

$$p = P_0 \sum_{m=-\infty}^{\infty} \sum_{n=-\infty}^{\infty} \frac{R_{m,n}}{L_{m,n}^2} \quad (5.48)$$

where P_0 is the free field sound field of 1 m away from the source, $L_{m,n}$ is the distance between receiver and image source $S_{m,n}$ and can be calculated by Eq, (5.3),

$R_{m,n}$ is the combined reflection coefficient and can be obtained by.

$$R_{m,n} = R_m \times R_n \quad (5.49)$$

where R_x is defined as

$$R_x = (1 - \alpha_+)^{|x+g(x)|/2} (1 - \alpha_-)^{|x-g(x)|/2} \quad (5.50a)$$

and the functions $g(x)$ is given by

$$g(x) = \begin{cases} 1 & \text{if } x \text{ is an odd integer} \\ 0 & \text{if } x \text{ is an even integer} \end{cases} \quad (5.50b)$$

where α_+ is the absorption coefficient of the boundary surface located at the positive side of the x - z co-ordinate system and α_- is the absorption coefficient of the boundary surface located at $(0, 0, 0)$ of the x - y - z co-ordinate system. Then, the steady-state sound field of the receiver located at the opposite end of the main enclosure can be calculated by

$$P = P_0 \sum_{m=M_-}^{M_+} \sum_{n=-\infty}^{\infty} V_m \frac{R_{m,n}}{L_{m,n}^2} \quad (5.51)$$

where M_+ , M_- and V_m are given by Eqs. (5.16), (5.17) and (5.13) to (5.15).

Similarly, the sound field of the receiver located at the side branch is shown as

$$P = P_0 \sum_{u=1}^{\infty} \sum_{m=M_-(u)}^{M_+(u)} \sum_{n=-\infty}^{\infty} \frac{R_{u,m,n}}{L_{u,m,n}^2} \quad (5.52)$$

where $M_+(u)$ and $M_-(u)$ are shown in Eqs (5.27) and (5.28).

On the other hand, the incoherent model also can be used to calculate the transient energy from time $t = 0$ to $t = t_d$. When both source and receiver are located at the same end of the main enclosure, the transient energy obtained at the receiver is given by

$$P_{(t)} = P_0 \sum_{m=(-d/a)}^{d/a} \frac{1}{h} \sqrt{d^2 - (am)^2} \sum_{n=-\frac{1}{h} \sqrt{d^2 - (am)^2}}^{\frac{1}{h} \sqrt{d^2 - (am)^2}} \frac{R_{m,n}}{L_{m,n}^2} \quad (5.53)$$

and the energy decay curve can be determined according to Eqs. (5.36), (5.37) and (5.38). Similarly, when the receiver is located at the opposite end of the main enclosure, the transient energy can be calculated by

$$P_{(t)} = P_0 \sum_{m=(-d/a)}^{d/a} \frac{1}{h} \sqrt{d^2 - (am)^2} \sum_{n=-\frac{1}{h} \sqrt{d^2 - (am)^2}}^{\frac{1}{h} \sqrt{d^2 - (am)^2}} V_m \frac{R_{m,n}}{L_{m,n}^2} \quad (5.54)$$

When the receiver is located at the side arm, the transient energy from time $t = 0$ to $t = t_d$ is given by

$$P_{(t)} = P_0 \sum_{u=1}^{(d-y_a-0.5b)/b} \sum_{m=1}^{\frac{1}{a} \sqrt{d^2 - [y_a + b(u+0.5)]^2}} \sum_{n=-\frac{1}{h} \sqrt{d^2 - [y_a + b(u+0.5)]^2 + (am)^2}}^{\frac{1}{h} \sqrt{d^2 - [y_a + b(u+0.5)]^2 + (am)^2}} V_{u,m} \frac{R_{u,m,n}}{L_{u,m,n}^2} \quad (5.55)$$

and the time t_d can be obtained by Eq. (5.47).

5.3 Experimental validations

In order to validate the proposed theories, field measurements were conducted in a model tunnel and in a corridor both with a T-branch.

5.3.1 Model tunnel with T-branch

A model tunnel with a T-branch was built for experimental measurements in the current study. The model was built with varnished plywood boards 20 mm in thickness and placed in an anechoic chamber. The model was 0.58 m wide, 0.61 m in

height and 5.4 m long. The T-branch opening was located at the left vertical boundary and the distance between the side branch opening and the source was chosen as 2.5 m. The cross-section area of the T-branch was the same as the main tunnel and the T-branch had a length of 3.0 m.

A Tannoy driver fitted with a 25 mm-diameter brass tube was used as a point source in the experiment. The brass tube was 1 m long and used to minimise the reflection of sound from the Tannoy driver. A Brüel and Kjær type 4189 ½” free field microphone was employed as the receiver. A computer-based maximum length sequence system analyser (MLSSA) was used as both signal generator and data logger [89]. MLSSA was also employed as a data analyser and provides the detail of measured SPLs and reverberation times which are displayed in the following comparisons. Actually, similar measuring method was used is Chapter 2.3.1.

The acoustic impedance of the plywood board was determined in the anechoic chamber before the model was built. During the determination, a point source and a receiver were placed 0.1 m above the boundary surface and separated at a distance of 1 m. The excess attenuation (EA) spectrum of the boundary surface is obtained from deducing the measured spectrum by the free field measurement at 1 m distance.

Actually, the acoustic impedance of the hardwood board cannot be measured in this way directly or indirectly but it can use Attenborough's two-parameter model [89] to simulate that. According to Attenborough's model, the normalised surface impedance is calculated by

$$Z = 0.538\sqrt{\sigma_e / f} + i[0.538\sqrt{\sigma_e / f} + 19.74\alpha_e / f] \quad (5.56)$$

where f is the frequency of the acoustic excitation, σ_e is the effective flow resistivity and α_e is the effective rate of change of porosity with depth. Both parameters, σ_e and α_e were deduced by the best match between the predicted and measured excess attenuation spectrum. Figures 5.7 displays the typical measured EA spectrum compared with theoretical predictions where the impedance is calculated by the Eq. (5.56). The best-fit parametric values for σ_e and α_e were 200,000 kPa s m⁻² and 50 m⁻¹ respectively. Furthermore, the one-third octave band absorption coefficients (α) normally required for the incoherent model prediction also can be deduced from the normalised surface impedance and they are given by [54]

$$\alpha = \left| \frac{Z-1}{Z+1} \right|^2 \quad (5.57)$$

The calculated absorption coefficients of the plywood board from 500 Hz to 8000 Hz in one-third octave bands are listed in Table 5.2.

Figure 5.8 shows the comparison of predicted narrow-band excess attenuation

spectrum with the field measurement. The predicted excess attenuation spectrums are calculated by the coherent image source model. The EA shown in all figures are a reference to the noise level measured at 1 m free field from the source. The source was fixed in one end of the main enclosure, 0.29 m away from both sidewalls and 0.295 m above the ground. The receiver was moving around in the centreline of both the main enclosure and T-branch. The height of the receiver was the same as the source. In Fig. 5.8a, both source and receiver were located in the same arm of the main enclosure and separated by 1 m. Figure 5.8b displays the excess attenuation while source and receiver are separated by the T-branch junction and in 4 m separation. Figure 5.8c demonstrates the measured EA when the receiver is located in the T-branch and 1.5 m away from the centre of the junction. The receiver locations are designed according to the three legs of a long enclosure with a T-intersection.

With reference to the figure 5.8, it can be seen that the fluctuation of the experimental data in three receiver locations are more than the numerical predictions. The difference between the experimental data and numerical prediction is caused from the locations of the source and receiver. While designing the experiment, both source and receiver are assumed to be place on the centreline of the enclosure. This setup can help to minimise the path difference between the reflections from both vertical

boundaries and minimise the fluctuation of the measured data. Unfortunately, the model T-branch tunnel is so small, both source and receiver cannot be placed exactly on the centreline. The fluctuation of the experimental data is much more than the predictions. Besides the amplitude of the fluctuation, it can be seen that the numerical predictions agree tolerably well with the experimental data. The interference patterns match reasonable well in all three receiver locations. Compared with the three set measurements, the high frequency prediction of the receiver located at the T-branch is relatively poorer than the others. This is caused from the diffraction at the edges of the T-junction.

Apart from the narrow analysis shown in figure 5.8, octave-band analyses are also useful, easy to understand and much used for comparison. The narrow-band EA spectrum can be converted to octave band by [104]

$$\Delta EA = \left[\sum_i p_i^2 \times 10^{|EA_i|/10} \right] / \left[\sum_i p_i^2 \right] \quad (5.58)$$

where ΔEA is the relative excess attenuation converted from narrow band spectrum, i is the narrow band frequency within the octave band, p is the narrow band free field sound pressure.

Figure 5.9 shows the converted ΔEA spectrum for both experimental and predicted

results. It also compares them with the prediction results of incoherent model described in Section 5.2.3. It demonstrates that, first, the difference between numerical prediction and experimental data is much easier to identify by octave band rather than the narrow band. Second, the numerical predictions according to coherent image source model provide generally good agreement to the experimental data. Both curves show similar interference patterns and comparable magnitude. Furthermore, the coherent model's predictions provide better agreement than the incoherent model, especially in the high frequency range. Third, predictions according to the incoherent model are generally smooth curves and the predicted EA decreased as the source frequency increased. The magnitude fluctuation due to phase interferences cannot be displayed in the predictions. Besides the magnitude fluctuation due to phase interfaces, the predicted EA of the incoherent model is smaller than the experiment data and the predictions of coherent model generally. However, the predictions of incoherent model consistent with the general trend of the experimental data. On average, the incoherent model's predictions are 1 to 3 dB smaller than the predictions of the coherent model in different cases.

Besides the excess attenuation, reverberation time is also important in acoustic study since reverberation time is one of the key elements in clarity of hearing and sound

transmission index (STI). Figure 5.10 displays the measured EDT in three receiver locations. Figure 5.10 also displays the numerical predictions according to coherent and incoherent image source model. It notes that the prediction results obtained from the coherent image model provides similar interference patterns and comparable magnitude to experimental data. The predictions of incoherent image source model only laid on the general trend of the experimental data. Apart from the interference patterns, both coherent and incoherent image models can reasonable estimate the EDT it obtained from the experiment.

5.3.2 Field measurement

A full scale field measurement was carried out in a corridor with a T-branch. The width and the height of the corridor were 2.37 m and 2.5 m respectively. The width and height of the T-branch were the same as the main corridor. The length of the main corridor was 28 m and the T-branch was longer than 15 m. The floor of the main corridor was covered with a hard concrete surface. The walls were constructed with bricks furnished with a smooth layer of plaster covered with paint. The ceiling was constructed with 600 mm x 600 mm gypsum boards. The materials used to construct the T-branch were the same as the main corridor. In the current study, the floor and ceiling of the main corridor and T-branch were treated effectively as flat and smooth

surfaces. The acoustic impedances of the ceiling, ground surface and vertical boundaries were obtained by the same way described in Section 5.3.1. The detail is not shown here again but the effective flow resistivity and effective rate of change of porosity with depth of all boundary surfaces are listed in Table 5.1. The calculated absorption coefficients of all surfaces in one-third octave bands are listed in Table 5.2.

The same set of measuring equipments mentioned in Section 5.3.1 was employed for the current measurement except for the sound source. A Brüel and Kjær omni-directional speaker type 4296 was used as a point source. The source was fixed in the same location during the experiments. It was mounted at the centre of the main corridor, 1.37 m above the ground and 10 m away from the centre of the T-junction. There are three receiver locations displayed in the coming figures, the first one was located in the same arm of the source and 5 m away from the source, the second one was located in the opposite end of the main corridor and 15 m away from the source, and the third one was located in the T-branch and 5 m away from the centre of the T-junction. The height of the receiver was the same as the source. Receiver locations were designed to be similar with the measurements conducted in the model tunnel with a T-intersection.

Figure 5.11 shows the measured EA compared with the predictions of the coherent image source model. Although the fluctuation of measured data is larger than the prediction, the predictions still generally agreed with measurements. The interference patterns of the experimental data are also similar to the predicted results. The coherent image source model is believed to be accurate enough to approximate the sound fields in a long enclosure with a T-intersection. Again, the narrow band predictions of the coherent model are converted to wideband and compared with the predictions of incoherent model and experimental data. As shown in figure 5.12, the prediction of coherent model agreed well with experimental data. The predicted EAs of the incoherent model are generally smaller than the experiment data and the predictions of the coherent model. On average, the incoherent model's predictions are 0.5 to 2 dB smaller than the predictions of the coherent model.

Figure 5.13 displays the EDT predictions of coherent and incoherent models. It also shows the measured EDT in three receiver locations. It can be seen that the predictions of the coherent model match with the experimental data and provide better agreement than the predictions of the incoherent model. However, the “averaged error” of the two theoretical models is similar.

5.4 Summaries

For safety concern, speech intelligibility is a key issue when constructing long enclosures. In the current study, systematic formulation for predicting the sound fields and reverberation times in a long enclosure with a T-intersection is developed. The formulation is based on the coherent image source method. By using the developed formulation, it can estimate the excess attenuation and reverberation time when source and receiver are located in a regular long enclosure, in a long enclosure but separated by a T-branch opening, and the receiver is located in a T-branch but the source is still maintain in the main enclosure.

The proposed theory is verified by two field measurements, one in an indoor model and the other one in a real application. The prediction result of the incoherent model is also displayed in the comparison. It can be seen that the prediction according to coherent image model agreed generally well with the experimental data. The formulae developed in the current study can be applied in real applications. On the other hand, the estimations of incoherent model can consistent with the general trend of the measured excess attenuations but laid on the general trend of the reverberation times. The averaged difference between the predictions of the coherent and incoherent models are 0.5 dB to 3 dB in two case studies. The difference of two reverberation time

prediction models is not much on average.

Tables

	$\sigma_e / \text{kPa s m}^{-2}$	α_e / m^{-1}
Plywood board used in model T-branch Tunnel	200,000	50
Ceiling of corridor	8	1
Floor of corridor	20,000	450
Sidewall of corridor	500,000	450

Table 5.1: The best fit parametric values of the effective flow resistivity (σ_e) and the effective rate of change of porosity with depth (α_e) of the boundary surfaces used in in-house and outdoor experiments.

Frequency (Hz)	400	500	630	800	1000	1250	1600
Absorption coefficient Of hard plywood	0.016	0.018	0.02	0.023	0.026	0.029	0.032
Absorption coefficient of corridor's ceiling	0.49	0.463	0.432	0.401	0.37	0.34	0.31
Absorption coefficient of corridor's floor	0.023	0.026	0.030	0.033	0.046	0.038	0.042
Absorption coefficient of corridor's sidewall	0.008	0.009	0.01	0.011	0.013	0.014	0.016
Frequency (Hz)	2000	2500	3150	4000	5000	6300	8000
Absorption coefficient of hard plywood	0.036	0.04	0.045	0.051	0.057	0.063	0.071
Absorption coefficient of corridor's ceiling	0.28	0.26	0.236	0.21	0.193	0.174	0.156
Absorption coefficient of corridor's floor	0.048	0.054	0.068	0.076	0.086	0.096	0.108
Absorption coefficient of corridor's sidewall	0.018	0.020	0.023	0.026	0.029	0.032	0.036

Table 5.2: The estimated mean absorption coefficients of the boundary surfaces given in dB.

Figures

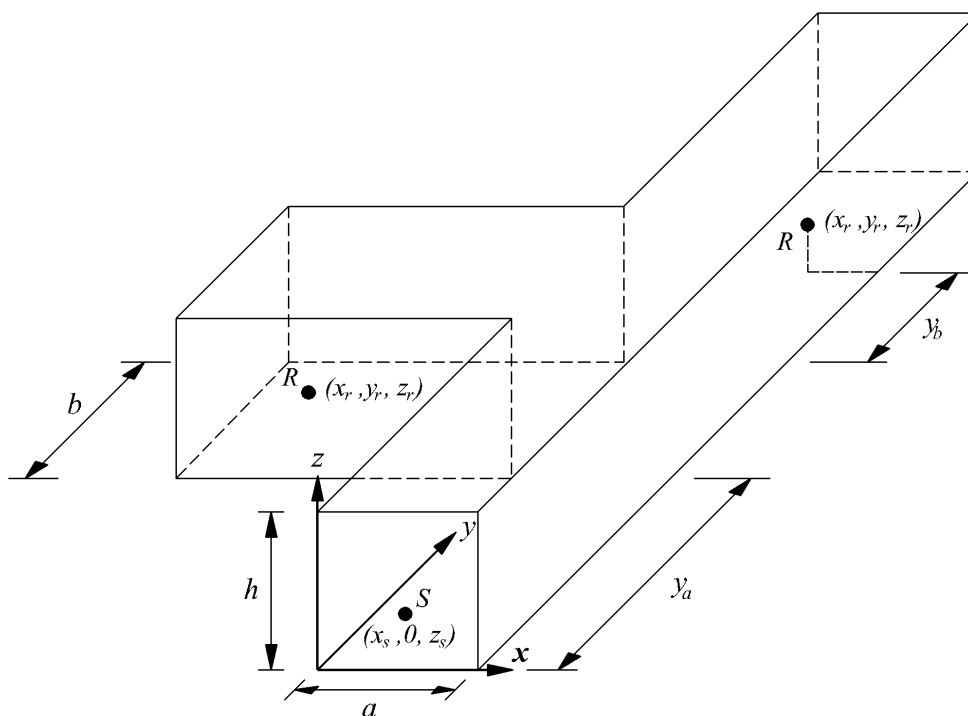


Fig. 5.1: Schematic diagram showing the rectangular coordinate system and the geometrical configuration of a long enclosure with a T-branch.

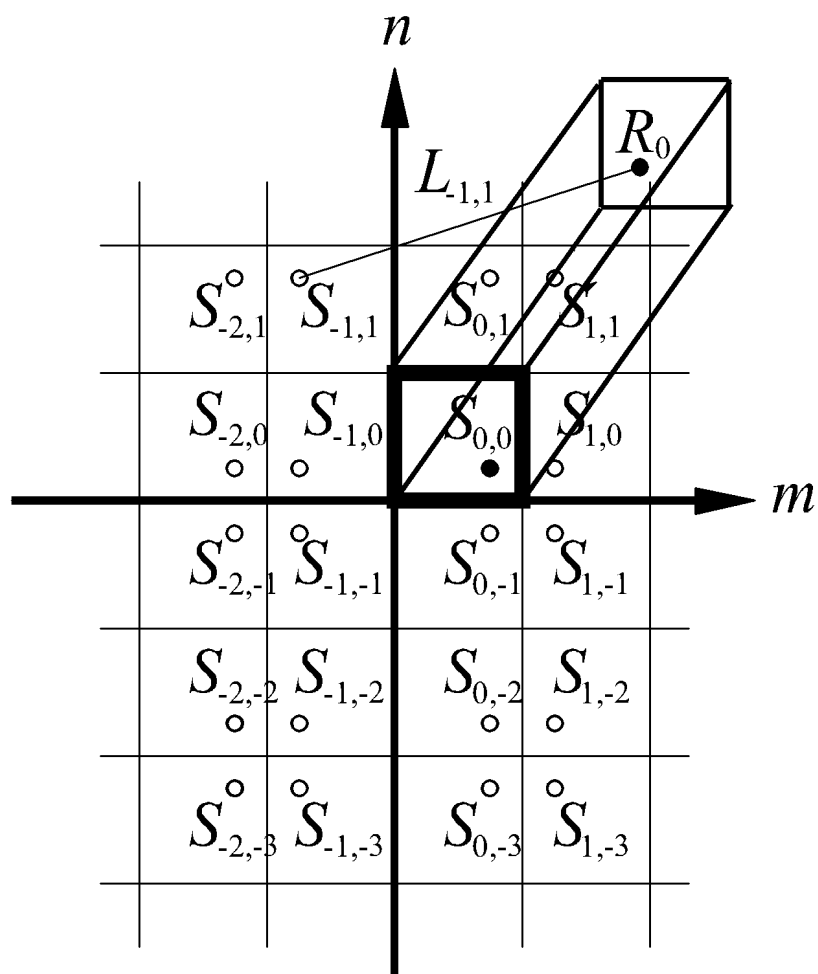


Fig. 5.2: Schematic shows the relative locations of the receiver, the real sound source (solid circle), image sources (open circle) and the corresponding distances of the receiver.

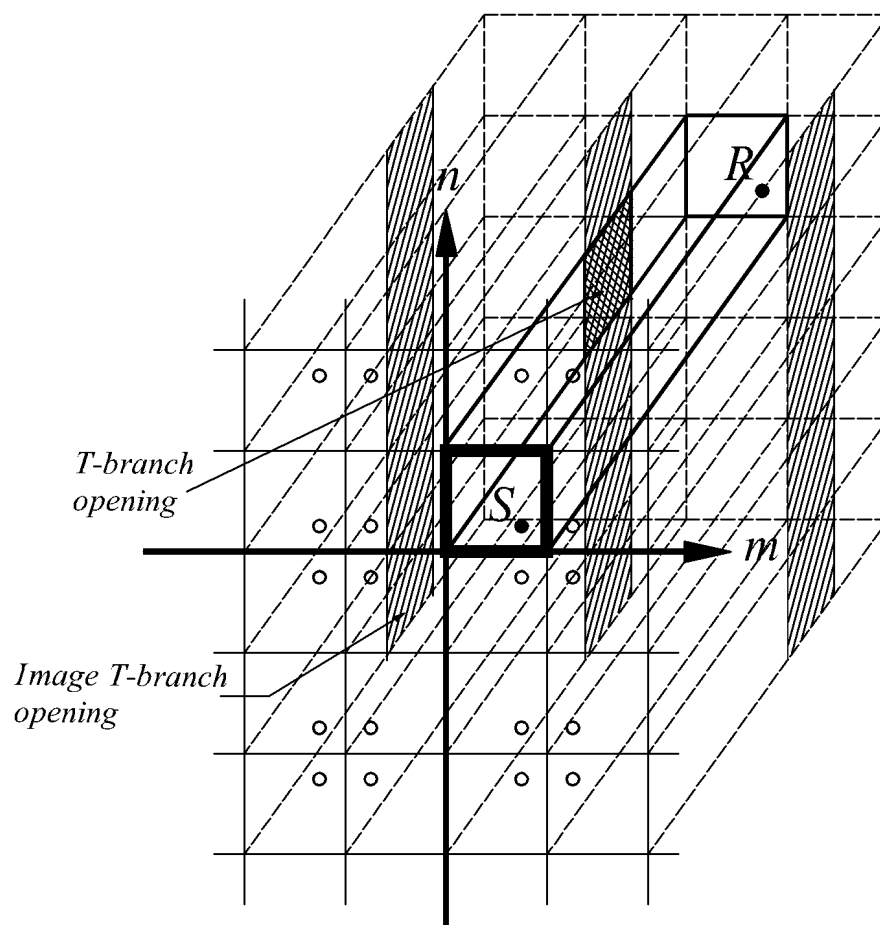


Fig. 5.3: Schematic diagram displays the locations of T-branch opening (in grid) and related image T-branch opening (in shadow).

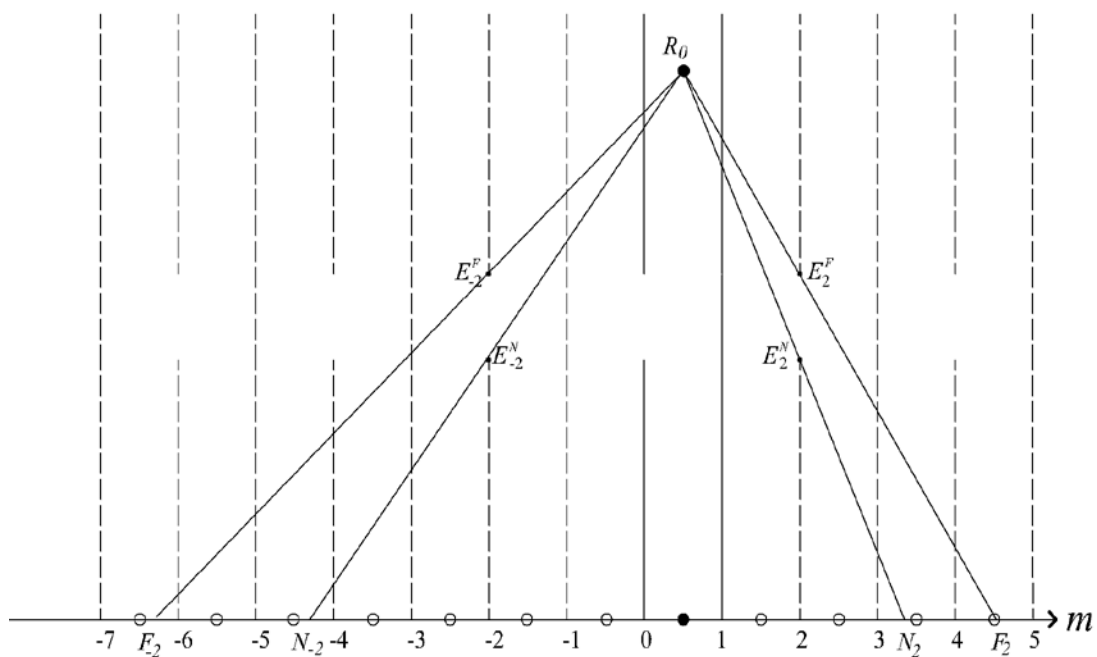


Fig. 5.4: Schematic diagram showing the simplified 2-D geometrical configuration of the main enclosure of a long enclosure with a T-branch. The solid lines are the vertical boundaries of the enclosure, the dash lines are the image boundaries and the junction of T-branch is represented by openings in the figure.

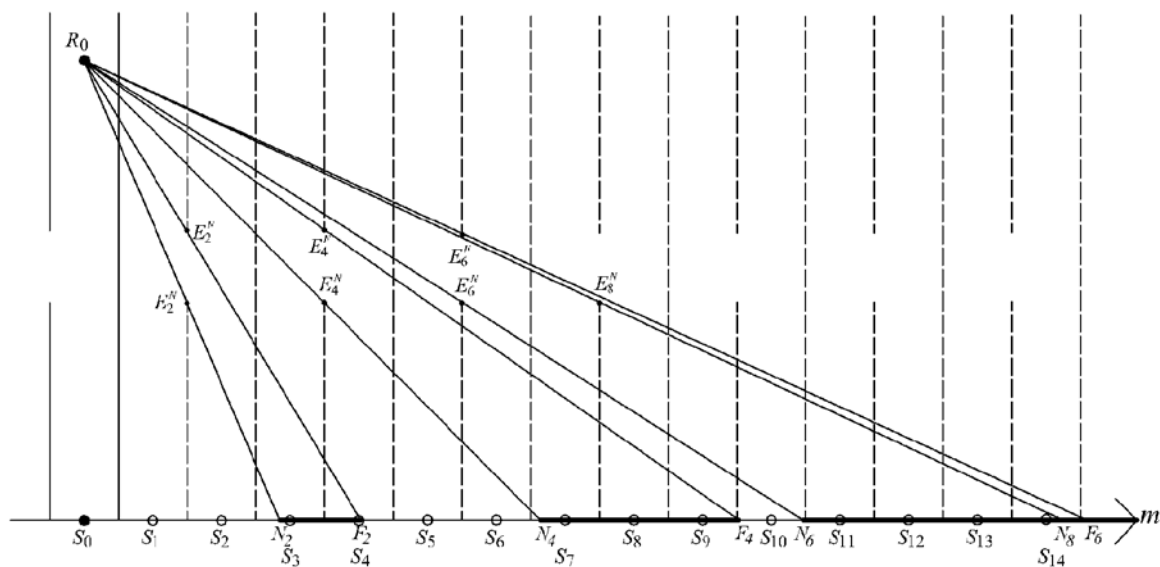


Fig. 5.5: Schematic diagram displays the image sources that will go into T-branch and cannot reach the receiver in simplified geometrical configuration (top view). The solid lines are the vertical boundaries of the enclosure, the dash lines are the image boundaries and the junction of T-branch is represented by openings in the figure. The real sound source and real receiver are represented by solid circles. Image sources are represented by open circles. The thick solid lines are the ranges of the image sources that cannot reach the receiver.

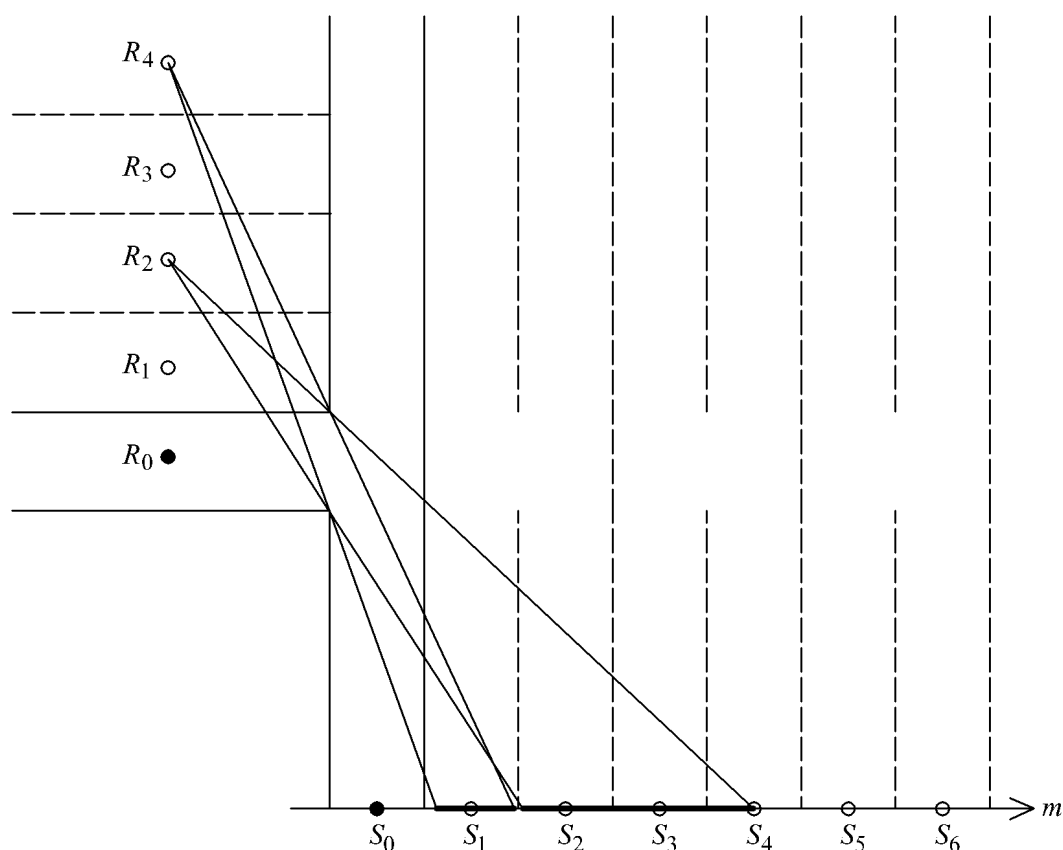


Fig. 5.6: Schematic diagram showing the geometrical configuration (top view) of a long enclosure with T-branch and related image boundaries. The solid lines are the vertical boundaries of the enclosure, the dash lines are the image boundaries and the openings are the images of junction of T-branch. The real sound source and real receiver are represented by solid circles. Image sources and image receivers are represented by open circles. The thick solid lines are the ranges of the image sources that can reach the image receivers.

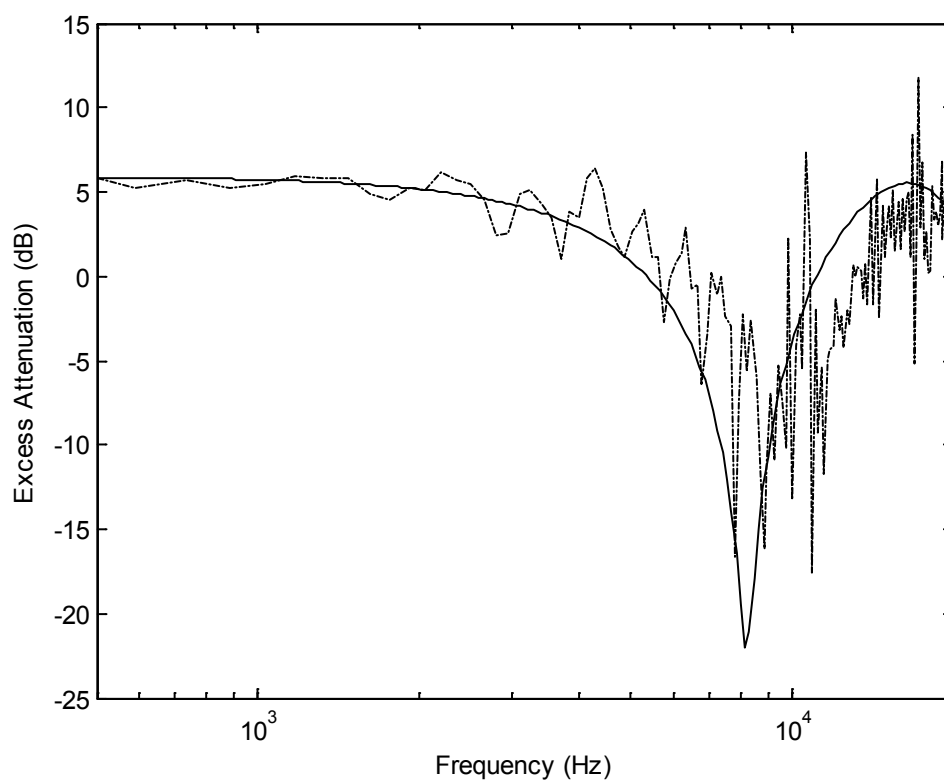


Fig. 5.7: The acoustic characterisation of the plywood board. The two-parameter model was used to characterise the surface impedances. The solid lines (—) are theoretical predictions where σ_e and α_e were 200,000 kPa s m⁻² and 50 m⁻¹ respectively and the dotted lines (-----) are experimental data.

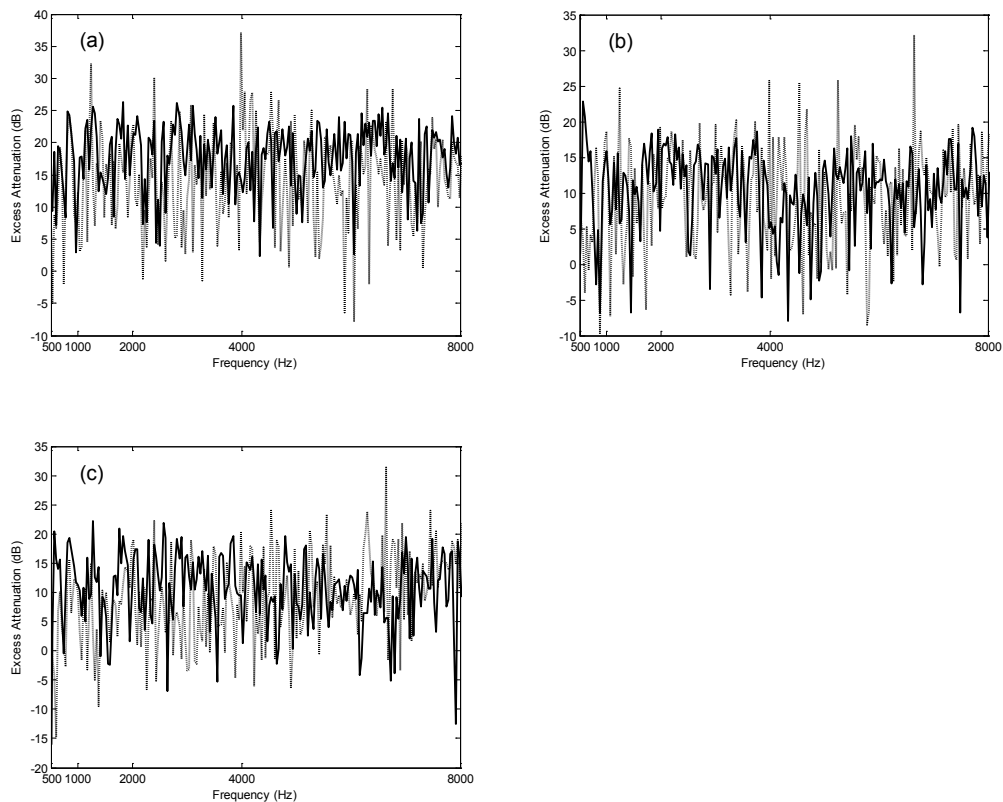


Fig. 5.8: Comparisons of measured EA with predicted excess attenuation by coherent image source method for different receiver locations in model tunnel with T-branch. The dotted lines are for experimental data and the solid lines are for predictions by the coherent image source method. In (a) and (b), both source and receiver were located in the main enclosure but receiver was located in the T-branch in (c). Details setup of the experiments is listed in Ch. 5.3.1.

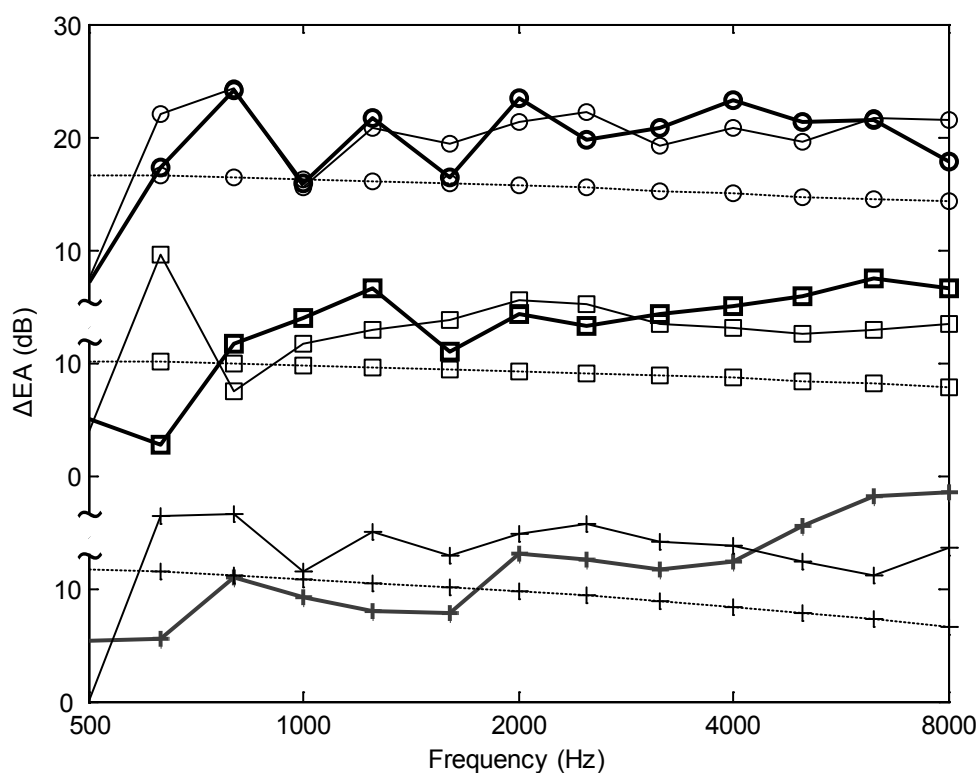


Fig. 5.9: The relative excess attenuation (ΔEA) is plotted versus frequency for various receiver locations in model tunnel with T-branch. The thick solid lines are for experimental data, the thin solid lines are for predictions by the coherent image source method and the dotted lines are for predictions by incoherent image source method.

The source and receiver locations are same as Fig. 5.8.

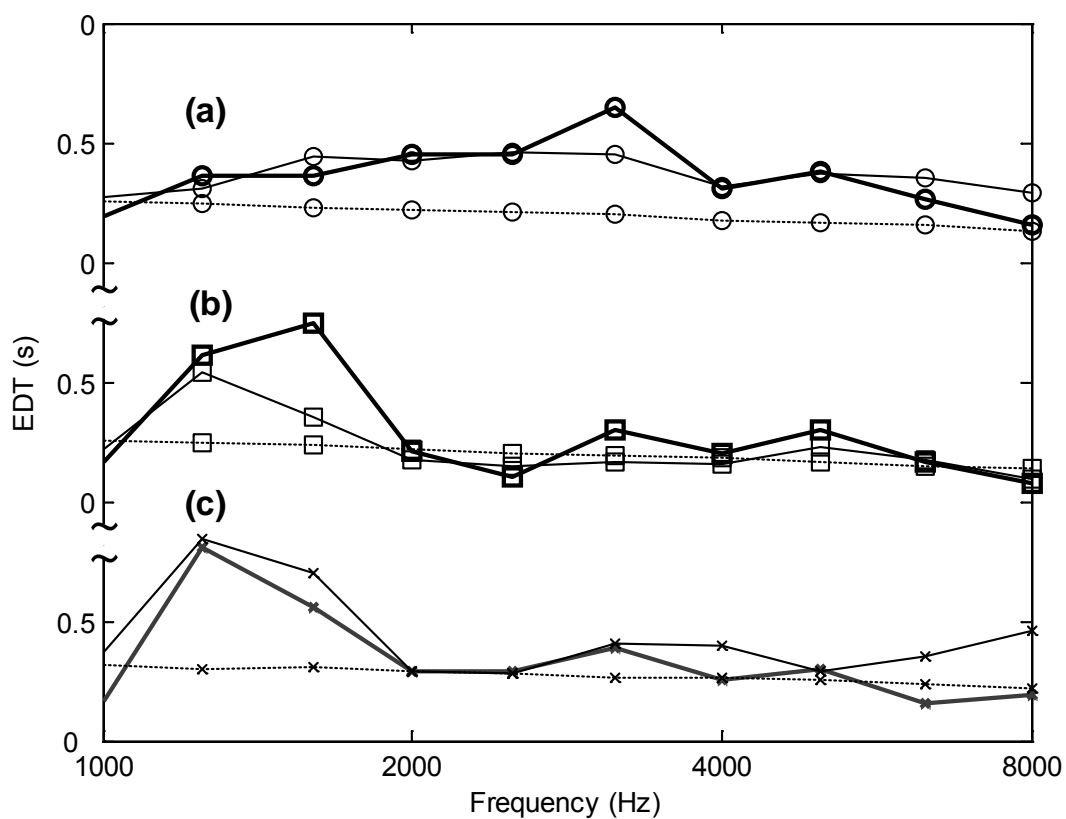


Fig. 5.10: The reverberation time, EDT, is plotted versus the source frequency in a model tunnel with T-branch. All source/receiver locations and the keys for the lines show in the figure are the same as in Fig. 5.9.

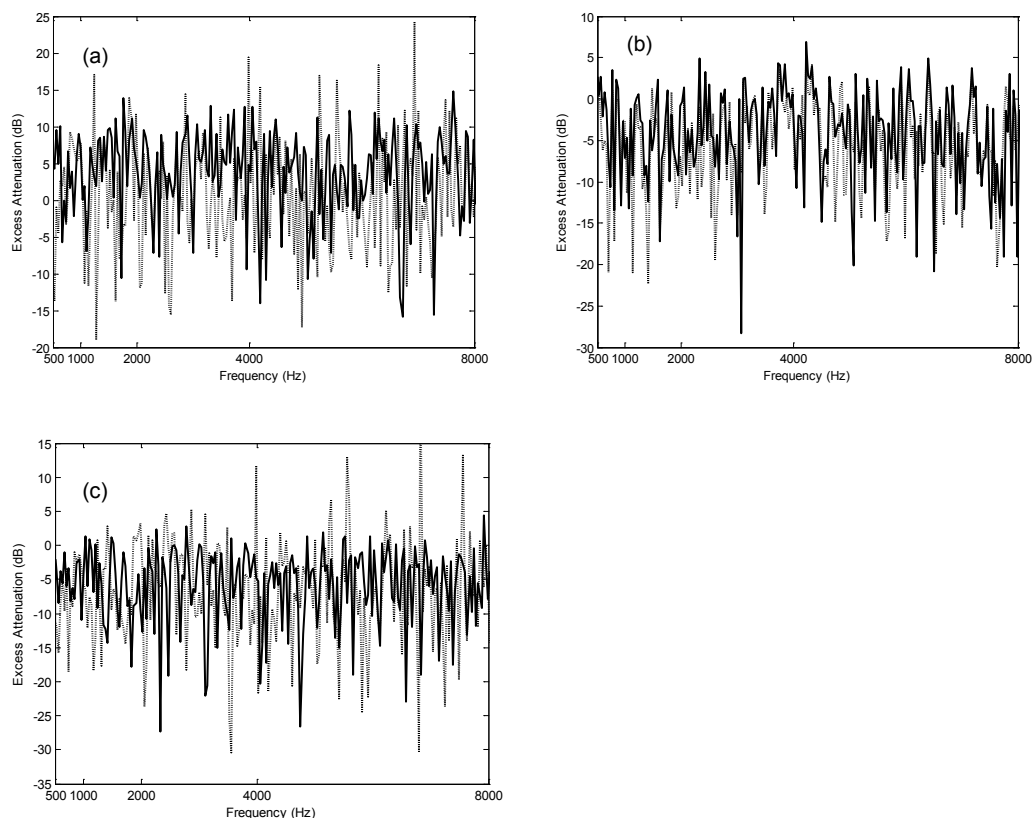


Fig. 5.11: Comparisons of measured and predicted narrow band excess attenuation in a corridor with T-branch. All keys for the lines show in the figure are the same as in Fig. 5.8. The source was fixed at the centre of one end of the main corridor. Receiver was located 5 m, Fig. 5.11(a), and 15 m, Fig. 5.11(b), away from the source. Fig. 5.11(c) shows the comparisons of the receiver located in T-branch and 5 m away from the centre of the junction. Details setup of the experiments is listed in Ch. 5.3.2.

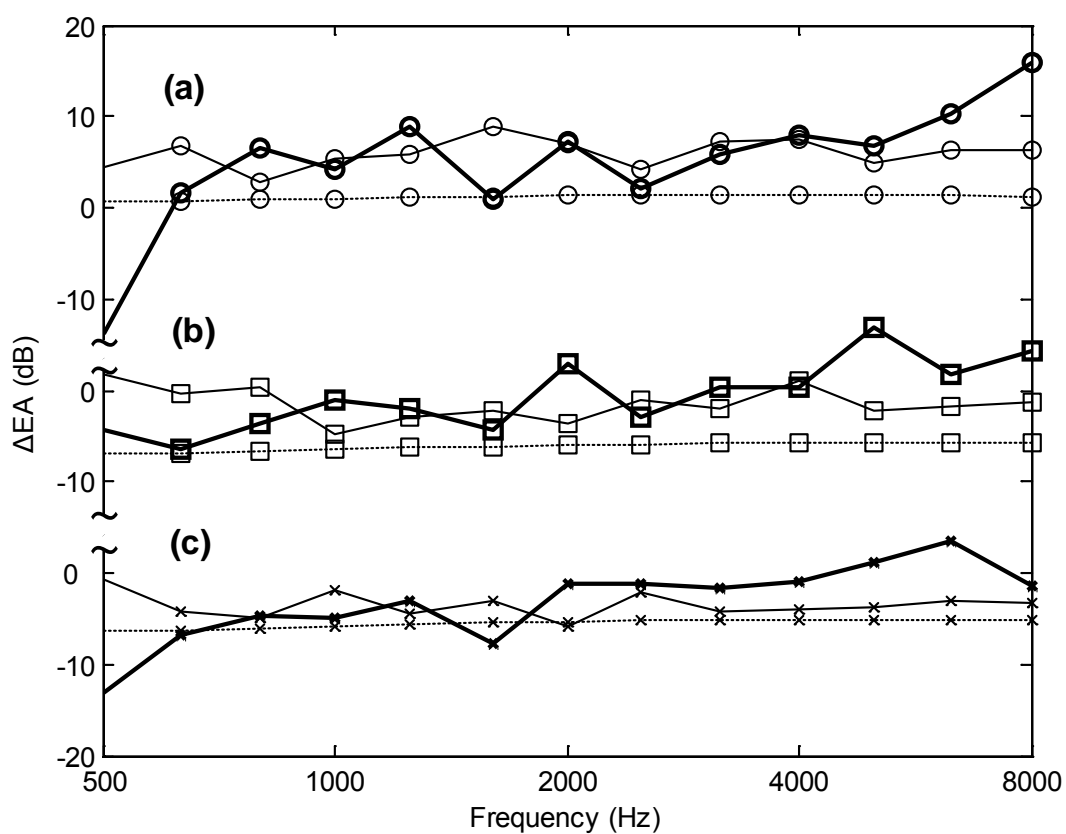


Fig. 5.12: The relative excess attenuation (ΔEA) is plotted versus frequency for receivers located in the corridor with T-branch. The source and receiver locations are the same as Fig. 5.11. The keys for the lines show in the figure are the same as in Fig. 5.9.

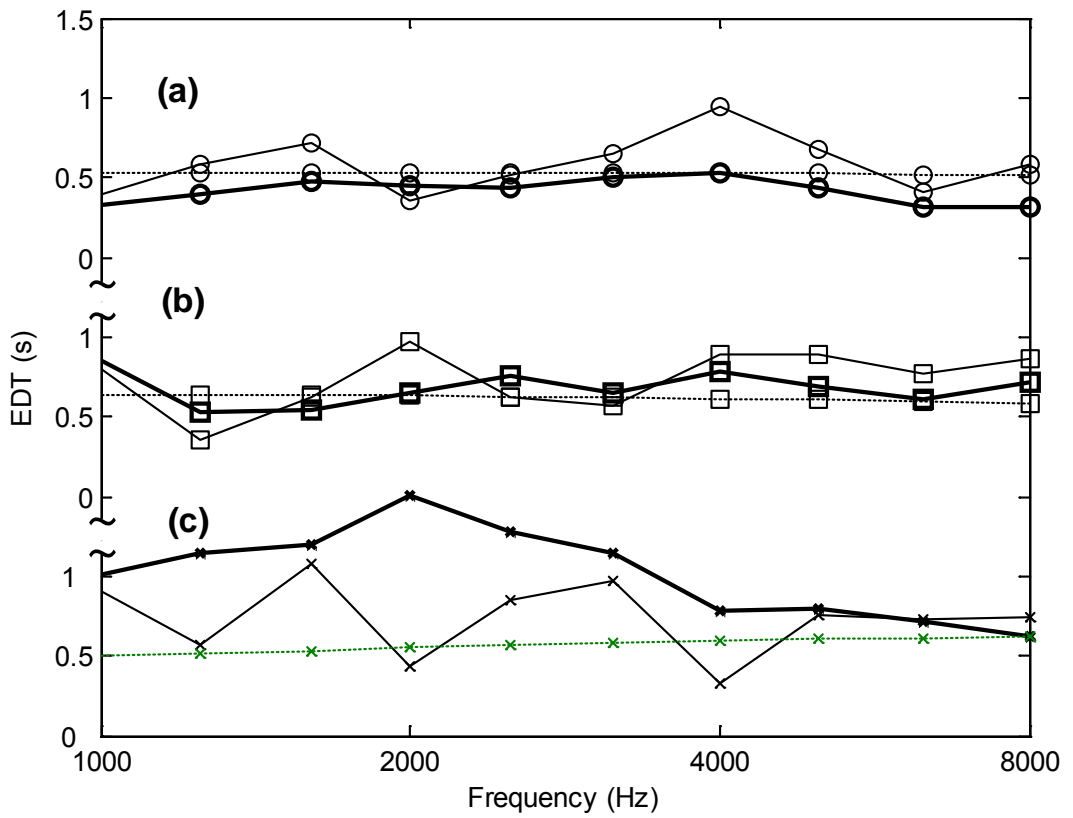


Fig. 5.13: The reverberation time, EDT, is plotted versus the source frequency in the corridor with T-branch. All source/receiver locations are the same as in Fig. 5.11 and the keys for the lines shown in the figure are the same as in Fig. 5.9.

Chapter 6

Constructing a dipole source

6.1 Introduction

Simple monopole is the most common sound source. However, many sound sources are directional and do not behave as a simple monopole. Dipole source is the next most important sound source besides the monopole. Many noise sources such as noise radiated from railway vehicles [66] and from ventilating fans [76] are best modelled as a dipole source. In previous studies, Hu and Bolton [105] used an un baffled loudspeaker as a dipole source in their experiments while Li *et al.* [106] have used piezoceramic disks as dipole sources to conduct impedance plane measurements.

In the current study, characteristics of dipole sound source are reviewed. The review is extended to focus on the dipole sources used in previous studies. The limitations of the available dipole sources are also mentioned. In order to prepare suitable dipole sources for the experimental measurements conducted in the next chapter, models for improving the performance of existing dipole sources are also studied. By using the

proposed model, both sound power output and directivity pattern of constructed dipole sources are improved.

6.2 Acoustic dipole

A dipole sound source is a pair of monopoles with equal acoustic power but in antiphase, separated by a small distance then coupled together. As shown in figure 6.1, the relative sound pressure levels (SPLs) of dipole source at $\theta = 90^0$ and 270^0 are zero since the two sources contribution at those points are equal and totally cancel each other out. However, with maximum magnitude on the axis, since the receiver is nearer to one source than the other, then the cancellation is reduced. The sound field of distance r and at an angle θ to the dipole axis is given by [65],

$$P_d(r, \theta, t) = \frac{\cos \theta}{4\pi} \left\{ \frac{1}{cr} \frac{\partial F}{\partial t} + \frac{F}{r^2} \right\} \quad (6.1)$$

where F is the dipole field strength. It can be seen that the dipole sound field is a variant that is based on two terms; one falls off with the inverse square of distance and the other is linear. The term with the inverse square dependence clearly dominates the field near source; it is termed 'near field'. The other falls off linearly as the distance is mainly dominant at far away distance; it is termed 'far field'. The difference between near field and far field behaviours of sources must always be borne in mind; one decreases inversely with the square of the distance but the other falls off linearly. In

the present study, the receiver is assumed to be far away from the source, so the near field characteristics are neglected in the study. All the directivity patterns presented in the current study are with the understanding that the data were taken from far field condition and the SPLs are decreasing linearly with distance increased.

In general, dipole source is a sound field constructed by two antiphase monopoles, provides maximum magnitude on axis and $\theta = 180^\circ$ but zero power radiates on 90° and 270° . The main difference between monopole and dipole is that the dipole has a near field characteristics but monopole does not.

6.3 Existing dipole sources

The diaphragm of an un baffled loudspeaker can be considered as a rigid circular piston in an infinite baffle [5, 108]. Lets consider the directivity pattern of a rigid circular piston in an infinite baffle. The directivity pattern of a rigid circular piston is dependent on the ka , where k is the wave number ($k=w/c$ or $2\pi/\lambda$, w is the angular frequency, c is the speed of sound, λ is the wave length) and a is the radius of the piston. Since the wave number k varies with frequency, the directivity pattern of a rigid circular piston varies with frequency also. At the low frequency band, $ka < 1$, the radiation of a rigid circular piston is almost independent of direction and the piston

behaves essentially like a monopole. When the frequency increases, the directivity pattern becomes narrow and highly directional after ka is greater than three. Assuming that the speaker diaphragm behaves as a rigid piston, the directivity characteristics of a speaker should be determined by the ratio of diaphragm diameter to wavelength of the emitted sound ($ka = 2\pi a/\lambda$). Decreasing the ratio of the diaphragm diameter to wavelength can improve the angle of radiation. The front and back sides of a vibrating diaphragm can be considered as two individual sound sources and two sources are radiated in anti-phase. At the low frequency band, both sources can be treated individually and non-directional. So, the un baffled loudspeaker is commonly described as a dipole. Hu and Bolton [105] used a “Radio Shack” 40-1289 as a dipole source in their study. The diaphragm diameter of 40-1289 was 7 cm and the usable frequency was between 1500 to 4500 Hz. The ka of the loudspeaker was between 1 to 3. However, Hu and Bolton found it necessary to include substantial monopole components when comparing their numerical predictions with measurements. Beauvilian *et al.* [107] used an “Infinity” RS 2000 un baffled loudspeaker as a dipole source (ka equal to 0.3) to conduct measurements. The one metre free field SPL of RS 2000 was 78 dB on 250 Hz pure tone.

Figure 6.2 shows the basic format of an un baffled loudspeaker. As shown on the figure,

the speaker diaphragm is suspended at front and rear by compliant suspension which allows the diaphragm to move on its axis. The diaphragm is called a “cone” in the speaker structure. Assuming that the diaphragm behaves as a rigid piston and is mass-controlled, the sound power output response is relies on two factors, ka and f_o . f_o is the principle resonant frequency of the speaker. The relationship of the sound power output and ka of an un baffled loudspeaker is displayed in figure 6.3. It can be seen that un baffled speaker can provide a flat frequency response when the ka is larger than 1. If ka is less than 1, the sound power output is decreased by 6 dB per octave and further rolls off to 18 dB per octave when the frequency fall down to below the principle resonant frequency. In principle, the directivity pattern of an un baffled loudspeaker can be improved by decreasing the operating ka . In the mean time, the sound power output of the loudspeaker also has been decreased. The acoustic power of the dipole source that is created by an un baffled loudspeaker should be less than the designed loudspeaker output power. The output power will be even less when the operating frequency is further reduced to improve the directivity. Worse still, the structure of the diaphragm front and back is assumed as two individual sources that vibrates in the anti-phase while the diaphragm structure is totally different in front and back parts. The directivity patterns radiated from two sides of a loudspeaker should not be fully symmetrical. Obtaining a perfect dipole sound source field from an

unbaffled loudspeaker is not an easy matter. Lucky, an unbaffled loudspeaker can perform as a perfect dipole, so its acoustic output power should be less than the designed value.

Apart from using unbaffled loudspeaker, Li *et al.* [106] used piezoceramic disks as dipole sources in their measurements. During anechoic chamber measurements, Li found that piezoceramic disks of the type used as ultrasonic transducer elements radiate as a dipole near their resonant frequencies with the main lobes normal to the disk faces. Two piezoceramic disks with measured resonance frequencies of 2915 and 4069 Hz were used in their experiments. The main limitation of using piezoceramic disk to conduct measurements is sound power output. As shown in Li *et al.*'s experiments [106], the free field SPLs provided by the piezoceramic disks were less than 30 dB. Furthermore, operating frequency range is the other limitation since piezoceramic dipole is functioned at a fixed frequency.

6.4 Dipole source constructed by two loudspeakers

By referring to figure 6.1, it can be seen that the radiation pattern of a dipole source can take the form often described as a “figure-of-eight” characteristic. The positive and negative signs indicate the relative phase or polarity of the sources, as well as the

relative phase of the sound radiation from front and back. By locating two non-directional sound sources close together but powered by anti-phase with equal amplitude, it can be described as a dipole source also.

The directivity pattern of a baffled loudspeaker or so called loudspeaker is non-directional at a low frequency band. By placing two loudspeakers together and powered by anti-phase, it is possible to construct a dipole sound source at a low frequency range. A loudspeaker radiation pattern measurement has been conducted in an anechoic chamber of internal dimensions of 6 x 6 x 4 m³ (high) to source a non-directional speaker. A Renkus-Heinz PN 61 self-powered loudspeaker was used as the source and a “B&K” 4189 pre-polarised free-field 1/2 in. condenser microphone was used as the receiver. “Renkus-Heinz” PN 81 is a two-ways active loudspeaker that equipped with a 175 w 8” low frequency driver, a 40 w 1” high frequency driver, a power amplifier and a crossover. A PC-based maximum length sequence system analyser (MLSSA) was used as both signal generator and data analyser of the measurements [90]. The MLSSA came with a special software module that can be used to measure the directivity patterns of loudspeakers directly. The anechoic chamber measurement result of the directivity pattern at 200 Hz is shown in figure 6.4(a). It can be seen that the directivity pattern of PN 81 at 200Hz is still not

fully non-directional. In practical terms, constructing a perfect non-directional monopole by a loudspeaker is possible in theory but difficult in practice.

During the study, a few speakers were been measured but the directivity patterns still were not good enough to perform as a perfect monopole. The possibility of constructing a dipole source by two non-perfect monopoles should be taken into consideration. Lets consider the directivity pattern of a loudspeaker in two parts; sound wave radiates from the front part and the back part. When two loudspeakers are setup close to each other and powered by anti-phase, sound power radiated on back part of one loudspeaker should be cancelled out by the other one. If the sound power radiating from the front part of the loudspeaker is larger than the back part, the interaction between the sound powers radiating from the back to the power radiating from the front of the other loudspeaker becomes less important. This is because the amount of sound power that can be cancelled out is less than the amount of the speaker radiated. The directivity pattern of the back part of the speaker becomes less important. With two loudspeakers with non-perfect monopole directivity it should be possible to construct a perfect dipole source.

Figure 6.4 displays the one-third octave band directivity patterns of the

“Renkus-Heinz” PN 81 self-powered loudspeaker at 200 Hz and 2 kHz. Figure 6.4(a) shows the directivity pattern at 200 Hz and figure 6.4(b) shows at 2 kHz. The front to back SPL differences are 13 dB at 200 Hz and 28 dB at 2 kHz. Figure 6.5 shows the one-third octave band directivity patterns of the dipole source which is constructed by two PN 81s. The same set MLSSA was used again. Since the size of the dipole was relatively large, the directivity patterns were measured 2 m away from the centre of the source rather than 1 m in normal directivity measurements. As shown in the figures, the directivity patterns of the dipole constructed by two PN 81s are reasonably good enough. The front-to-back SPL differences of the dipole source were 0.5 dB at 200 Hz and 0.1 dB at 2 kHz. The dipole also quite powerful; it provided up to 87 dB at 200 Hz and 107 dB at 2 kHz. The setup of the dipole source is shown in figure 6.6. Since PN 81 is a self-powered loudspeaker and the dimension of the speaker is much larger than un baffled loudspeaker, this is the main limitation of using this dipole in field experiments. The size of the dipole was 0.28 m in width, 0.5 m in height and 0.7 m in depth. It is suitable for large scale measurements such as measurements in traffic tunnels, pedestrian subways but it is too large for corridors. In order to construct a suitable dipole source for small scale measurements, the size of the dipole source must be reduced.

The directivity pattern of un baffled loudspeaker is dipole like but it is very difficult to obtain a perfect dipole shape. It was shown that with two non-perfect monopoles it is possible to construct a perfect dipole. It may be possible to construct a perfect dipole with two un baffled loudspeakers as well. When two un baffled loudspeakers are faced back to back and close to each other and then powered by anti-phase, the sound power radiated from the backside of the loudspeakers may be totally cancelled out by the other one. The sound fields radiated from the front part of two un baffled loudspeakers can be coupled together and performed as a dipole source.

Figure 6.7 shows the directivity patterns of 800 Hz and 1 kHz of a 20 w un baffled loudspeaker in one third octave band. Figure 6.7(a) is the directivity pattern of 800 Hz and figure 6.7(b) is 1 kHz. The speaker size was 4" (100 mm) and the diaphragm size was 94 mm (the ka approximately equal to 0.7 at 800 Hz and 0.87 at 1 kHz). As shown in the figures, the directivity patterns of the un baffled loudspeaker at 800 Hz and 1 kHz are similar to the dipole but totally non-perfect. After the setup of two un baffled loudspeakers together with a separation of 54 mm and power by anti-phase, the directivity patterns of both frequencies is must improved. See figure 6.8(a) and 6.8(b). The maximum 1 m free field sound pressure levels were 68 dB at 800 Hz and 67 dB at 1 kHz. The front-to-back SPL differences of this dipole at both frequencies

were 0.4 dB. The sound power output is the main limitation when applying this source for experimental measurements. It is limited to 68 dB at both frequencies.

In order to prepare a much powerful dipole source for experimental studies in the next chapter, the other dipole source was constructed by two 5.5" 50 w un baffled speakers. The diaphragm diameter of this dipole was 114 mm (the ka was 0.84). Figure 6.9 shows the directivity pattern of 800 Hz in the one third octave band. Compared with the dipole source constructed by two 4" un baffled loudspeakers, the new source provided up 80 dB at 800 Hz but the front-to-back SPL different was 0.6 dB. In order to minimise the front-to-back SPL difference of this dipole source, two loudspeakers were driven by two different signal levels. After adjusting the signal levels on two loudspeakers, the front-to-back SPL difference of this dipole was reduced to 0.1 dB. Figure 6.10 shows the directivity pattern of the dipole after adjusting the signal levels on two speakers. The dipole source setup arrangement is shown in figure 6.11.

6.5 Summaries

Both un baffled loudspeaker and piezoceramic disk were used as dipole sources by previous authors [105 - 107]. The limitations of using an un baffled loudspeaker include the sound power output, the directivity pattern and limited sound power output.

By using a piezoceramic disk, the directivity pattern of the created dipole source can be optimised and made nearly perfect but the sound power output is very limited. In the present study, dipole sources were constructed by two baffled or unbaffled loudspeakers where two speakers were located close to each other, faced back to back and powered by anti-phase.

Experiment results show that the directivity patterns of the dipole sources constructed by two speakers were close to a perfect dipole source. Compared with the dipole source that was constructed by a single unbaffled loudspeaker, the directivity patterns are greatly improved. Apart from the directivity pattern, the operation frequency range of the dipole source constructed by the proposed model is much higher than the dipole constructed by a single unbaffled loudspeaker. The dipole source constructed by two 5.5" unbaffled loudspeakers can work at 800 Hz one third octave band compared to only 250 Hz pure tone by a single 6" unbaffled loudspeaker in previous studies [107]. Furthermore, the sound power output of the dipole source constructed by two loudspeakers is much higher than in previous studies [105 - 107].

In general, all directivity patterns, operating frequency ranges and output power can be improved by constructing dipole from two loudspeakers. The proposed model is an

alternative to preparing a dipole source for experiments.

Figures

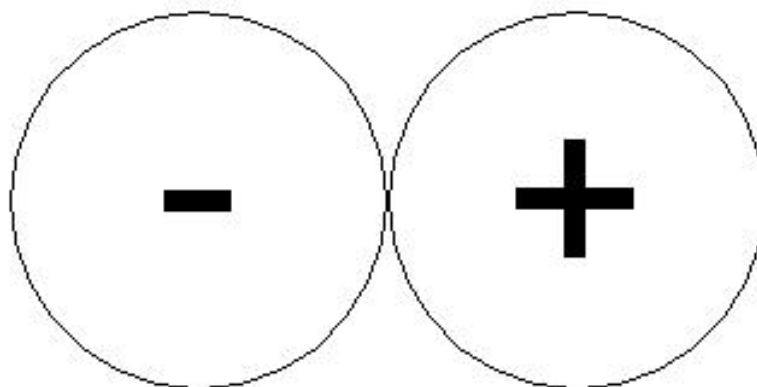


Fig. 6.1: The dipole sound field

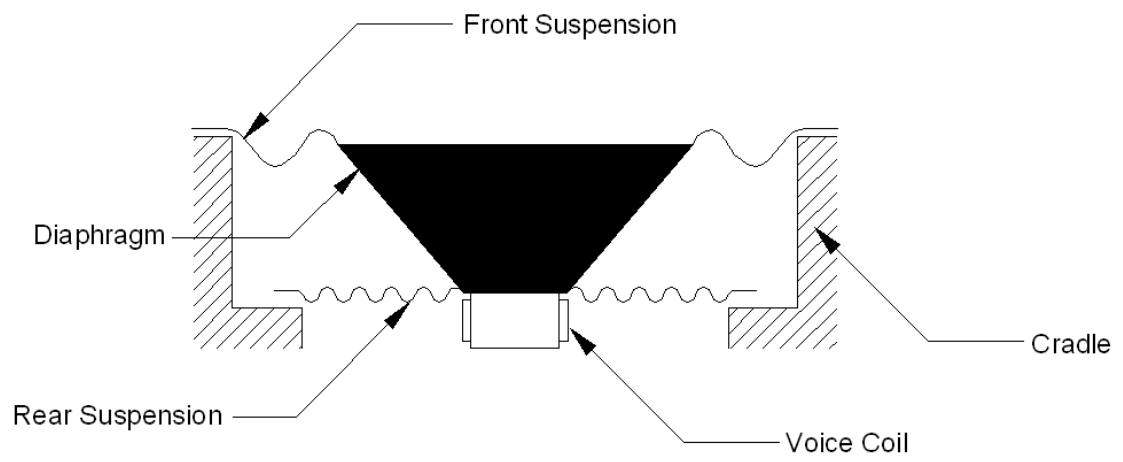


Fig. 6.2: The structural assembly of a loudspeaker.

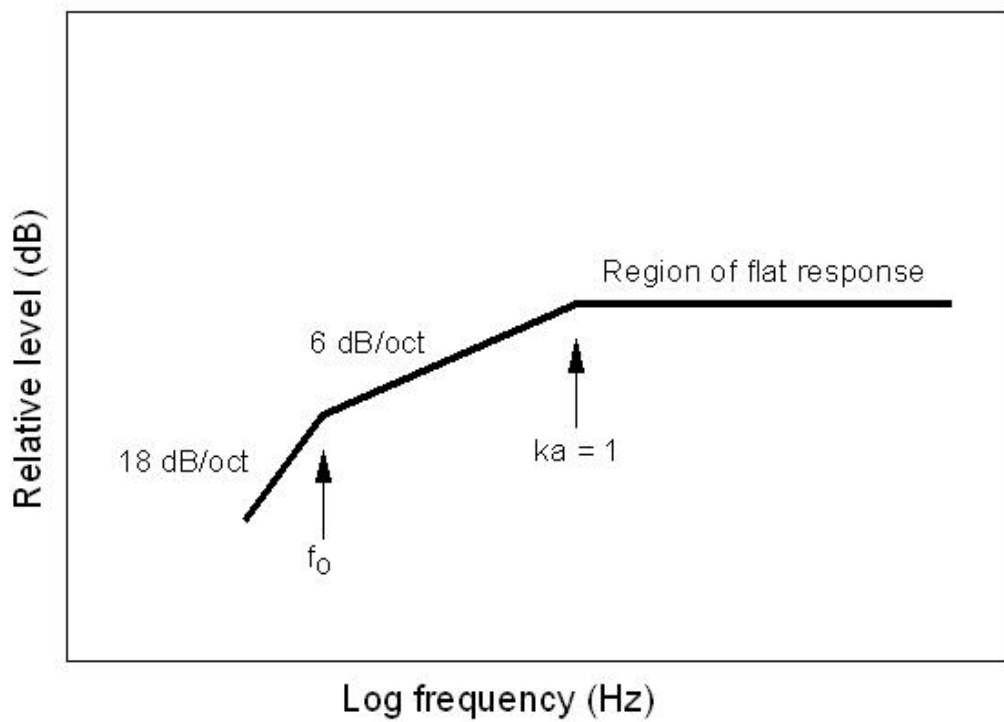


Fig. 6.3: The loudspeaker sound power output related to ka .

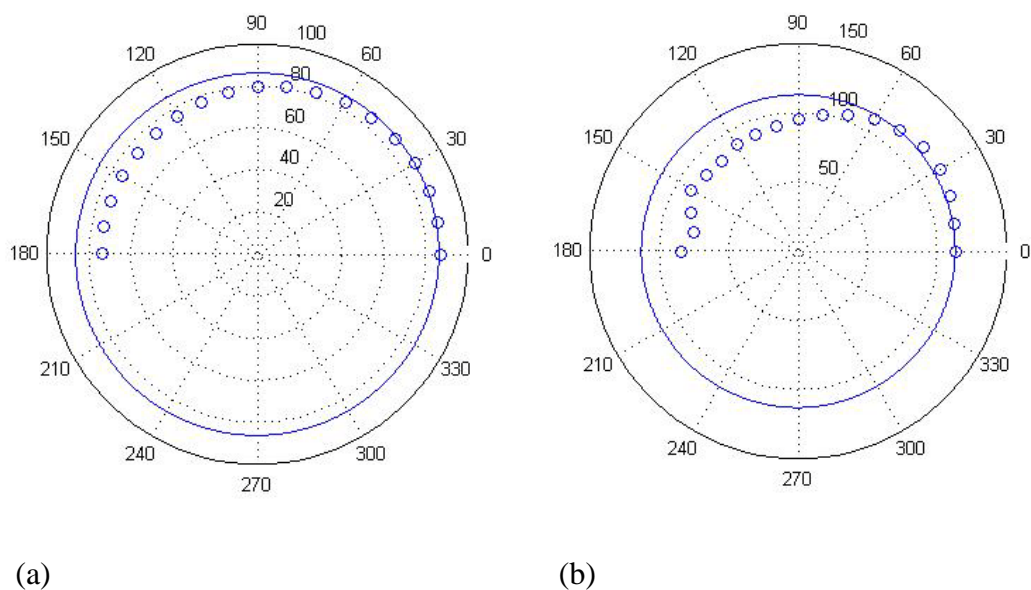


Fig. 6.4: The directivity patterns of a “Renkus-Heinz” PN 81 self-powered loudspeaker compare with a perfect monopole at (a) 200 Hz and (b) 2 kHz. The solid lines (-----) are the directivity pattern of a perfect monopole and the circles (O) are the measured directivity pattern of the PN 81.

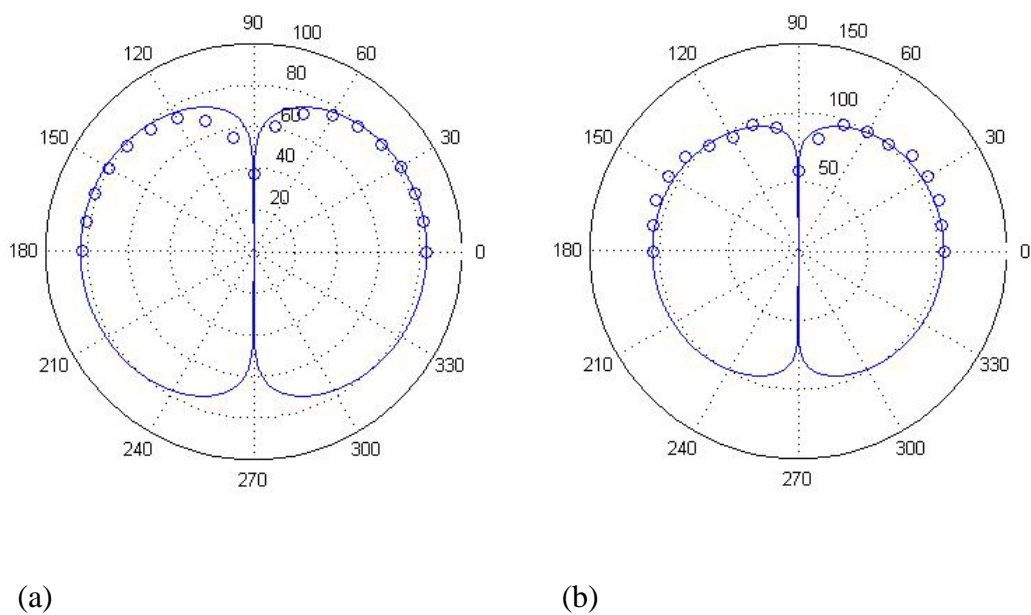


Fig. 6.5: The directivity patterns of the dipole source constructed by two out-of-phase “Renkus-Heinz” PN 81 self-powered loudspeakers compared with a perfect dipole at (a) 200 Hz and (b) 2 kHz. The solid lines (—) are the directivity pattern of a perfect dipole and the circles (O) are the measured directivity pattern of the dipole source constructed by two out-of-phase PN 81.



Fig. 6.6: The arrangement of the dipole source constructed by two “Renkus-Heinz” PN 81 self-powered loudspeakers.

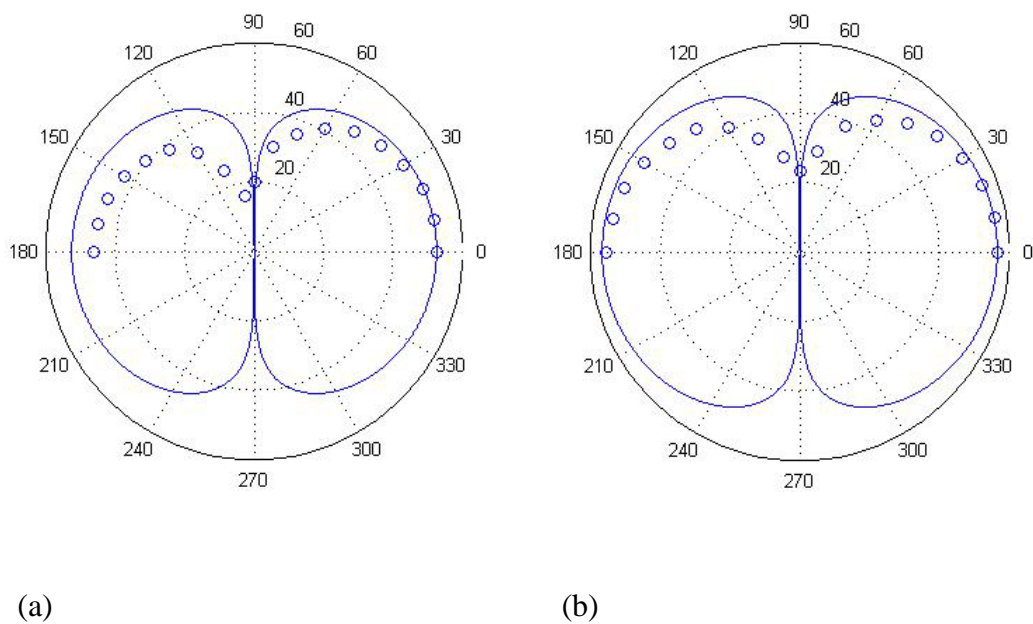


Fig. 6.7: The directivity patterns of a 4" unbaffled loudspeaker compared with a perfect dipole at (a) 800 Hz and (b) 1 kHz. The solid lines (-----) are the directivity pattern of a perfect dipole and the circles (O) are the measured directivity pattern of the 4" unbaffled loudspeaker.

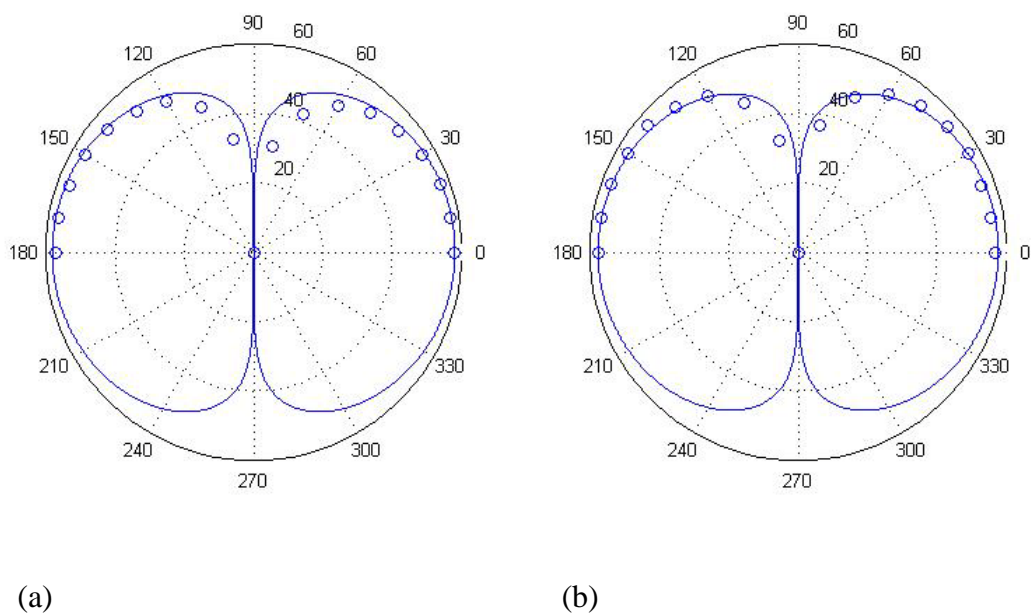


Fig. 6.8: The directivity patterns of the dipole source constructed by two out-of-phase 4” unbaffled loudspeakers compare with a perfect dipole at (a) 800 Hz and (b) 1 kHz.

The solid lines (-----) are the directivity pattern of a perfect dipole and the circles (O) are the measured directivity pattern of the dipole source constructed by two out-of-phase 4” unbaffled loudspeakers.

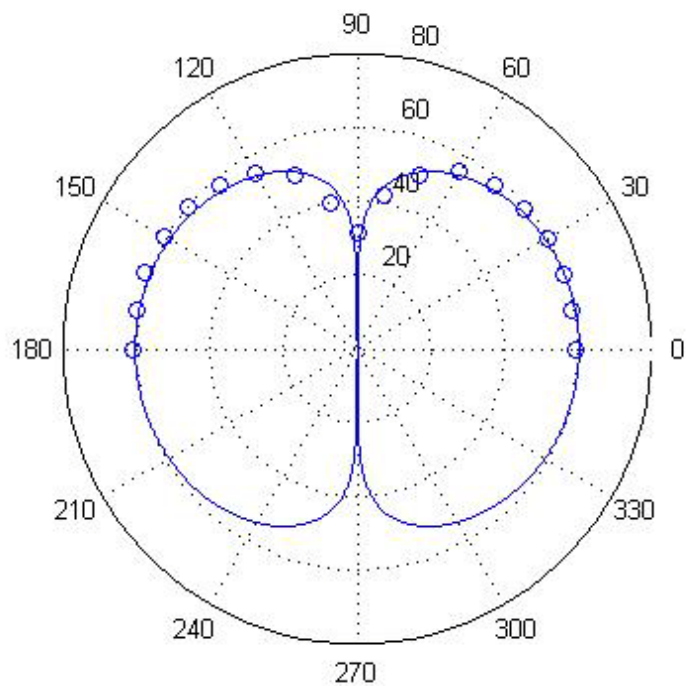


Fig. 6.9: The directivity patterns of the dipole source constructed by two out-of-phase 5.5" unbaffled loudspeakers compare with a perfect dipole at 800 Hz. The solid lines (-----) are the directivity pattern of a perfect dipole and the circles (O) are the measured directivity pattern of the dipole source constructed by two out-of-phase 5.5" unbaffled loudspeakers.

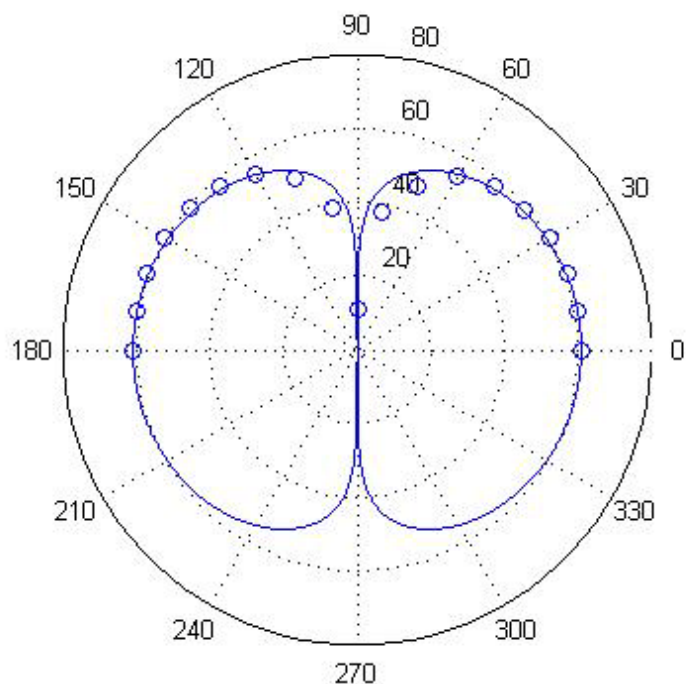


Fig. 6.10: The directivity patterns of the dipole source constructed by two out-of-phase 5.5” unbaffled loudspeakers which are powered by different signal level on two loudspeakers compared with a perfect dipole at 800 Hz. The solid lines (-----) are the directivity pattern of a perfect dipole and the circles (O) are the measured directivity pattern of the dipole source constructed by two out-of-phase 5.5” unbaffled loudspeakers.



Fig. 6.11: The arrangement of the dipole source constructed by two 5.5" inch un baffled loudspeakers.

Chapter 7

Noise propagation in a long enclosure due a dipole source

7.1 Introduction

Reverberation time and signal to noise ratio are two key factors in speech intelligibility [2]. To predict speech intelligibility, previous studies were mainly focused on either sound field propagation or reverberation time predictions [44, 47, 54]. In these studies, the sound sources were usually assumed to be a monopole. However, it is well known that many noise sources have distinct directional characteristics. For example, noise radiated from railway vehicles [66] and ventilating fans are best modelled as a dipole [76]. The current study presents a numerical model to predict the sound field due to a dipole source in a long enclosure. The experimental dipole source was constructed by a pair of identical loudspeakers. The sound field due to a non-symmetrical dipole source is studied afterwards.

7.2 Theory

A dipole sound source can be modelled as a pair of monopoles with equal acoustic power but in anti-phase, separated by a small distance then coupled together. Based on this assumption, two experimental dipole sources were constructed by two unbaffled loudspeakers as in the previous chapter. By referring to figure 7.1, the on-axis one-metre free field sound pressure level (SPL) of a dipole source (SPL_{dipole}) that is created by two out-of-phase monopoles can be calculated by,

$$SPL_{dipole} = 10\log\{10^{[SPL_{mono+} - 20\log(1-\Delta d)]/10} - 10^{[SPL_{mono-} - 20\log(1+\Delta d)]/10}\} \quad (7.1)$$

where SPL_{mono} is the one metre free field SPL of monopole. The plus sign and minus sign following the SPL_{mono} indicate the phase relationship between the monopole and dipole. SPL_{mono+} shows that the sound field of the monopole is the same phase with the dipole at the measuring point and otherwise is anti-phase with the dipole. Δd is the distance between the acoustic centre of the monopole and of the dipole. The one metre free field SPL of the equivalent monopole can be obtained by,

$$SPL_{mono} = SPL_{dipole} + 10\log_{10}\left[\frac{(1-\Delta d)^2(1+\Delta d)^2}{4\Delta d}\right] \quad (7.2)$$

In the real world, most of dipole sources are not fully symmetrical. The sound power radiated from the dipole front should not be the same as the sound power radiated from the dipole back. The free field SPL of two equivalent monopoles should be

calculated separately.

In this study, a long enclosure is modelled as a rectangular enclosure which is constructed by two vertical side walls, two horizontal surfaces and is infinitely long.

All boundary surfaces are assumed as totally reflective and diffusion effect is ignored.

The width of the enclosure is a and the height is b . The left bottom corner of the source plane is chosen at the origin of three-dimensional rectangular co-ordinate system (see figure 7.2).

The width of the enclosure is measured in x direction, height in z direction

and the separation between source and receiver should be measured in y direction. The

monopole source is located at a distance of S_a away from the left sidewall and S_b

above the ground, i.e. $(S_a, 0, S_b)$. Based on the image source method, a row of image

sources is created by the reflections of the vertical sidewalls and their related images.

The x -coordinates of the image sources are given by

$$x_{\pm m} = ma + a_{(m)} \quad \text{for } m = 0, 1, 2, 3, \dots, \quad (7.3a)$$

where

$$a_{(m)} = \begin{cases} a - S_a & \text{if } m \text{ is odd} \\ S_a & \text{if } m \text{ is even} \end{cases} \quad (7.3b)$$

Due to the reflections of the ground, the ceiling and their related images, infinite

columns of image sources are formed similarly. The z -coordinates of those image

sources are given by

$$z_{\pm n} = nh + b_{(n)} \quad \text{for } n = 0, 1, 2, 3, \dots, \quad (7.4a)$$

where

$$b_{(n)} = \begin{cases} b - S_b & \text{if } m \text{ is odd} \\ S_b & \text{if } m \text{ is even} \end{cases} . \quad (7.4b)$$

Then, the image source coordinate is given by $\mathbf{S}_{m,n} = (x_m, 0, z_n)$. The receiver is positioned at a distance R_a from the left sidewall, R_b above the ground and separated by the horizontal distance along the y-axis is y_r to the source. Figure 7.3 displays the distance $D_{m,n}$ between an image source (m, n) and the receiver, and the distance can be calculated,

$$D_{m,n} = \sqrt{(x_m - R_a)^2 + y_r^2 + (z_n - R_b)^2} . \quad (7.5)$$

The related sound pressure level ($RSPL_{m,n}$) contributed by image source (m, n) at the receiver is,

$$RSPL_{m,n} = RSPL_{mono} + 10 \log \left(\frac{(1 - \alpha)^{|m|+|n|}}{D_{m,n}^2} \right) - \alpha_a D_{m,n} \quad (7.6)$$

where $RSPL_{mono}$ is the 1 m free field sound pressure level of the monopole source which is referenced to $20 \mu\text{Pa}$. α is the averaged absorption coefficient of boundary surfaces, α_a is air absorption factor which can be obtained from Ref. 85 for different frequencies.

The related steady-state SPL due to a monopole source at the receiver is given by,

$$RSPL_{Tm} = RSPL_{mono} + 10 \log \left(\sum_{m=-\infty}^{m=\infty} \sum_{n=-\infty}^{n=\infty} \frac{(1-\alpha)^{|m|+|n|}}{D_{m,n}^2} \right) - \alpha_a \left(\sum_{m=-\infty}^{m=\infty} \sum_{n=-\infty}^{n=\infty} D_{m,n} \right). \quad (7.7)$$

Dipole source can be modelled as two out-of-phase monopoles. The steady-state sound field contributed by a dipole source can be calculated by subtracting the total sound field contributed by two equivalent monopoles since two monopoles are totally out-of-phase. The related steady-state sound pressure due to a dipole is given by

$$RSPL_{Td} = RSPL_{Tm+} - RSPL_{Tm-} \quad . \quad (7.8)$$

7.3 Field measurements

7.3.1 Full scale field measurements - a long corridor

Field measurements were conducted in a corridor in the Department of Mechanical Engineering, Hong Kong Polytechnic University. The corridor was 35.6 m long, 1.85 m width and 2.45 m height. The floor was covered with carpet and the ceiling was made up of perforated panels filled with fibreglass. The vertical partition walls were finished with plaster and wooden doors. The absorption coefficients of four boundary surfaces were reused from the previous experimental data since the same location was used to conduct measurements as before [54]. The single absorption coefficient used in the current study is an averaged value of all boundary surfaces on their area proportion. The averaged absorption coefficients from 200 Hz to 4000 Hz are listed in Table 7.1.

The dipole source constructed by two 5.5” un baffled loudspeakers was used as the source. The front-to-back SPL different was 0.1 dB in 800 Hz. The field strength was reconfirmed by separate measurements. The measurements were conducted in an anechoic chamber to measure the free field sound pressure level at 1 m away from the source. The diversity pattern of the dipole is shown in figure 7.4. Same as Chapter 2.3.1, a software based maximum length sequence system analyser (MLSSA) [90] was employed for the current study. MLSSA was run on a personal computer and worked with a special sound card. The test signal was generated from the PC sound card and fed to a power amplifier and then connected to the dipole. The receiver was a “B&K” 4189 pre-polarised free field 1/2” inch condenser microphone and the signal was amplified by a “B&K” Nexus preamplifier then fed into the sound card. The source was fixed at 0.45 m away from the right vertical wall and 0.6 m above ground. For the receiver, it was allocated at 1.2 m above ground and varied between 0.45 and 0.9 m from the right vertical wall (see figure 7.5).

Figure 7.6 shows the variation of the steady-state SPLs at 800 Hz with the horizontal separation. The receiver was located at 1.2 m above the ground and 0.45 m away from the right vertical wall. Since a dipole source is a directional source, two source directions were involved in the measurements. The dipole was facing to vertical

sidewalls and facing the end of the corridor during the measurements. The measured spectra are compared with the numerical predictions according to the proposed formulation. In the graphs, the experimental data agreed reasonably well with the numerical predictions. The maximum prediction error appeared at 1 m source/receiver separation. Although the gap of two equivalent monopoles was assumed as 15 mm in the measurement, actually, the gap of two acoustical centers was tolerated to the designed value. When the receiver closed to the source, direct sound field was dominated. The tolerated locations of two equivalent monopoles caused prediction error. It is suggested that the proposed model only apply to the situation when the source/receiver separation is great the width and the height of the enclosure. The proposed formulation can predict the general trend of the experimental data. The average discrepancies at 800 Hz were found to be 1.74 and 2.72 dB for two source directions respectively.

Next, figure 7.7 shows the variation of the 800 Hz steady-state SPLs with the horizontal separation in the other set measurement. The source location was the same as before but the receiver was moved to 0.9 m away from the right vertical but at same height. Again, the numerical predictions according to the proposed formulation show tolerably good agreements with the measurements in both source directions. In general,

the proposed formulations can predict the average level of measured related steady-state SPLs over the range of interest.

7.3.2 Indoor measurements – a model tunnel

A 28.5 m long, 1.16 m wide and 1.45 m high model tunnel was made for verification of the formulation developed in pervious section. The tunnel sidewalls, floor and ceiling were fully covered by gypsum board. The surface impedance Z of the gypsum board was characterised by two-parameter model [89]. By conducting a short-range propagation measurement which placed both source and receiver 0.1 m above the boundary surface and separated by 1 m, the excess attenuation of the gypsum board was obtained. The parametric values of the effective flow resistivity σ_e and the effective rate of change in porosity with depth α_e were deduced by comparing the measured spectrum to a free field measurement in same source/receiver separation. The best-fit parametric values of σ_e and α_e are 30,000 kPa s m⁻² and 50 m⁻¹ (see figure 7.8). The converted one-third octave band absorption coefficients (α) [54] of the boundary surfaces are listed in table 7.1.

The same set of equipment using in the previous section was employed to conduct the measurements in the model tunnel. The 4” dipole source developed in the previous

chapter was used as the source but the front-to-back SPL different at 800 Hz was adjusted to 0.3 dB. The directivity pattern of the dipole source is shown in figure 7.9.

Figure 7.10 displays the measurements in three source/receiver locations. They were sound level decay curves in the model tunnel with (a) the source was located at 0.3 m away from the right vertical wall, 0.2 m above the ground and the receiver was located at the centre of the width of the cross-section, i.e. 0.58 m from both vertical walls and 0.8 m above the ground, (b) same source location but the receiver was located at 0.86 m away from the right vertical wall and 1.2 m above the ground, and (c) the source was located at 0.86 m away from the right vertical wall, 0.2 m above the ground and the receiver location was the same at (b). There was only one source direction involved in the measurements and the dipole source was always facing the vertical sidewalls of the tunnel. In the graphs, the experimental results are compared with numerical predictions according to the proposed formulation. The measured and numerical predictions agree tolerable well with each other in all three source/receiver locations. The maximum discrepancy between the measurements and numerical predictions was only 2.5 dB found in 1 m separation of the source and receiver located in (a). The average discrepancies in the one-third octave bands were found to be better than the corridor experiments.

7.4 Propagation of non-perfect dipole source in a long enclosure

The prediction model of dipole source propagation developed in section 7.2 was verified by two field measurements with one conducted in a long corridor and the other one conducted in a model tunnel. In both field experiments, the measured data and numerical predictions agreed reasonably well with each other in two source directions. There were some interesting findings when comparing two field measurement results. Although both sizes of the enclosures and absorption coefficients of two experimental sites were similar, propagation loss of dipole sound field in the corridor was much more than in the model tunnel in the same source/receiver separation. As shown in figure 7.6, the propagation loss in the corridor was 10 dB in 10 m source/receiver separation but only 5 dB in the model tunnel (see figure 7.10). Since the same set of measurement equipment was used in both experiments and the experiment results agreed well with numerical predictions, the difference of the propagation loss between two experiments should not be caused by experimental error. Noise sources should be the key affecter of the propagation loss in the experiments since the front-to-back SPL difference of the dipole source used in corridor was only 0.1 dB but 0.3 dB in the model tunnel. In previous studies, noise radiated from railway vehicles and ventilating fans were best modelled as dipole sharp but the directivity

patterns of those sources were tolerable with a perfect dipole [66, 76]. As shown in Hodgson and Li study [80], the front-to-back SPL difference of the noise generated from a computer cooling fan was varied between 0.1 dB to 3 dB on different supply voltages. Similar results were reported in Thomson and Jones' study [74]. The wheel/rail noise of railway vehicles was modelled as a dipole which better modelled than a monopole in axial motion. However, the directivity pattern of wheel/rail noise was not exactly the same as a dipole. Although there is no exact figure quoted on the noise generated from a ventilation fan, it is not difficult to imagine that the directivity pattern of fan noise is tolerant with a perfect dipole source. The propagation loss of non-symmetrical dipole source in long enclosure should be further studied.

7.4.1 Propagation loss of non symmetrical dipole source

The theoretical sound field study of a non symmetrical dipole source was conducted by comparing the propagation loss of different non-symmetrical dipole sources. The comparison included the propagation loss of a monopole source. By reference to the propagation loss of monopole source, the characteristics of non-symmetrical dipole sources are much easier to understand. In the theoretical study, the steady-state contribution of the monopole was calculated by the image source method.

The simulation took place in a long enclosure with the width of 1.5 m and height of 2.5 m. The absorption coefficient of all boundaries was assumed as 0.1. The source was located at 1.3 m above the ground and 0.8 m away from left vertical wall, receiver was placed at 1.2 m above the ground and 0.7 m from the same vertical wall. The front-to-back SPL different of the dipole source is set to (a) 0 dB, i.e. fully symmetrical, (b) 0.1 dB, (c) 0.3 dB, (d) 0.5 dB and (e) 1 dB.

Figure 7.11 displays the propagation losses of dipole sources with different front-to-back SPL differences and of a monopole source. In the figure, the free field source pressure levels of all sound sources were set to 0 dB. It can be seen that the propagation loss of a fully symmetrical dipole source is much more than a monopole. This is the same as the well known characteristics of dipole source; dipole source is a non effective radiator [65]. If a dipole source is not fully symmetrical and the front-to-back SPL difference is 0.1 dB, the propagation loss is reduced more than 19 dB on 10 m source/receiver separation. While the front-to-back SPL differences of the dipole source increased to 0.3 dB, the propagation loss of the said dipole is very similar to a monopole. When the front-to-back SPL differences are further increased, the propagation loss of the dipole is further reduced and becomes even less than a monopole. This is a very interesting dipole characteristic since the dipole source is

assumed as a weaker radiator than a monopole although it is not difficult to understand. When converting a dipole source to two out-of-phase monopoles, the free field SPL of the converted monopole should be larger than the dipole. For example, the sound field of the converted monopole was 12 dB larger than the dipole in the studied case. Since the free field SPL of one of converted monopoles is larger than the other, the contributed sound field from the larger monopole should be larger than from the other one. The sound field can be cancelled out and should become smaller. After the front-to-back SPL difference of the dipole source is further increased, one of the converted monopoles should be much stronger than the other one and the sound field contributed by the weaker monopole can be neglected. The propagation characteristic of a non-symmetrical dipole source is very similar to a monopole now but much stronger. This is because the sound field of the converted monopole is stronger than the corresponding monopole.

7.4.2 Experimental measurements

In order to verify the theoretical study in section 7.4.1, experimental measurements were conducted in the model tunnel. In order to compare the propagation loss of non-symmetrical dipole and monopole source, both sources were involved in the measurements. The dipole source was the source constructed by two 4" unbaffled

loudspeaker with 0.4 dB front-to-back SPL difference at 1 kHz. A “Renkus-Heinz” PN 61 self-power loudspeaker was used as a monopole source. Besides the sound sources, the same set of equipment used in section 7.3.1 and 7.3.2 was employed in the measurements again. In the experiment, both sources were located at 0.3 m away from the right vertical wall and 0.2 m above the ground. The receiver was placed at 0.8 m above ground and 0.3 m away from the same wall. The distances between source and receiver were adjusted between 1 to 9 m. During the measurements, the dipole source was always facing the vertical boundaries.

Figure 7.12 displays the experimental data and numerical predictions of both monopole source and dipole source along the model tunnel. It is shown that the numerical predictions agreed well with experiment data. On average, the difference between the numerical predictions and experimental measurement was around 1 dB for both sources. By compared the results displayed in figure 7.12, it can be seen that the propagation loss of a non symmetrical dipole source with 0.4 dB front-to-back SPL difference was very close to a monopole. The propagation loss of the dipole source was 3 dB less than the corresponding monopole only.

By referring to the experiment results, it can be seen that the theoretical consideration

of the propagation loss of a non-symmetrical dipole source agreed with the experimental data. The concept of dipole source as a less efficient radiator than the corresponding monopole can not be applied in a long enclosure. The front-to-back SPL difference of a dipole source is the key element affecting the excess attenuation of the source.

7.5 Summaries

Apart from acoustic monopole, dipole source is one of the other common noise sources. Noise radiated from railway vehicles and ventilating fans is best modeled as dipole but the study of dipole source propagation in the long enclosures is very limited. A simple prediction model is proposed in the current study, with a dipole source is modeled as two monopoles. The dipole source contribution in a long enclosure can be represented by the difference of the contributions from two monopoles.

Experimental measurements were carried out in two locations to verify the proposed theory and they reported good agreement between predictions and measurements. In practice, most of the dipole noise sources should not be fully symmetrical. The propagation characteristics of non-symmetrical dipole sources were studied. It is found that the propagation loss of a perfect dipole source is the same as the well

known dipole characteristic; a dipole source is a less efficient radiator than the corresponding monopole. If a dipole source is not fully symmetrical, the propagation loss is reduced and it is even less than the corresponding monopole source. Field measurements showed that the characteristics of non-symmetrical dipole agreed with the theoretical consideration. This is a new concept of dipole source characteristics in long enclosures and totally disagreed with the well known dipole source studies.

Normally, dipole noise source is assumed to be a less efficient radiator than the corresponding monopole and it is neglected in the background noise study. As shown in the current study, the propagation loss of dipole sources is varied by the front-to-back sound pressure level difference of the source. The background noise created by a dipole source may be even higher than the corresponding monopole. Dipole source is a non-neglected noise source in the background noise study. Furthermore, the dipole source prediction model can be used to determine the maximum fan noise allowed to be generated when Noise Criteria is given in acoustic design.

Tables

Frequency (Hz)	200	250	315	400	500	630	800
Absorption coefficient (Corridor)	0.021	0.025	0.029	0.034	0.040	0.047	0.054
Absorption coefficient (Model tunnel)	0.029	0.032	0.036	0.041	0.046	0.051	0.058
Frequency (Hz)	1000	1250	1600	2000	2500	3150	4000
Absorption coefficient (Corridor)	0.063	0.072	0.084	0.095	0.11	0.12	0.14
Absorption coefficient (Model tunnel)	0.065	0.072	0.081	0.091	0.10	0.11	0.13

Table 7.1: The estimated mean absorption coefficients of the boundary surfaces of corridor and model tunnel given in dB.

Figures

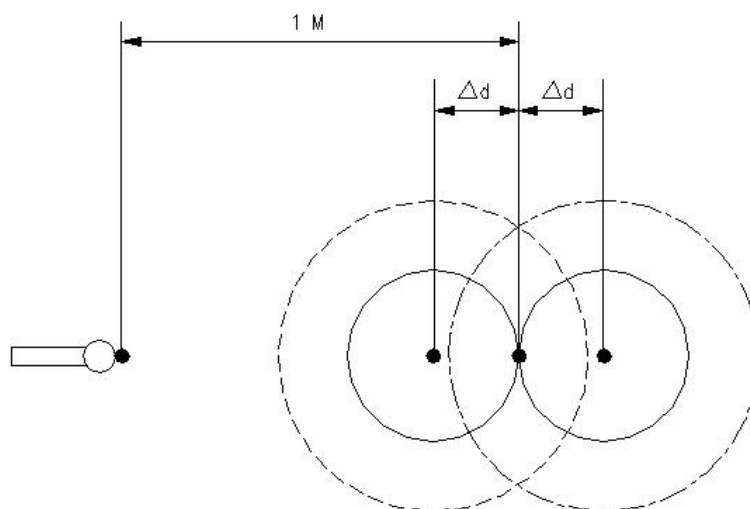


Fig. 7.1: Schematic diagram showing the relative distances of the dipole source and the related monopoles. The solid lines (—) are the source field of dipole source, the dotted lines (· · · · ·) are the sound field of corresponded monopole which is the same phase with the dipole, and dot-dashed lines (· - - - ·) are the sound field of corresponded monopole which is anti-phase with the dipole.

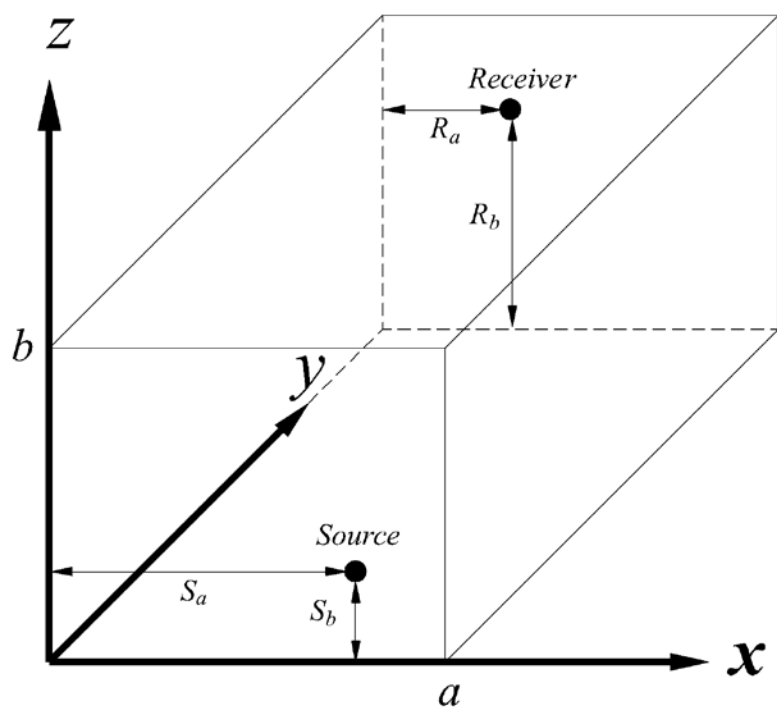


Fig. 7.2: Schematic diagram showing the rectangular coordinate system and the geometrical configuration of a long enclosure.

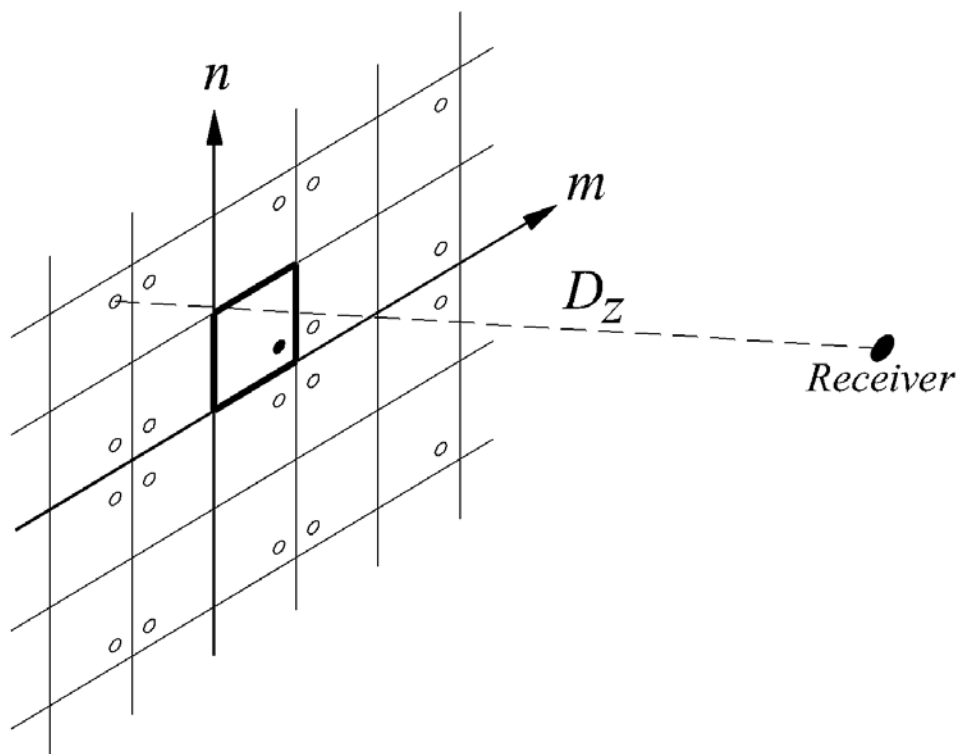


Fig. 7.3: Schematic diagram showing the relative locations of the receiver, the point source (solid circle), image sources (open circle) and the corresponding distance D_z between an image source (m, n) and the receiver.

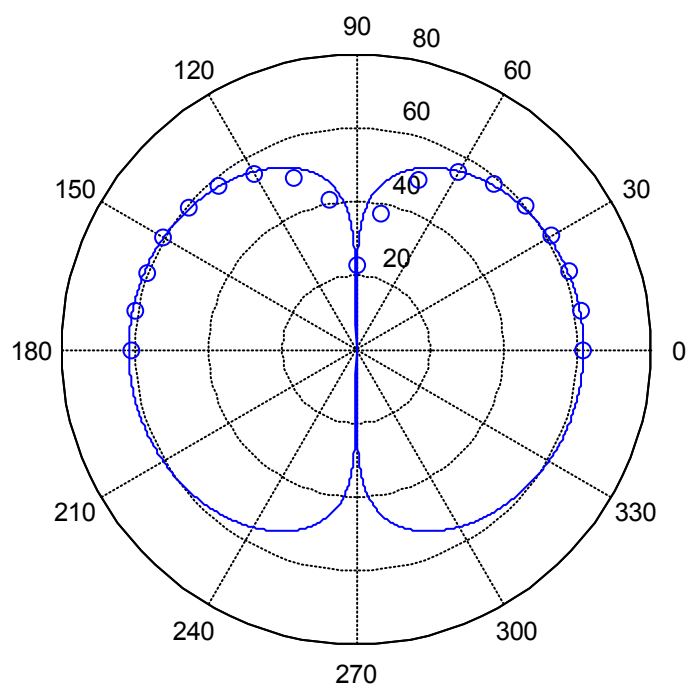


Fig. 7.4: The directivity pattern of the dipole source coupled by two out-of-phase 5.5” un baffled loudspeakers with 0.1 dB front-to-back SPL different at 800 Hz compares with a perfect dipole. The solid lines (—) are the directivity pattern of a perfect dipole and the circles (O) are the measured directivity pattern of the dipole with 0.1 dB front-to-back SPL difference.

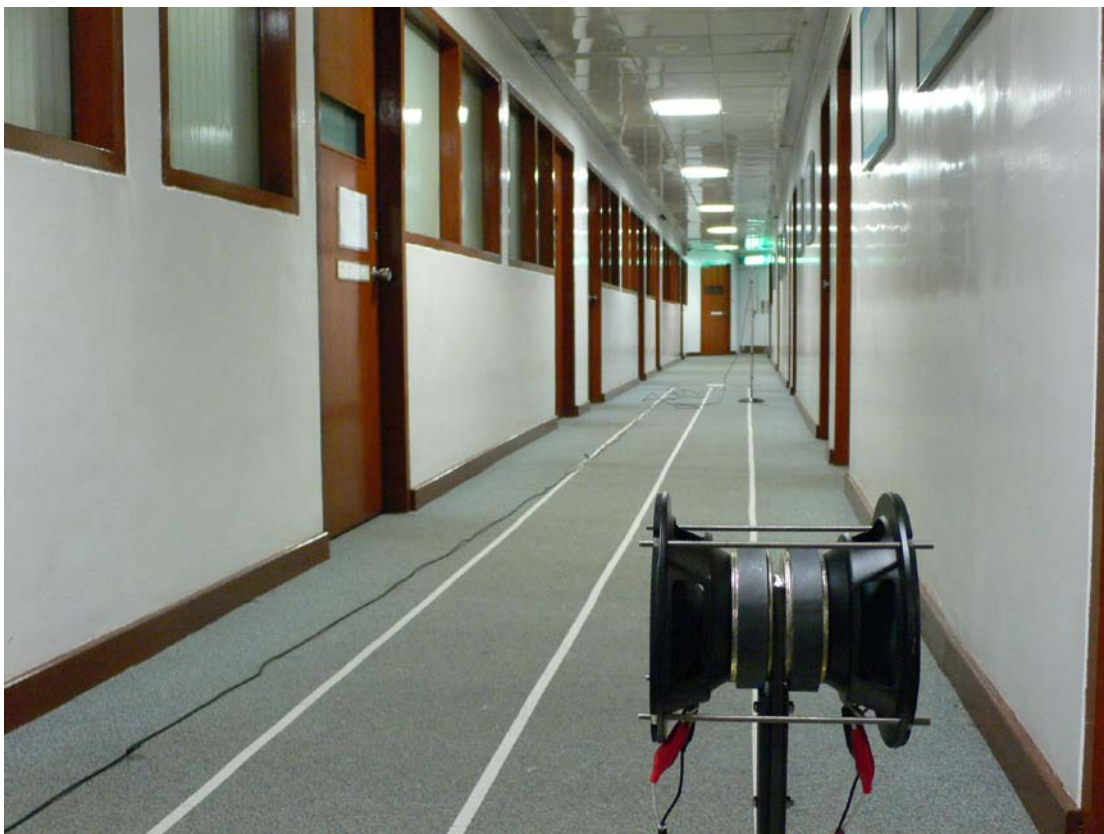


Fig. 7.5: Photograph displaying the set-up of the full scale field measurements in a long corridor.

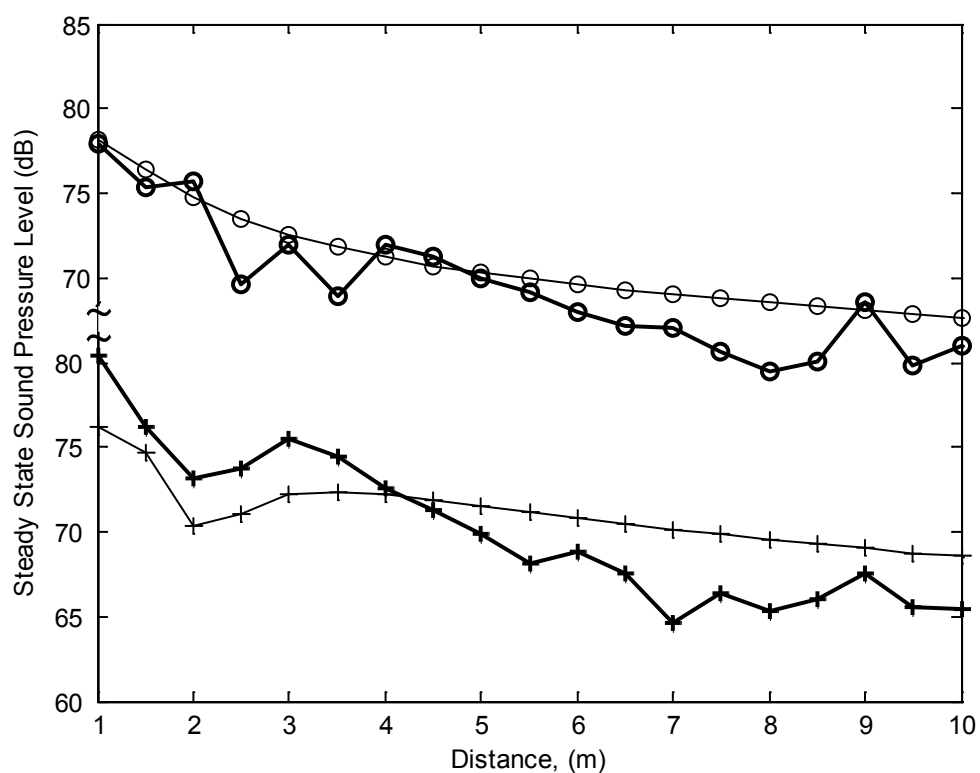


Fig. 7.6: The sound pressure level is plotted versus the horizontal distance. The source was located at 0.6 m above the ground and at 0.45 m from the right side of the vertical wall. The receiver was placed at 1.2 m above the ground and 0.45 from the same wall. The thick solid lines are experimental data and the thin solid lines are predictions by the proposed formulations. (Open circles: dipole faced to side wall; plus signs: dipole faced to end of the corridor).

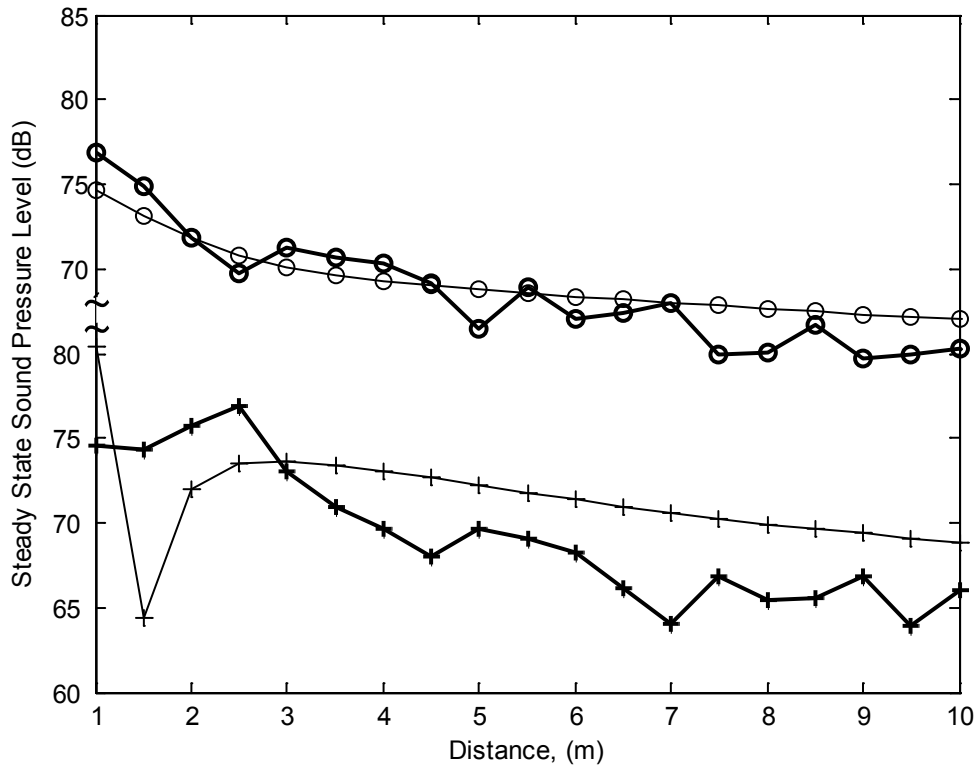


Fig. 7.7: The sound pressure level is plotted versus the horizontal distance. The source located is the same as Fig 7.6. The receiver was placed at 1.2 m above the ground and 0.9 from the right side of vertical wall. The thick solid lines are experimental data and the thin solid lines are predictions by the proposed formulations. The keys for the lines show in the figure are the same as Fig. 7.6.

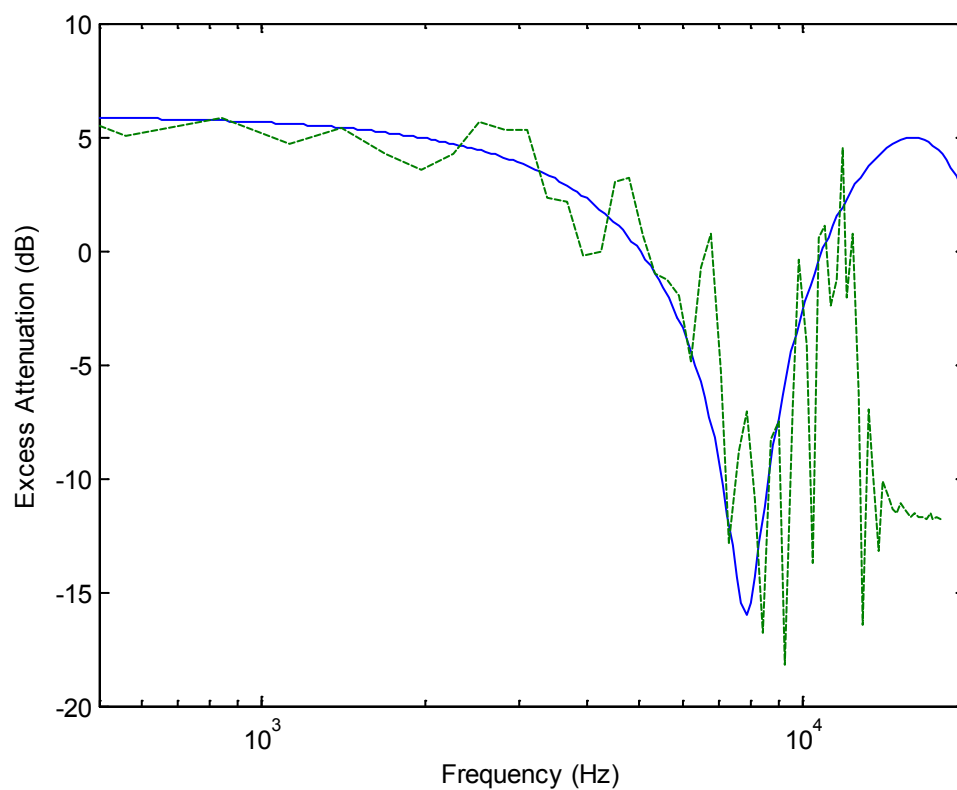


Fig. 7.8: The acoustic characterisation of the gypsum board. The two-parameter model was used to characterise the surface impedances. The best-fit parametric values for σ_e and α_e were 30 000 kPa s m⁻² and 50 m⁻¹. The solid lines are (—) are theoretical predictions and the dotted lines (- - - -) are experimental data.

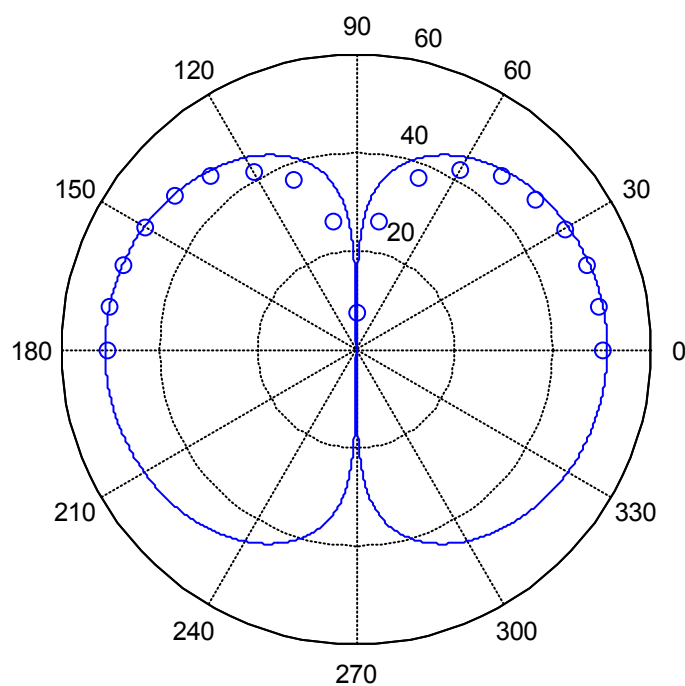


Fig. 7.9: The directivity pattern of the dipole source coupled by two out-of-phase 4” un baffled loudspeakers with 0.3 dB front-to-back SPL different at 800 Hz compare with a perfect dipole. The solid lines (-----) are the directivity pattern of a perfect dipole and the circles (O) are the measured directivity pattern of the dipole with 0.3 dB front-to-back SPL difference.

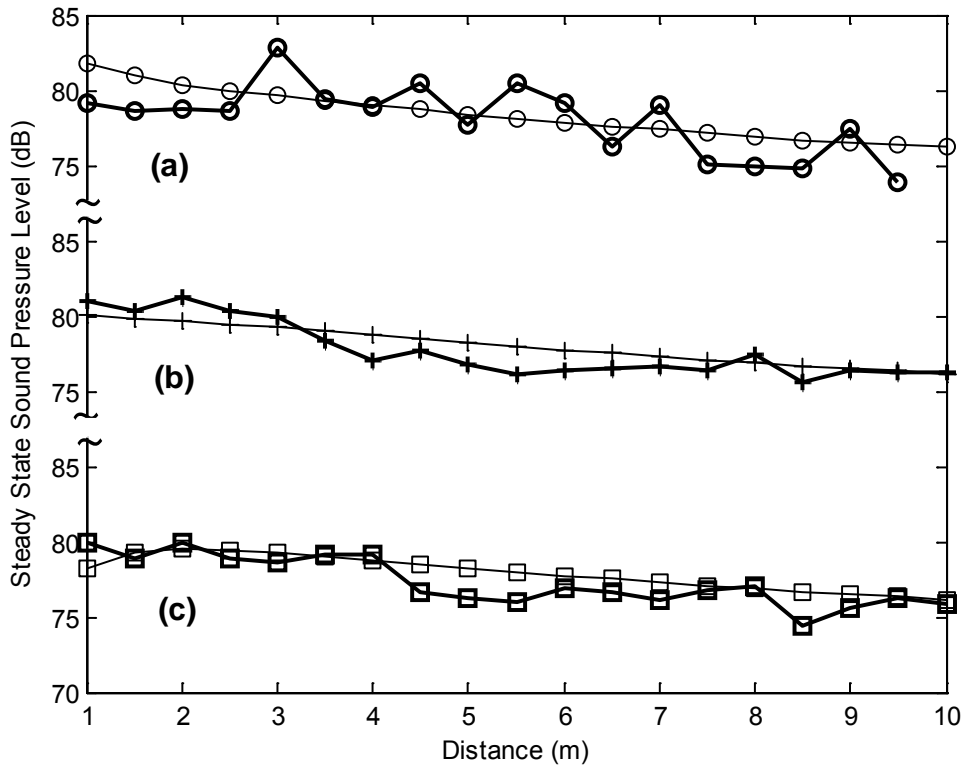


Fig. 7.10: The sound pressure level is plotted versus the horizontal distance. The source and receiver locations were (a) the source was located at 0.2 m above the ground and at 0.3 m from the right side of the vertical wall, receiver was placed at 1.2 m above the ground and 0.45 from the same wall, (b) same source location of (a) but the receiver was located at 0.86 m away from the right vertical wall and 1.2 m above the ground and (c) the source was located at 0.86 m away from the right side wall and 0.2 m above the ground and same receiver location of (b). The thick solid lines are experimental data and the thin solid lines are predictions by the proposed formulations.

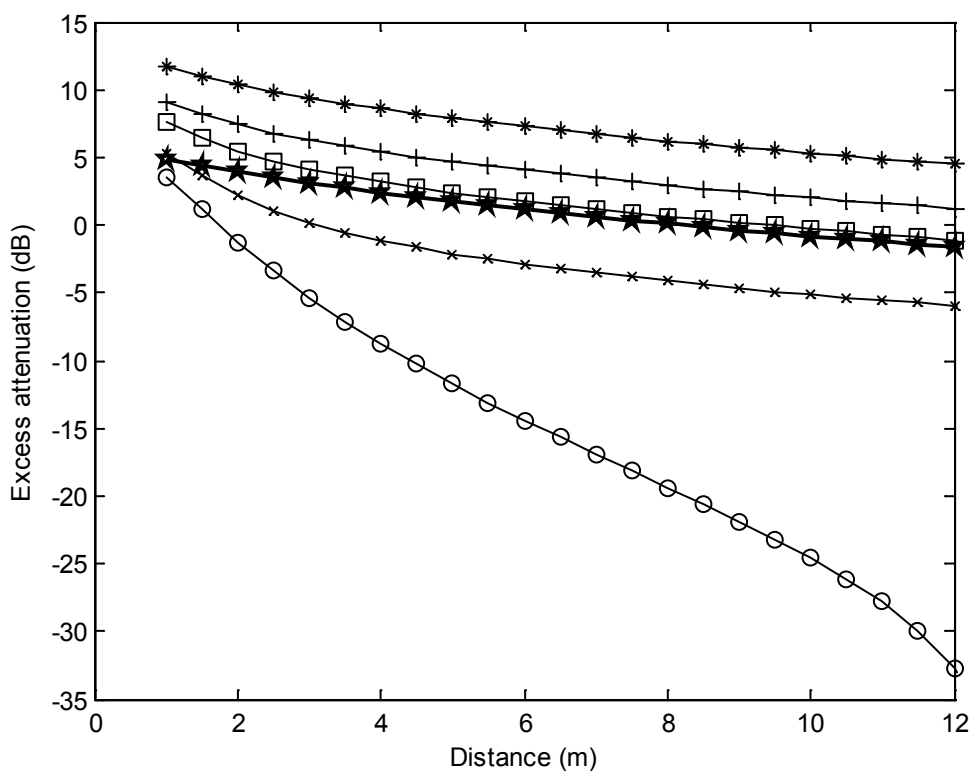


Fig. 7.11: The sound pressure level is plotted versus the horizontal distance. The source was located at 1.3 m above the ground and at 0.8 m from the right side of the vertical wall. The receiver was placed at 1.2 m above the ground and 0.7 from the same wall. The thick solid line with star signs are excess attenuation of monopole source and the thin solid lines are excess attenuation of dipole sources. (Open circles: fully symmetrical dipole source; cross signs: dipole with 0.1 dB front-to-back SPL different; squares: dipole with 0.3 dB front-to-back SPL different; plus signs: dipole with 0.5 dB front-to-back SPL different; asterisks: dipole with 1 dB front-to-back SPL different).

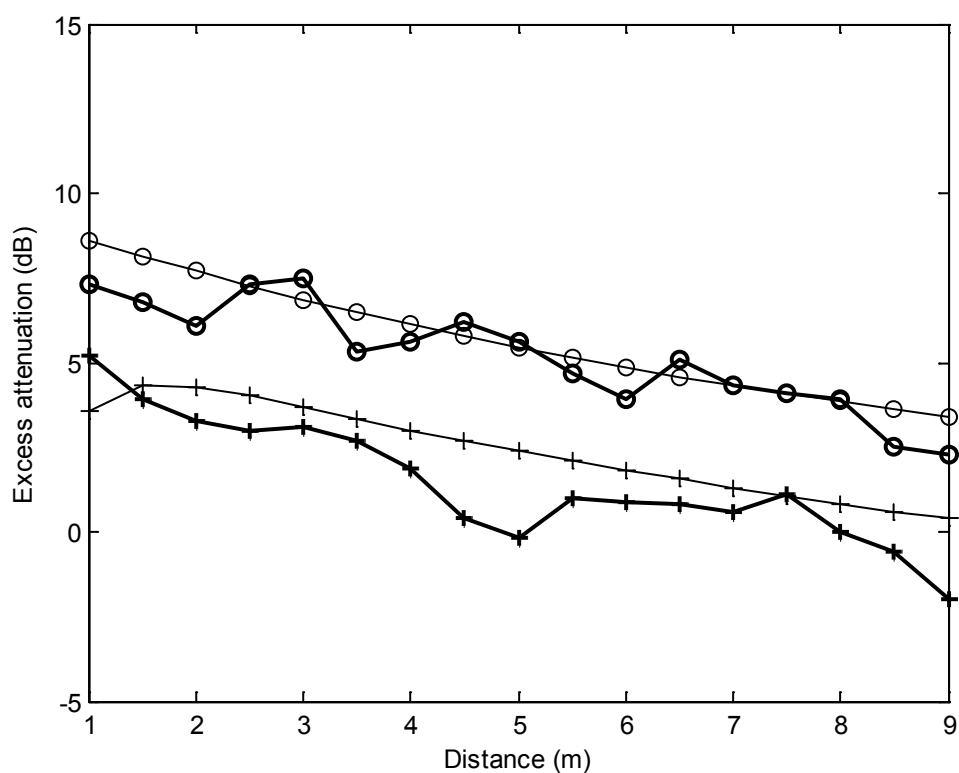


Fig. 7.12: The excess attenuation is plotted versus the horizontal distance. The source was located at 0.2 m above the ground and at 0.3 m from right side of the vertical wall. The receiver was placed at 0.8 m above the ground and 0.3 from the same wall. The thick solid lines are experimental data and the thin solid lines are predictions by the proposed formulations. (Open circles: monopole source; plus signs: dipole source).

Chapter 8

Conclusion and suggestions for future work

8.1 Conclusion

Long enclosure is a common feature in built-up areas. For instance, an underground train station and its platform, a road or railway tunnel, a pedestrian subway and a corridor in buildings. Normally, acoustic consideration is not placed in the first priority when constructing long enclosures. Cost consideration and associated maintenance problems drive engineers to use fewer sound absorption materials for noise reduction. The associated acoustic problems in a long enclosure are high ambient noise and lack of speech intelligibility. The public address (PA) system is normally installed in a long enclosure for delivery announcements especially for fire drills and verbal warnings. However, increasing the sound power output of the PA system can improve the audibility but not necessarily speech intelligibility. The objective of this study is to simplify the prediction of sound field in a long enclosure in order to improve the speech intelligibility.

On the other hand, traffic noise is one of the most cited environmental factors in high-rise cities. A simple steady-state noise level and reverberation time evaluation formula can help to assess the effectiveness of noise control. By treating the flanking façades as a pair of parallel side walls, the road pavement is taken as the floor, and the opening at the top is represented by a perfectly absorptive ceiling, and a street canyon can be considered as a category of a long enclosure. This study is started by developing a simple formula to estimate steady-state noise levels and reverberation times of a straight street canyon. The formula is developed from the image source method. By replacing the discrete image sources with an effective line source, an integral formulation is proposed in the study. The formulation is validated by comparing the predictions with published data conducted in a town street, and with indoor and outdoor experimental data obtained in the present study. It has been demonstrated that the predictions according to the integral formulation agreed reasonably well with both published data and all experimental data obtained in the present study. The average discrepancies of steady state sound field between experimental data and theoretical prediction were within 3 dB. The integral formulation can be used to provide an efficient model for predicting noise levels and the reverberation effect in a street canyon. Since the proposed integral formulation is a simple closed form solution, it is much useful than the other theoretical numerical

models in practice especially for daily application.

The concept developed in chapter 2 was further applied in predicting steady-state sound fields in a long enclosure. By considering the discrete image sources in a long enclosure as effective area sources, an analytical formula has been developed to estimate the steady-state sound fields. The prediction accuracy of the analytical formula was validated by comparing the numerical predictions with indoor model measured data and full-scale outdoor experimental results. The average discrepancies between the measurement and prediction were less than 3 dB. By using this single formula, it is believed accurate enough for predicting the steady-state sound field in a long enclosure.

Apart from the straight long enclosure, there are other variations. A cross junction, a long enclosure with a T-intersection, and U-turn long enclosures are some typical examples. A theoretical model is proposed for estimating the steady-state sound fields and reverberation times for a junction of a street canyon. The theoretical model can be applied to both coherent and incoherent image source methods. By comparing with field measurements, it was shown that the sound fields and reverberation times in four legs of a street's junction can reasonably be computed. Although the predictions of the

coherent model provided better agreement than the predictions of the incoherent model to the experimental data, the calculations of incoherent model still laid on the general trend of the measurements. Actually, the average different between measurements and calculations of two prediction models was within 2 dB. The sound fields in the opposite ends of the street canyon have been studied by using the incoherent ray model. By comparing to a straight street canyon, the opening of a junction can help to reduce the traffic noise only when the receiver is close to the junction. The distance between the source and junction do not affect the noise level at the receiver. The efficient way to reduce the traffic noise in the opposite end of the street is increased the width of the junction.

The model is extended to predict the steady-state sound fields and reverberation times in a long enclosure with a T-intersection. The prediction capability of the proposed model integrated with the coherent image source method and incoherent method were displayed by comparing with experiments conducted in a model tunnel with a T-intersection and in a corridor. It can be seen that the predictions by the proposed model integrated with coherent image source method agreed reasonable well with measured data and provided better agreement than using the proposed model integrated incoherent method. However, the predictions of incoherent model

consistent with the general trend of measured excess attenuations and laid on the general trend of the reverberation times.

In all previous acoustical studies related to a long enclosure, most studies are focused on a monopole sound source. Apart from non-directional noise source, many noise sources in a long enclosure are directional. Both train noise and fan noise are classified as dipole rather than non-directional monopole. In order to study the characteristics of directional noise sources, a review of available dipole sources was conducted. It was shown that both sound power output and frequency range are the limitations to use the available dipole sources to conduct experimental study in long enclosure. A numbers of dipole sources were constructed afterwards. The dipole sources were constructed by pairs of identical loudspeakers which were powered by anti-phase, placed by back to back and close to each other. By using the dipole source constructed by two loudspeakers, both sound power output and frequency range were much improved. In this study, the maximum sound power output of the constructed dipole was 107 dB and the usable frequency was 2 kHz.

A theoretical study of propagation due a dipole sound source was conducted. By modelling a dipole source as a pair of monopoles but in anti-phase, the sound field

contributed from a dipole source can be obtained by subtracting the contribution from two equivalent monopoles since two equivalent monopoles are totally out-of-phase. Field measurements were conducted in a model tunnel that was built in an anechoic chamber and a corridor in an office building. It can be seen that numerical predictions according to the proposed theory agreed with experimental data at both sites. The propagation loss of a perfect dipole source is much more than the corresponding monopole. Perfect dipole source is a less efficient radiator than the corresponding monopole. Furthermore, the propagation characteristics of non-symmetric dipole sources have also been studied. It was demonstrated that the source field contributed from a non non-symmetric dipole is similar or even larger than a corresponding monopole source. Dipole source is a non-neglected noise source in long enclosures.

8.2 Limitations of developed models

In this study, all sound field propagation models are developed from the image source method. The limitations of the image source method also applied to this study. They are included but not limited to

1. For an indoor space, the geometry of a long enclosure should be arranged such that one of the dimensions is much larger than the remaining two dimensions. Furthermore, these two remaining dimensions are still relatively greater than

the acoustic wavelength of interest. The proposed theory can also be applied to outdoor long spaces when the length is much larger than the wide. In practice, it is suggested that the length of the long space is greater than six times the width and the height (indoor only) [94].

2. The boundary surfaces of the long space are assumed to be acoustically “smooth”. In other words, the sound fields in the long space are dominated by the reflective sound fields. The theories developed in this study cannot apply in the long space with many irregular boundary surfaces. It is because sound wave reflected from irregular boundaries cause diffused sound fields.

8.3 Suggestions for future work

Owing to the time limit in this study, there are still other research problems waiting to be explored. The following areas are recommended for further exploration:

1. Closed form solutions have been developed to simplify the sound field prediction in street canyons and long enclosures. The models need to be extended to cover the sound fields in a junction of a street canyon and also in a long enclosure. This can help to reduce the calculation time and speed up the design.

2. Transportation noise is a major issue in a high-rise city. Studies of noise propagation through a segment of a straight street canyon and a junction of a street canyon were conducted in the present study. In real applications, studies of noise propagation in a city should focus on an area rather than a segment. The noise studies in street canyons and junctions need to be combined together. The combined model can be used to study the noise propagation in a district and prepare noise maps in a city.

3. Studies for predicting the sound fields in a straight long enclosure and a long enclosure with a T-intersection have been conducted in the study. Apart from the straight long enclosure and long enclosure with a T-intersection, long enclosure with an L-shaped section and U-turn long enclosures are commonly found in office buildings and shopping malls. Although sound field in L-shaped section and U-turn enclosure is possible predicted by image source method [39 – 41], there is still no any detail formulation reported in related studies. In the current study, it is recommended to extend research to predict the sound fields in a long enclosure with an L-shaped section and U-turn long enclosure. This extension would help to consider the realistic aspects of a sound field in a building environment.

4. When the public address (PA) system is installed in a long enclosure, it is not limited to one speaker. Increasing the numbers of speakers can improve the even distribution of sound fields in the covered area but also increase the reverberation fields and echoes. In this case, increasing the numbers of speakers does not necessarily improve the speech intelligibility and can even degrade the speech intelligibility. Studies of multi source distribution in long enclosure therefore become necessary. Furthermore, closed form solution is much useful than the theoretical model.

5. Regarding long enclosure with end walls, this was not limited to the current study. The long enclosure is assumed to be infinitely long in most long enclosure's studies. In the real situation, a long enclosure should be limited in length and the sound wave would be reflected back by terminations. The termination is either a solid object such as hard wall or wooden door, or impedance mismatched boundary. The sound wave reflected from termination would increase both usable and non-usable sound fields. The reflected sound wave can be considered as a sound source (image source) in the enclosure. The effect of end termination should be further studied by

closed form solutions.

References

1. T. Houtgast and H. J. M. Steeneken, "The modulation transfer function in room acoustics as predictor of speech intelligibility," *Acustica* **28**, 66-73 (1973).
2. H. J. M. Steeneken and T. Houtgast, "A physical method for measuring speech-transmission quality," *J. Acoust. Soc. Am.* **67**, 318-326 (1980).
3. H. J. M. Steeneken and T. Houtgast, "RASTI: a tool for evaluating auditoris," *Brüel & Kjør Technical Review* **3**, 13-39 (1985).
4. W. C. Sabine, *Collected papers on Acoustics*, (Harvard University Press, Cambridge, MA, 1927).
5. L. L. Beranek, *Acoustics*, (The American Institute of Physics, New York, NY, 1986).
6. T. Yamamoto, "On the distribution of sound in a corridor," *J. Acoust. Soc. Japan.* **17**, 286-292 (1961).
7. Grant Fairbanks, "Test of phonemic differentiation: rhyme test," *J. Acoust. Soc. Am.* **30**(7), 596-600 (1958).
8. Irwin Pollack, Herbert Rubenstein and Louis Decker, "Intelligibility of know and unknown message sets," *J. Acoust. Soc. Am.* **31**(3), 273-279 (1959).
9. Arthur R. House, Carl E. Williams, Michael H. L. Hecker, and K. D. Kryter, "Articulation testing methods: Consonantal differentiation with a closed response

- set,” J. Acoust. Soc. Am. **37**(1), 158-166 (1965).
10. B. Wayne. Anderson and Joel T. Kalb, “English verification of the STI method for estimating speech intelligibility of a communications channels,” J. Acoust. Soc. Am. **81**(1), 1982-1985 (1987).
 11. H. Fletcher and J. C. Steinberg, “Articulation testing methods,” Bell. Sys. Tech. J. **8**, 806-854 (1929).
 12. N. R. French and J. C. Steinberg, “Factors governing the intelligibility of speech sounds,” J. Acoust. Soc. Am. **19**, 90-119 (1947).
 13. K. D. Kryter, “Methods for the calculation and use of the articulation index,” J. Acoust. Soc. Am. **34**, 1689-1697 (1962).
 14. R. Plomp, H. J. M. Steeneken and T. Houtgast, “ Predicting speech intelligibility in rooms from the Modulation Transfer Function. I. General room acoustics,” Acustica **46**, 60-72 (1980).
 15. R. Plomp, H. J. M. Steeneken and T. Houtgast, “ Predicting speech intelligibility in rooms from the Modulation Transfer Function. II. Mirror image computer model applied to rectangular rooms,” Acustica **46**, 73-81 (1980).
 16. H. J. M. Steeneken and T. Houtgast, “Mutual dependence of the octave-band weights in predicting speech intelligibility,” Speech Communication **28**, 109-123 (1999).

17. IEC 60268-16, "Objective rating of speech intelligibility by speech transmission index," (1998).
18. C. F. Eyring, "Reverberation time in dead rooms," J. Acoust. Soc. Am. **1**, 217-241 (1930).
19. G. Millington, "A modified formula for reverberation," J. Acoust. Soc. Am. **4**, 69-82 (1932).
20. D. Fitzroy, "Reverberation formula which seems to be more accurate with nonuniform distribution of absorption," J. Acoust. Soc. Am. **31**, 893-897 (1959).
21. H. Arau-Puchades, "An improved reverberation formula," Acustica **65**, 163-180 (1988).
22. Naylor G, "ODEON – another hybrid room acoustic model," Applied Acoustics **38**, 131-143 (1993).
23. S. M. Dance and B.M. Shield, "The complete image-source method for the prediction of sound distribution in non-diffuse enclosed spaces," J. Sound and Vibration **201**(4), 473-489 (1997).
24. S. M. Dance, "The representation of fittings in the computer prediction of sound propagation in enclosed spaces," Applied Acoustics **52**(1), 71-83 (1997).
25. S. M. Dance, "Minimal input models for sound level prediction in fitted enclosed spaces," Applied Acoustics **63**, 359-372 (2002).

26. J. E. Piercy, T. F. Embleton, and L. C. Sutherland, "Review of noise propagation in the atmosphere," *J. Acoust. Soc. Am.* **61**(6), 1403-1418 (1977).
27. J. E. Volkmann and M. L. Graham, "A survey on air raid alarm signals," *J. Acoust. Soc. Am.* **14**, 1-9 (1942).
28. L. M. Ball, "Air raid siren field tests," *J. Acoust. Soc. Am.* **14**, 10-13 (1942).
29. F. W. Wiener, C. I. Malme, and C. C. Gogos, "Sound propagation in urban areas," *J. Acoust. Soc. Am.* **37**, 738-747 (1965).
30. D. Aylor, J. Y. Parlange, and C. Chapman, "Reverberation in a city street," *J. Acoust. Soc. Am.* **54**, 1754-1757 (1973).
31. K. W. Yeow, "External reverberation times observed in built-up area," *J. Sound Vib.* **48**, 438-440 (1976).
32. K. W. Yeow, "Decay of sound levels with distance from a steady source observed in a built-up area," *J. Sound Vib.* **52**, 151-154 (1977).
33. N. W. M. Ko and C. P. Tang, "Reverberation time in a high-rise city," *J. Sound Vib.* **56**, 459-461 (1978).
34. P. Steenackers, H. Myncke, and A. Cops, "Reverberation in town streets," *Acustica* **40**, 115-119 (1978).
35. R. H. Lyon, "Roles of multiple reflections and reverberation in urban noise propagation," *J. Acoust. Soc. Am.* **55**, 493—503 (1974).

36. H. G. Davies, "Multiple-reflection diffuse-scattering model for noise propagation in streets," *J. Acoust. Soc. Am* **64**(2), 517-521 (1978).
37. J. Picaut, L. Simon and J. Hardy, "Sound field modeling in streets with a diffusion equation," *J. Acoust. Soc. Am.* **106** (5), 2638-2645 (1999).
38. J. Kang, "Sound propagation in street canyons: Comparison between diffusely and geometrically reflecting boundaries," *J. Acoust. Soc. Am.* **107** (3), 1394-1404 (2000).
39. S. T. So, W. S. Fung, C. W. Leung and K. M. Li, "Transmission of sound in a long enclosure with a "T" intersection," *ICSV 14*, Cairns, Australia, (2007).
40. S. T. So and K. M. Li, "Image source methods for prediction of sound fields in a U-shape section," *ICSV 15*, Daejeon, Korea, (2008).
41. S. T. So and K. M. Li, "Comparison of conical beam and image source methods for prediction of sound fields in a branching tunnel," *J. Acoust. Soc. Am* **122**(5), 2963-2963 (2007).
42. H. G. Davies, "Noise Propagation in corridors," *J. Acoust. Soc. Am.* **53**, 1253-1263 (1973).
43. H. Kuttruff, "Zur Berechnung von Pegelmittelwerten und Schwankungsgrößen bei Straßenlärm," *Acustica* **32**, 57 (1975).
44. M. V. Sergeev, "Scattered sound and reverberation on city streets and in tunnels,"

- Sov. Phys. Acoust. **25**(3), (1979).
45. T. L. Redmore, "A theoretical analysis and experimental study of the behaviour of sound in corridors," *Applied Acoustics* **15**, 161-170 (1982).
46. J. Kang, "The unsuitability of the classic acoustical theory in long enclosures," *Architectural Science Review* **39**, 89-94 (1996).
47. J. Kang, "Reverberation in rectangular long enclosures with geometrically reflecting boundaries," *Acustica* **82**, 509-516 (1996).
48. J. Kang, "A method for predicting acoustic indices in long enclosures," *Applied Acoustics*. **51**, 169-180 (1997).
49. L. Yang and B. M. Shield, "The prediction of speech intelligibility in underground stations of rectangular cross section," *J. Acoust. Soc. Am.* **109**(1), 266-273 (2001).
50. J. Kang, "Reverberation in rectangular long enclosures with diffusely reflecting boundaries," *Acustica –Acta Acustica* **88**, 77-87 (2002).
51. K. K. Lu and K. M. Li, "The propagation of sound in narrow street canyons," *J. Acoust. Soc. Am.* **112**(2), 537-550 (2002).
52. K. M. Li and K. K. Lu, "Propagation of sound in long enclosures," *J. Acoust. Soc. Am.* **116**(5), 2759-2770 (2004).
53. K. M. Li and K. K. Lu, "Full-scale measurements for noise transmission in

- tunnels,” J. Acoust. Soc. Am. **117**(3), 1138-1145 (2005).
54. K. M. Li and P. M. Lam, “Prediction of reverberation times and speech transmission index in long enclosures,” J. Acoust. Soc. Am **117**(6), 3716-3725 (2005).
55. S. J. V. Wijngaarden and J. A. Verhave, “Prediction of speech intelligibility for public address systems in traffic tunnels,” Applied Acoustics **67**, 306-323 (2006).
56. D. J. Oldham and M. M. Radwan, “Sound propagation in city streets,” Bldg. Acoust. **1**, 65-88 (1994).
57. E. Walerian, R. Janczur and M. Czechowicz, “Sound level forecasting for city-centers. Parts 1: sound level due to a road within an urban canyon,” Applied Acoustics **62**, 359-380 (2001).
58. M. Hodgson, R. Rempel and S. Kennedy, “Measurement and prediction of typical speech and background-noise levels in university classrooms during lectures,” J. Acoust. Soc. Am. **105**(1), 226-233 (1999).
59. M. Hodgson, “Rating, ranking, and understanding acoustical quality in university classrooms,” J. Acoust. Soc. Am. **112**(2), 568-575 (2002).
60. N. Heerema and M. Hodgson, “Empirical models for predicting noise levels, reverberation times and fitting densities in industrial workrooms,” Applied Acoustics **57**, 51-60 (1999).

61. C. Talottea, P. E. Gautiera, D. J. Thompsonb and C. Hansonc, “Identification, modelling and reduction potential of railway noise sources: a critical survey,” *J. Sound and Vibration* **267**, 447-468 (2003).
62. M. J. Lighthill, “The Bakerian lecture, 1961. Sound generated aerodynamically,” *Proceeding of the Royal Society of London, Series A*, 267, no. 1329, 147-182 (1962).
63. C. Talottea, “Aerodynamic noise: a critical survey,” *J. Sound and Vibration* **231**(1), 549-562 (2000).
64. M. J. Crocker (ed.), *Handbook of Acoustics*, (Wiley, New York, 1998).
65. A. P. Dowling and J. E. F. Williams, *Sound and Sources of Sound*, (E. Horwood, Chichester, 1983).
66. S. Peters, “The prediction of railway noise profiles,” *J. Sound and Vibration* **32**(1), 87-99 (1974).
67. E. J. Rathe, “Railway noise prediction,” *J. Sound and Vibration* **51**(3), 371-388 (1977).
68. D. Hohenwarter, “Railway noise propagation models,” *J. Sound and Vibration* **141**(3), 17-41 (1990).
69. Österreichisches Normungsinstitut, Berechnung der schallimmission durch schienenverkehr, Zugverkehr, verschub- und umschlagbetrieb, Önorm S 5011,

- Österreichisches Normungsinstitut, Vienna, Austria, (1995) (in German).
70. Österreichischer Arbeitsring für Lärmbekämpfung, Schallabstrahlung und Schallausbreitung, ÖAL 28, Österreichischer Arbeitsring für Lärmbekämpfung, Vienna, Austria, (1987) (in German).
71. Deutsche Bundesbahn, Richtlinie zur berechnung der schallimmissionen von schienenwegen, Schall 03/Akustik 03, Deutsche Bundesbahn Zentralamt, München, Germany, (1990) (in German).
72. Bundesamtes Für Umwelt, Walt und Landschaft und Bundesamtes Für Verkehr, Semibel version 1, Schweizerisches emissions-und immissionsmodell für die berechnung von eisenbahnlärm, Schriftenreihe Umweltschutz Nr.116, Bundesamtes für umwelt, walt und landschaft und Bundesamtes für Verkehr, Bern, Austria, (1990) (in German).
73. Ministerie Volkshuisvesting, Ruimtelijke Ordening en Milieubeheer, Reken- en meetvoorschrift railverkeerslawaaai (Draft), Ministerie volkshuisvesting, ruimtelijke ordening en milieubeheer, Directie Geluid en Verkeer, The Hague, Netherlands, (1996) (in Dutch).
74. D. J. Thomson and C. J. C. Jones, "Sound Radiation from a vibrating railway wheel," *J. Sound and Vibration* **253**(2), 401-419 (2002).
75. J. Busch-Vishniac, J. E. West, C. Barnhill, T. Hunter, D. Orellana, and R.

- Chivukula, "Noise levels in Johns Hopkins Hospital," *J. Acoust. Soc. Am.* **118**(6), 3629-3645 (2005).
76. P. K. Baade, "Effects of acoustic loading on axial flow fan noise generation," *Noise Control Engineering Journal*, Jan.-Feb., 5-15 (1977).
77. E. J. Margetts, "A demonstration that an axial fan in a ducted inlet ducted outlet configuration generates predominantly dipole noise," *J. Sound and Vibration*, **117**(2), 399-406 (1987).
78. M. C. Thompson, K. Hourigan and A. N. Stokes, "Prediction of the noise generation in a centrifugal fan by solution of the acoustic wave equation," *International Symposium on Fan Noise*, 197-204 (1992).
79. W. Neise, "Review of fan noise generation mechanisms and control methods," *International Symposium on Fan Noise*, 45-56 (1992).
80. M. Hodgson and I. Li, "Experimental study of the noise emission of computer cooling fans," *Applied Acoustics* **67**, 849-863 (2006).
81. C. H. Chew, "Prediction of traffic noise from expressways-Part 1: Buildings flanking one side of expressways," *Appl. Acoust.* **28**, 203-212 (1989).
82. C. H. Chew, "Prediction of traffic noise from expressway-Part II: Buildings flanking both sides of expressways," *Appl. Acoust.* **32**, 61-72 (1991).
83. K. K. Chin, K. Y. Ng, S. K. Soon, and H. T. Chui, "A study of urban traffic

- noise,” Proceedings Western Pacific Regional Acoustics Conference **2**, 142-145 (1997).
84. K. M. Li, “Managing environment noise in Hong Kong,” J. Acoust. Soc. Am. **115**, 2593 (2002).
85. “Method for calculation of the absorption of sound by the atmosphere,” American National Standards Institute S1.26 (1995).
86. M. Abramowitz and I. A. Stegun, Handbook of Mathematical Functions, With Formulas, Graphs and Mathematical Tables (Wiley, New York, 1972). Chap. 5.
87. M. R. Schroeder, “New method of measuring reverberation time,” J. Acoust. Soc. Am. **37**, 409-412 (1965).
88. G. A. Daigle, M. R. Stinson, and D. I. Havelock, “Experiments on surface waves over a model impedance plane using acoustical pulses,” J. Acoust. Soc. Am. **99**, 1993-2005 (1996).
89. K. Attenborough, “Ground parameter information for propagation modeling,” J. Acoust. Soc. Am. **92**, 418-427 (1992).
90. D. D. Rife and J. Van der Kooy, “Transfer-function measurement with maximum-length sequences,” J. Audio Eng. Soc. **37**, 419-443 (1989).
91. T. A. Busch and M. R. Hodgson, “Improved method for selecting scale factors and model materials for scale modelling of outdoor sound propagation,” J. Sound

- Vib. **243**, 173-181 (2001).
92. K. V. Horoshenkov, D. C. Hothersall, and S. E. Mercy, "Scale modelling of sound propagation in a city street canyon," J. Sound Vib. **223**, 795-819 (1999).
93. E. A. Lehmann and A. M. Johansson, "Prediction of energy decay in room impulse responses simulated with an image-source model," J. Acoust. Soc. Am **124**(1), 269-277 (2008).
94. J. Kang, Acoustics of long spaces (Thomas Telford Publishing, London, 2002).
95. ISO 10534-2, "Acoustics – Determination of sound absorption coefficient and impedance in impedance tubes – Part 2: Transfer-function method," 2001.
96. G. Jones and W. Galloway, "Motor vehicle noise: Identification and analysis of situations contributing to annoyance," BBN Rep. No. 2082 (1971).
97. S. Fidell, "Nationwide urban noise survey," J. Acoust. Soc. Am **64**(1), 198-206 (1978).
98. E. Öhrström, "Longitudinal surveys on effects of changes in road traffic noise – annoyance, activity disturbances, and psycho-social well being," J. Acoust. Soc. Am **115**(2), 719-729 (2004).
99. M. R. Ismail and D. J. Oldham, "A scale model investigation of sound reflection from building facades," Applied Acoustics **66**, 123-147 (2005).
100. T. L. Pollès, J. Picaut and M. Bérengier, "Sound field modeling in a street canyon

- with partially diffusely reflecting boundaries by the transport theory,” J. Acoust. Soc. Am. 116 (5), 2969-2983 (2004).
101. K. M. Li and C. Y. C. Lai, “A note on noise propagation in street canyons,” J. Acoust. Soc. Am. 126 (2), 644-655 (2009).
102. M. R. Schroeder, “Integrated-impulse method measuring sound decay without using impulse,” J. Acoust. Soc. Am **66**(2), 497-500 (1979).
103. W. T. Chu, “Comparison of reverberation measurements using Schoreder’s impulse method and decay-curve averaging method,” J. Acoust. Soc. Am **63**(5), 1444-1450 (1978).
104. K. M. Li, C. W. Leung and C. Y. C. Lai, “Transmission of noise through a junction in a street canyon,” to be published.
105. Z. Hu and J. S. Bolton, “Sound propagation from an arbitrarily oriented multi-pole placed near a plane, finite impedance surface,” J. Sound and Vibration **170**(5), 637-669 (1994).
106. K. M. Li, S. Taherzadeh, and K. Attenborough, “Sound propagation from a dipole source near an impedance plane,” J. Acoust. Soc. Am **101**(6), 3343-3352 (1997).
107. T. A. Beauvilian, J. S. Bolton, and B. K. Garder, “Sound cancellation by the use of secondary multipoles: Experiments,” J. Acoust. Soc. Am **107**(3), 1189-1202 (2000).

108. J. Eargle, Loudspeaker Handbook, (Kluwer Academic Publishers, 2003).